Universitetet i Stavanger

FACULTY OF SCIENCE AND TECHNOLOGY

MASTER'S THESIS

Study programme: MSc in Marine and Offshore Technology	Spring semester, 2020 Open
Author: Adham Amer	.... (author signature)
Programme coordinator: Prof. Muk Chen Ong Supervisor(s): Associate Prof. Lin Li/ Dr. Xinying Zhu	
Master thesis title: Numerical study on the deployment of a subsea template	
Credits: 30 ECTS	
Keywords: Offshore lifting operations; subsea template; over-boarding; lowering through splash-zone; time-domain simulations; allowable sea state assessment;	Number of pages: 102 + supplemental 11 material/other: Stavanger, June 29/ 2020 date/year

Numerical study on the deployment of a subsea template

by

Adham Amer

MASTER'S THESIS

Spring 2020

Department of Mechanical and Structural Engineering and

Materials Science

University of Stavanger

Supervisor: Associate Prof. Lin Li   Co-supervisor: Dr. Xinying Zhu

Abstract

Subsea templates are normally transported to the installation site on the deck of a crane vessel. After being lifted off from the deck, the template is 1) over-boarded from the initial location to the target position by the side of the vessel; 2) lowered through the splash zone; 3) further lowered down to the seabed and 4) finally positioned and landed.

All the mentioned phases should be evaluated. The over-boarding phase has not been the focus of analysis due to a large involvement of human actions and little involvement of hydrodynamic effects. During offshore operations, the offshore manager may decide to decrease the defined installation weather criterion if the risk of the personnel safety on deck during the over-boarding phase is considered high. Thus, it is of a great need to quantify the operational criterion for such operation.

The splash zone crossing phase is also a critical phase of the installation process and must be analyzed to define the installation weather criterion. Furthermore, the shielding effect provided by the installation vessel must be accounted for in order to achieve an accurate assessment of the allowable sea state.

The objective of this study is to perform numerical analyses and define the allowable sea states for a safe over-boarding and splash-zone crossing operations when deploying subsea templates. A coupled numerical model of the vessel and the subsea template is constructed in SIMA-SIMO for each phase. The numerical analyses using time-domain simulations have been performed in various sea states.

For the over-boarding phase, tugger lines have been modeled to control the motions of the template during the operation. The pendulum motions of the subsea template are considered as the critical responses for the assessment of the allowable sea states for the over-boarding phase.

The allowable sea states limiting criteria for the splash-zone crossing include slack sling, snap loads in wires. The assessment is done with and without the shielding effect provided by the vessel. Different sensitivity studies including the influence of the wave direction, seed number, and sizing of the suction anchor are also addressed during the splash-zone crossing.

Acknowledgement

This master's thesis study was performed under the supervision of Associate Prof. Lin Li and Dr. Xinying Zhu. This project fulfillment and the achieved results were thanks to the exceptional support provided by my supervisors.

Associate Prof. Lin Li was always supportive on both professional and personal level. She provided her guidance with great enthusiasm on every detail of this thesis. I felt more confident and achieved a better level of self-research and alternatives exploration while I was working under her supervision, and for that, I am deeply thankful.

Dr. Xinying Zhu expertise was an essential part of this project. I want to thank her for all the technical data and the time she provided for my thesis. She always gave her technical opinion on the study with constructive comments. The validation of the introduced numerical model in this study was thanks to the technical data she provided.

Finally, and most important, I would like to thank my parents, brothers, and fiancé for the continuous support they provided me throughout the different stages of my life until this point.

Adham Amer

June 2020

Stavanger, Norway

Acronyms and Abbreviations

API	American Petroleum Institute
CDF	Cumulative Density Function
CoB	Center of Buoyancy
CoG	Center of Gravity
DAF	Dynamic Amplification Factor
DDC	Depth-Dependent Coefficients
DHL	Dynamic Hook Load
DoF	Degree of Freedom
EVD	Extreme Value Distribution
EVT	Extreme Value Theory
FFT	Fast Fourier Transformation
GEV	Generalized Extreme Value
HLV	Heavy Lift Vessel
ITS	Integrated Template Structure
PDF	Probability Density Function
RAO	Response Amplitude Operator
SHL	Static Hook Load
SLI	Safe Load Indicator
SPS	Subsea Production System
SS	Steady State
TDM	Time-Dependent Mass
TLA	Tugger Lines Arrangement

Table of Contents

Table of Figures

List of Tables

Chapter 1

Introduction

1.1   Motivation and background

The development of offshore fields depends on the safe and efficient installation process of various subsea assets. However, the installation process involves high risks and hazards due to the uncertain and harsh nature of the marine environment [1]. The combined high costs of the operation and assets reduce any chances for correcting errors during the installation process. Furthermore, subsea assets are usually deployed for a long lifetime and the retrieving process is extremely complicated compared to onshore operations [2]. Engineering analytical work is required to tackle both the uncertainties and risks involved in the installation phase [3]. Although such analytical work can be time-consuming, it is still an effective and low-cost tool compared to the overall budget of the operation. The analytical work is applied within the planning phase of the operation. It can include but not limited to, collecting installation vessel and crane data, collecting weather forecasting data, and statistical modeling for the allowable sea states [4]. Numerical models can also be implemented in the analysis of various phases of offshore lifting operations [3, 5, 6]. Lifting operations are often classified as weather restricted operations. The operational limits need to be assessed during the planning phase [3]. For operations dominated by waves, operational limits are normally expressed in terms of sea state parameters, such as significant wave height (Hs) and spectral peak period (Tp). To quantitatively assess the allowable sea states, detailed numerical analysis is required to evaluate the critical responses and compare them with the allowable limits [3].

This thesis work covers a numerical study on the deployment of a subsea template. The current study consists of the development of two numerical models that allows an assessment of allowable sea states for two different phases of the lifting operation. Each lifting phase has its own operability study and limiting criteria based on the critical responses obtained from each numerical model [6, 7]. Furthermore, the operability analysis was conducted based on the recommended practices provided by DNV-GL.

1.2   Subsea production system (SPS)

The development of subsea fields is moving further offshore and deeper into the sea. Figure 1-1 compares the quantity of both shallow and deep-water subsea completions activities in the Gulf of Mexico from the year 1955 to 2005 [2].
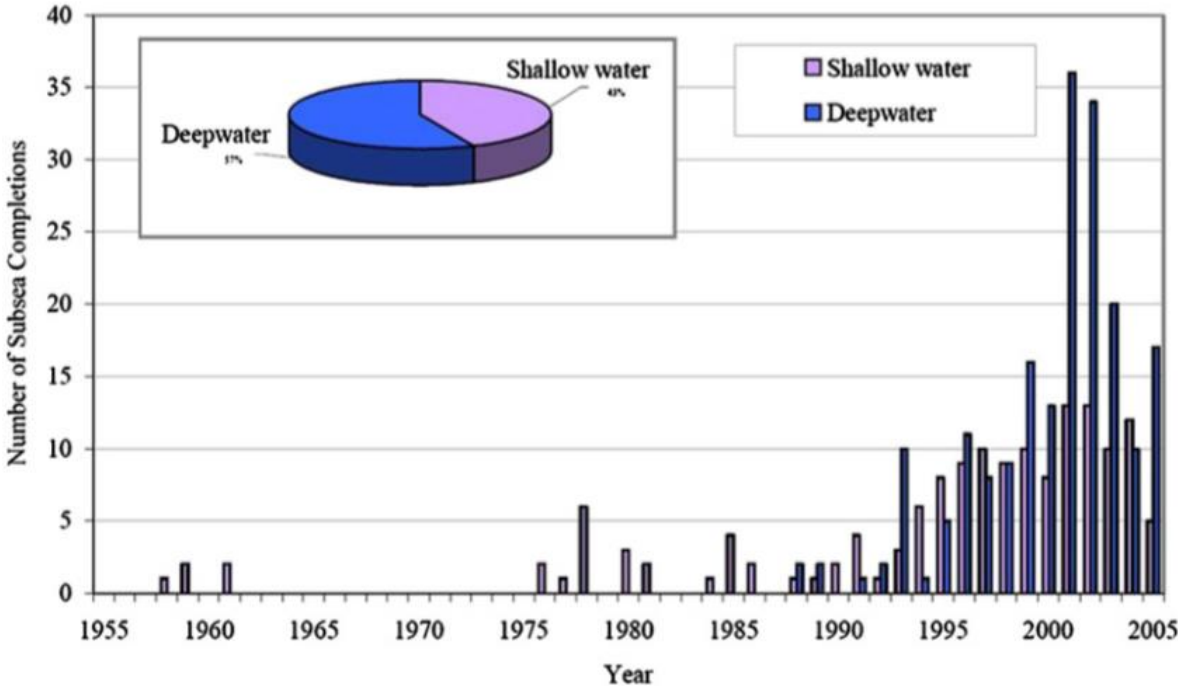
Figure 1-1 Number of shallow and deep-water subsea completions each year from 1955 to 2005 [2].

Subsea activities that takes place in a water depth of 305m or less are considered shallow-water completions, while any completion activity that is deeper than 305m are considered deep-water completion activity. Figure 1-1 clearly shows how the completions are advancing more towards deep-water in this 40 years period [2].

Figure 1-2 also illustrates the maximum water depth of subsea completion for each year of the same period in the Gulf of Mexico. It is noticed that the maximum water depth is increasing especially at the start of late 90s [2].
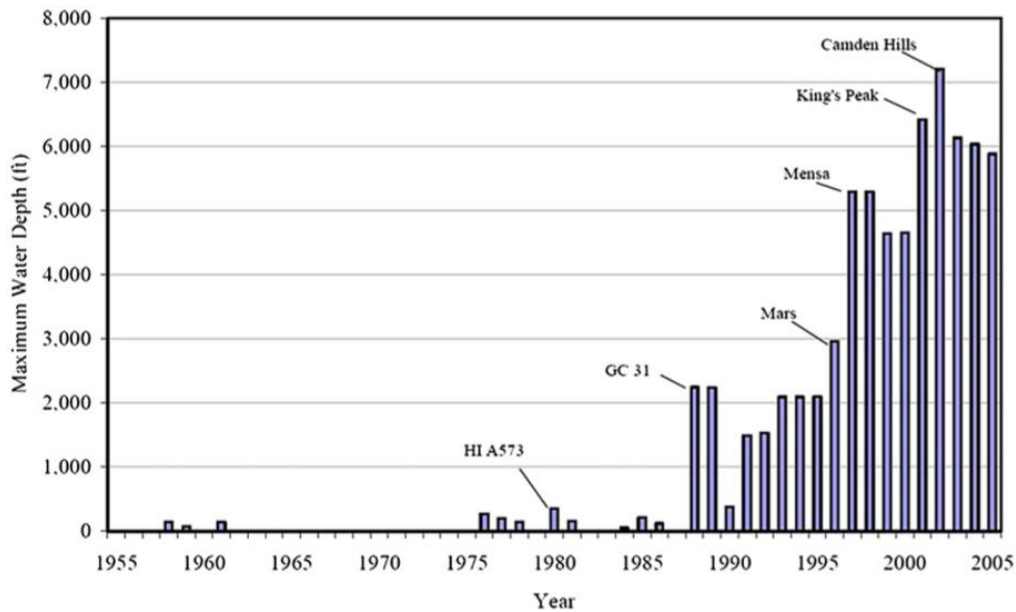
Figure 1-2 Maximum water depth of subsea completions installed each year from 1955 to 2005 [2].

This development requires a wide range of variety in SPS. According to NORSOK standards, the SPS is divided into the typical subsystems shown in Figure 1-3 [8].
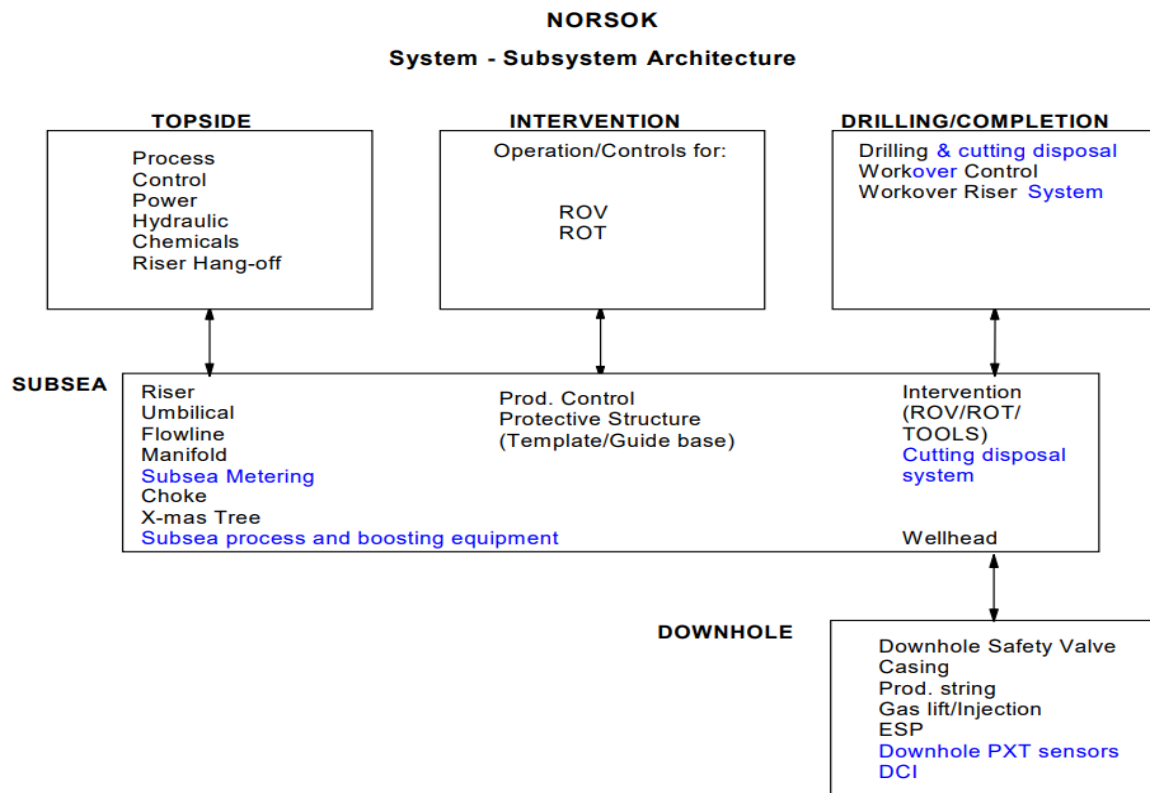
Figure 1-3 Subsea System Architecture [8].

The subsea architecture is represented by the middle block in the figure. This architecture main subsystems are [8]:

1) Wellhead and X-mas tree: Provide pressure-controlled access to the subsea well.
2) Umbilical system: To transmit electrical and hydraulic power signals as well as chemical injections from topside to the SPS.
3) Subsea structures and piping systems: Includes subsea templates, manifolds, and other protective structures.
4) Subsea flowlines: Acts as a medium to transfer oil and gas out of formulation zone as well as transferring injection fluids.
5) Subsea Processing: It includes Separation, metering, and boosting units for the SPS.

Subsea template

Subsea templates are seabed structures that provide guidance and support for well drilling equipment and other completion activity taking place on the seabed. The template also acts as a structural framework that supports other SPS components such as manifolds, risers, and wellheads [2].

The structural framework must be designed to withstand a variety of loads acting on the subsea template during drilling, completion, and production activities. Such loads are [2]:

1) External pressure loads
2) Environmental loads
3) Thermal expansion loads
4) Snag loads on pipelines

Integrated template structure (ITS)

ITS is used to support an integrated manifold system for produced fluids. They are also designed to allow close positioning of a group of well conductors. This application is typically used to group several wells at the same seabed location. The grouping of wells is also known as clustering wells [2].

Figure 1-4 Subsea template on seabed at Åsgard field [Source: Equinor].

The number of wells clustered within ITS is limited by the ITS size. Drilling rigs are usually used to deploy small-sized subsea templates, while Larger templates may require specialized installation vessels [2].

ITS main components are [2]:

1) Steel framework: Provide structural support
2) Top hatches: Provide protection against impacts from falling objects and fishing activities.
3) Washout sleeves: Provide protection against seabed soil layer collapse for large drilling activities.
4) Suction anchor: Provide a mean of soil penetration when the template is being deployed on the seabed.

Suction anchor

Generally, subsea templates have four equal-sized suction anchors. These anchors represent a large portion of the template distributed mass and volume. As previously mentioned, they provide a mean of soil penetration for the template and holding it down in the designated location on the seabed [2, 9].

Figure 1-5 Subsea template lowering at Åsgard field [Source: Equinor].

Suction anchors can be described as big metal cups. They are designed to resist both vertical uplift and horizontal loads. For vertical uplift loads, the following design factors are considered [2, 9]:

1) External skin friction
2) Reverse end bearing at the tip of the anchor pile
3) Submerged weight of the anchor
4) Soil plug weight

While for horizontal loads, the following factors are considered [2, 9] :

1) Passive and active resistance of the soil
2) External skin friction on the anchor wall sides
3) Anchor tip shear

The change in the anchor size and geometry will have a significant impact on these load factors. The geotechnical load capacity of the suction anchor is also considered, and it is mainly based on the seabed soil strength properties [9].

The anchor required bearing capacity for a given depth is estimated today based on the recommended practices provided by DNV-GL and American Petroleum Institute (API) [9].

1.3   General description of marine lifting operation

SPS deployment process requires specialized lifting vessels. The vessels are equipped with the necessary utilities for the intended water depth of the installation. The installation process involves high risks and usually, heavy lifting activity is kept at a minimum [2].

The following vessels are typically used within the scope of installing SPS [2, 4] :

1) Transportation barges and tugboats
2) Drilling vessels including jack-up rigs, semi-submersibles, and drill ships
3) Pipe-laying and umbilical-laying vessels
4) Heavy lift vessels (HLV)
5) Offshore support vessels

The vessel used in the scope of this study is a normal construction vessel for non-heavy lift applications. A vessel must be able to operate within a lifting capacity of 500 to 1000 tons to be categorized as HLV, while the vessel used in the study has a maximum lifting capacity of 400 tons.

Subsea installation tasks may involve [2]:

1) Installation of subsea structures and equipment
2) Laying of umbilical and pipelines
3) Subsea tie-ins operations

The typical deployment phases of offshore lifting operation are described by both DNVGL-RP-N201 and DNVGL-RP-N103. These phases are [10, 11] :

1) Pre-lift: In this stage, the vessel is within the designated location to carry out the operation. This is the last stage before the lifting starts.
2) Lift-off: The subsea asset is lifted from the vessel deck.
3) Over-boarding: The subsea asset is translated horizontally from the lift-off location to the lowering point over the sea.
4) Splash-zone crossing: The subsea asset is lowered through the free water surface where the wave kinematics is at its highest.

5) Lowering: The subsea asset is lowered further below the free water surface and closer to the deployment point on the seabed.

6) Vessel positioning: The vessel position is re-adjusted as the asset is getting closer to the deployment point.

7) Landing: The subsea asset is landed on the seabed designated location.

Each of these phases has operational criteria and challenges that must be tackled to ensure that the whole deployment process is carried out safely with minimal risks. This study focuses on two phases of the lifting operation, the over-boarding and the splash-zone crossing.

1.3.1 Over-boarding challenges

Despite the over-boarding phase does not involve complicated hydrodynamic loading on the structure, it is also a critical operation phase for which a safe deck handling needs to be ensured. In particular, the pendulum motions of the template in the air need to be well controlled.

Tugger lines connected with controlled winches are normally used for this purpose. The vessel roll and pitch motions, in this case, affect the performance of the lifting system, significantly. Both tugger lines arrangement and the crew working onboard help in limiting the motions of the lifted object during the operation. Winch drivers control the winches to ensure a safe and smooth engaging and disengaging tension forces on the tugger lines as the template reaches the lowering position.

The sudden activation and release of the tugger lines may cause transient motions of the lifted objects. The excessive horizontal motions of the template are hazardous to the working individuals and may also damage the assets onboard. Therefore, numerical studies on over-boarding operations are necessary for the planning phase to reduce the associated risks.

Due to the involvement of tugger lines, the over-boarding phase is dominated by non-linear responses. To simulate such an operation, two simulation approaches are normally used [12, 13] :

1) A steady-state approach which is based on finding the most critical position for the template during the over-boarding phase and running the simulations at this position under various wave conditions

2) A transient approach which is based on repetitive simulation of the whole transient over-boarding phase with different irregular wave realizations.

Both approaches are used in this study to assess the allowable sea states for the over-boarding process.

1.3.2 Splash-zone crossing challenges

Lowering subsea assets through the splash-zone is one of the most critical phases of offshore lifting operations [6]. The dynamic responses of the installation system must be identified within the planning phase of the operation by introducing an accurate numerical model [6].

The prediction of the induced motions and the slamming loads on the lowered object is quite challenging due to the transient effects that take place as the object reaches the air-wave interface [6]. Performing time-domain simulations of the installation system are recommended to evaluate similar operations according to DNVGL-ST-N001 [1]. To achieve a realistic numerical model for splash-zone crossing, the hydrodynamic loads acting on the lowered object must be estimated accurately.

According to DNVGL-RP-N201, the following concerns must be addressed during splash-zone crossing [10]:

1) Potential for damage to the lowered object due to the slamming loads.
2) Potential for snapping forces acting on the lift wire and slings due to slack limit being reached. DNVGL-OS-H206 defines the snap force as a short duration dynamic force which is associated with any sudden changes within the lifted object velocity [14].
3) The shift of the lifted object. This happens when the center of buoyancy (CoB) is no longer vertically in-line with the center of gravity (CoG) for the submerged object.

1.4 Literature review

1.4.1 Over-boarding

Few similar numerical studies were carried out for this phase of the operation with the intension of avoiding the induced pendulum motion when the objected is being translated in air. One of these studies was performed by Araujo et al [15]. The aim of the study was to propose a methodology for over-boarding operations with a focus on avoiding the induced pendulum motions of the lifted object by defining a minimum relative angle between the crane wire and the vessel vertical axis [15].

However, this thesis will focus on providing a numerical modeling methodology for the operation while controlling the pendulum responses with the introduced tugger lines. Furthermore, the study will try to address the critical pendulum responses for the over-boarding phase with respect to the operational sea states. Finally, the study will compare different time-domain simulation approaches based on the operation allowable sea state.

Examples of assessment of operational limits for various lifting operations have been studied in the literature, such as lifting operations of foundations, spool pieces, and suction anchors [6, 16, 17] . Moreover, various sources of uncertainties, such as weather forecasts and wave spectral shape have also been evaluated in other studies to provide safety margins to the operational limits [18, 19] .

However, these studies were focused on the splash-zone crossing and deep-water installation, while the over-boarding phase does not share the same level of focus in literature when numerical modeling and operational limits are being addressed.

1.4.2   Splash-zone crossing

Several numerical studies were performed addressing the splash-zone crossing dynamic responses. Bunnik and Buchner introduced an improved numerical method to simulate non-linear waves load on the structure during the splash-zone crossing. The method also took into account the flow in and out of the structure [20]. Jia and Agrawal introduced a wave loads prediction approach by using fluid-structure interaction. The approach was implanted for the lowering of a subsea manifold in splash-zone using CFD numerical modeling [21].

Yufang et al. performed numerical study on the installation of a subsea tree through the splash-zone. The study addressed the influence of multiple marine environments, and the multi-body movement relationship between the installation vessel and the lowered object. The focus was on providing a recommended installation winch speed, flow velocity, and wave height to carry out the operation safely [22].

Furthermore, some of these studies developed new numerical methods to account for the shielding effect generated by the floating installation vessel the during splash-zone crossing. A study by Li et al. included an operability analysis approach for monopile lowering operation which accounted for the shielding effect provided by the installation vessel [12]. Another numerical study by Li et al. utilized the shielding effect for large spool piece splash-zone crossing [6].

However, fewer studies are available in literature when it comes to assessing the operational limits of splash-zone crossing for large subsea structures such as templates while accounting for the shielding effect provided by the installation vessel.

The thesis will propose a numerical modeling methodology to account for the dynamic responses associated with splash-zone crossing for a subsea template with and without shielding effect. An assessment of the operational limits will also be addressed in association with the obtained dynamic responses from the time-domain simulations.

1.5   Aim and scope

As discussed in section 1.3.1 and 1.3.2, the challenges of each phase require an accurate utilization of numerical modeling in order to evaluate the operational limits and the allowable sea states. The following points must be tackled within the scope of this thesis to overcome the challenges in each phase:

Over-boarding phase

1) Build an accurate numerical model of the over-boarding phase, which requires:
    a) Modeling of the subsea template
    b) Modeling of the vessel ballast system
    c) Modeling of the crane articulated structure
    d) Modeling of the system tugger lines to control the induced pendulum motion
2) Set-up the limiting criteria for the operation based on the challenges in section 1.3.1

3) Comparing different approaches of time-domain simulations for the developed numerical model

4) Perform allowable sea state assessment and operability analysis based on statistics of the critical dynamic responses

Splash-zone crossing phase

1) Build an accurate numerical model of the splash-zone crossing phase, which requires:
   a) Modify the subsea template model to include the hydrodynamic forces and perforation effect
   b) Modify the vessel model to include the wave diffraction data for the shielding effect
2) Set-up the limiting criteria for the operation based on the challenges in section 1.3.2
3) Comparing time-domain simulations dynamic responses with and without the shielding effect
4) Perform allowable sea state assessment and operability analysis based on statistics of the critical dynamic responses

Figure 1-6 illustrates the general scope of the thesis based on the previously outlined points in the above section.
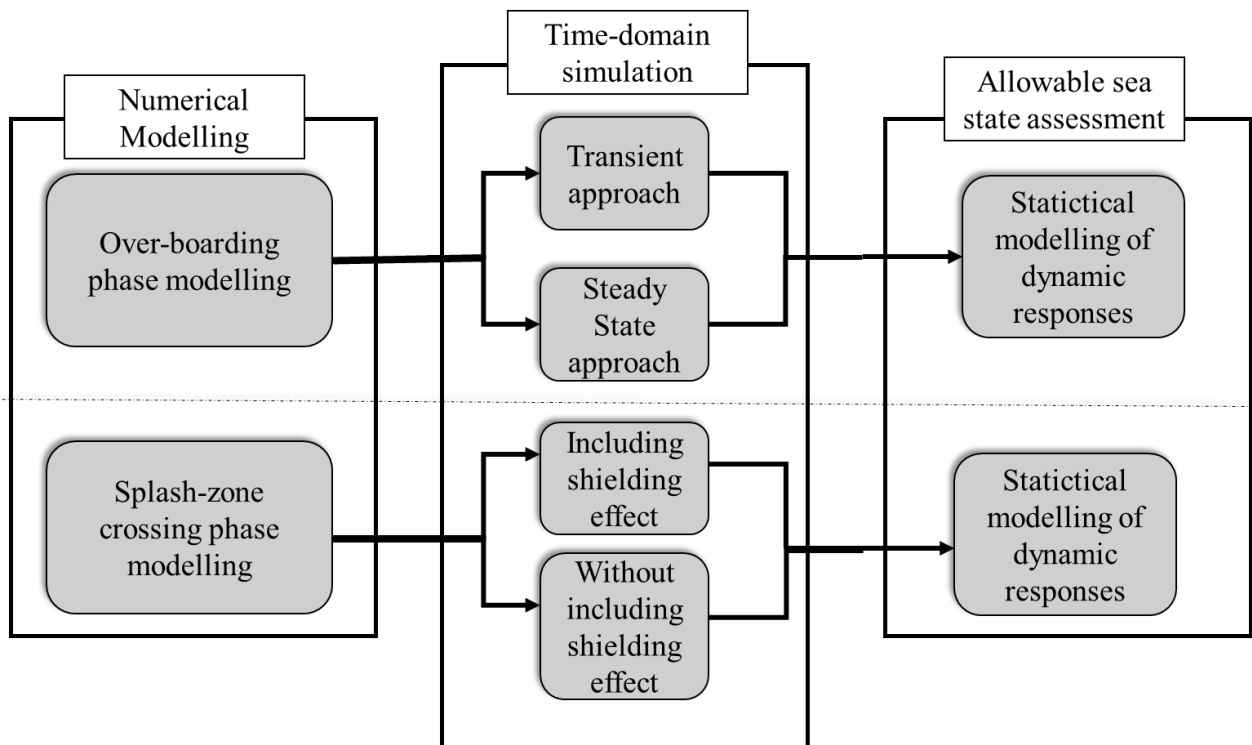
Figure 1-6 Thesis general scope.

Thesis structure

The thesis includes seven chapters in total. The following is a brief description of the content of each chapter.

Chapter 1

This chapter discusses the motivation behind this study and provides a brief description of the SPS. The chapter also discusses the general phases of offshore lifting operation with emphasis on the challenges of the two phases of interest in the study. The aim and scope of the study is also addressed at the end of this chapter.

Chapter 2

This chapter illustrates the theoretical basis behind the numerical modeling of each phase of interest. The chapter includes a description of waves, airy wave theory, and wave load. The last section includes a discussion on the probability and statistical models used in this study.

Chapter 3

This chapter addresses the components of the lifting system. The numerical models used in the time-domain simulations for over-boarding and splash-zone crossing are also described in this chapter. The hydrodynamic forces calculations for the subsea template are also presented.

Chapter 4

This chapter discusses the operational limiting criteria for both over-boarding and splash-zone crossing. A brief comparison between the dynamic responses of both the transient and steady state approach is presented for the over-boarding phase. A similar assessment for the dynamic responses during splash-zone crossing is also discussed in this chapter.

Chapter 5

This chapter includes the allowable sea state assessment for the over-boarding phase based on the statistical modeling of the extreme responses. The allowable sea states are compared for both transient and steady state approach with different tugger lines arrangement.

Chapter 6

This chapter includes the allowable sea state assessment for the splash-zone crossing phase based on the statistics of the extreme responses. The allowable sea states with and without the shielding effect are compared. The chapter also includes a sensitivity study on changing the wave direction while utilizing the shielding effect. Another sensitivity study addressing the influence of the suction anchor size on the splash-zone dynamic responses is also included. Finally, the chapter provides a validation by comparing the dynamic hook load of the numerical model and the actual crane measurement of the installation vessel.

Chapter 7

This chapter concludes the thesis work and provide a brief future recommendation on the study.

Chapter 2

Theoretical Basis

2.1 General

This chapter will discuss the theoretical background behind the numerical models. It includes sub-sections for:

1) Description of waves and airy wave theory.
2) The wave loads acting on slender structures during the splash-zone crossing.
3) Description of the vessel and crane tip motion.
4) Statistics for extreme values.

2.2 Description of waves

By nature, ocean waves have irregular and random characteristics. In terms of modelling the only way to describe real sea state is by implementing a random wave model. Those random waves can be both linear and non-linear [23]. Waves can be generated by different sources, such as [23]:

1) Wind
2) Earthquakes
3) Tides

Waves generated by blowing wind are most common and they are the main concern in marine operations design as well as in the scope of this study.

In a region of storm generation, high-frequency sea waves start dissipating and transforming to low-frequency waves. Due to differences in frequency, waves start travelling at different speeds. Thus, outside the region of storm generation, the sea state is modified as the various frequency components start separating as shown in Figure 2-1 [24].
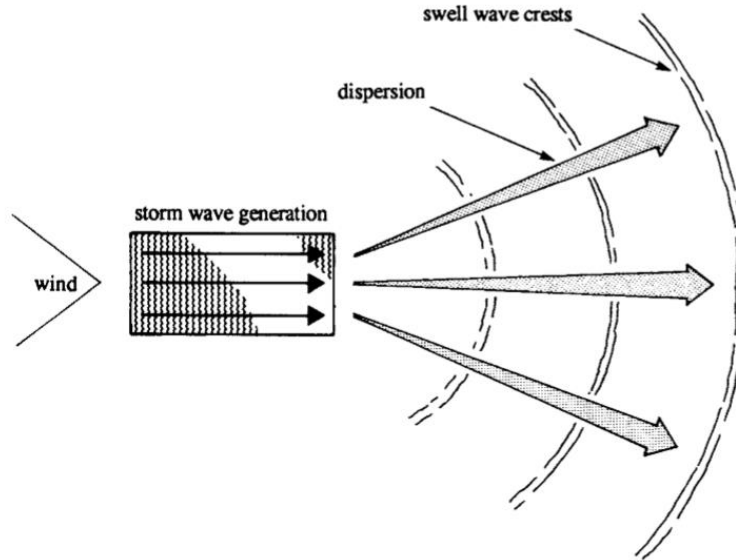
Figure 2-1 Wave generation and dispersion [24].

Low-frequency waves are faster than high-frequency ones. This results in a swell sea condition which is the opposite of the storm sea condition. Swell waves are long-crested and not very steep. They can also travel to longer distances without any apparent decay. Wind waves are short crested, steep, and have a larger direction and frequency range compared to swell waves. [24].

2.2.1   Regular and irregular waves

Regular waves propagate in a permanent form, hence comes the name regular. They have a defined length, period, and height. The wave surface has a sinusoidal shape and can be expressed with position x and time t by the following function [23, 24]:

$$\eta(t) = A_k \cos(k_n x - \omega_k t) \qquad (2.1)$$

where A_k is the amplitude of the Kth component of the wave, ω_k is the angular frequency of the Kth component of the wave, t is the associated time in seconds and k is the wave number.

However, to represent a real sea state, irregular wave theory is implemented by summing sinusoidal regular wave components in a superposed manner as the following shows [23, 24],

$$\eta(t) = \sum_{k=1}^{N} A_k \cos(k_n x - \omega_k t + \varepsilon_k) \qquad (2.2)$$

ε_k is the random phase angle of the Kth component of the wave. By generating random ε_k varying from 0 to 2π for each sinusoidal component and summing these components together, one wave realization can be achieved [23, 24]. A common method used to generate independent random values for ε_k is Monte Carlo simulation [25].
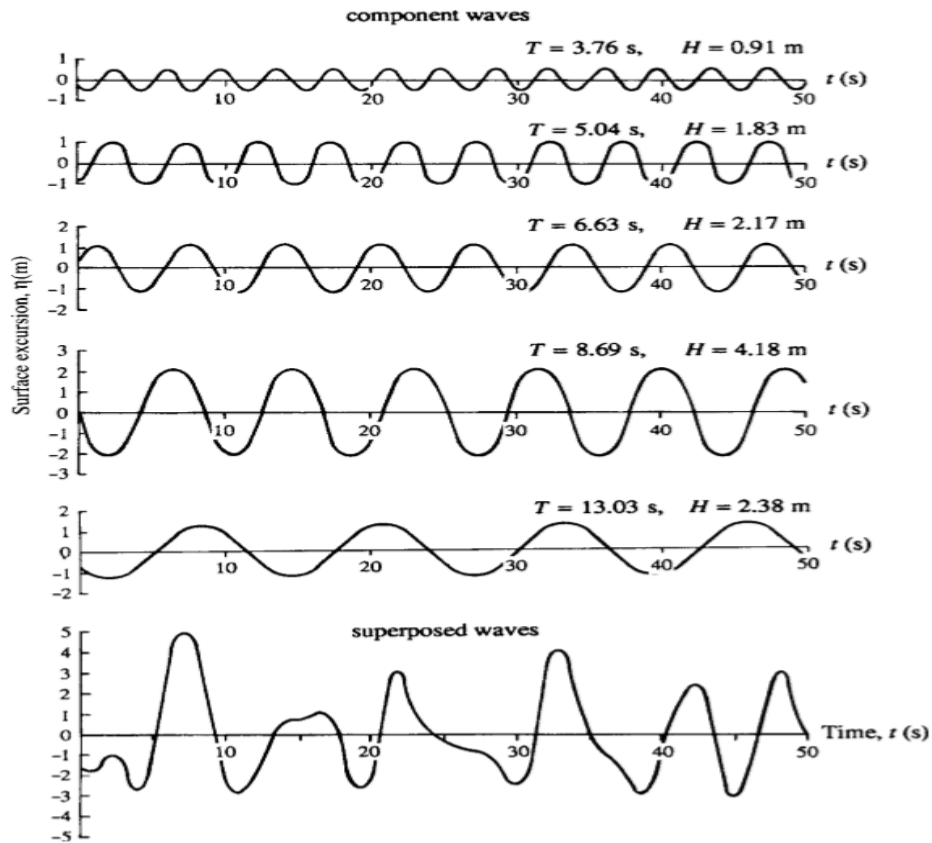
Figure 2-2 Superposed waves generation by summing component waves [24].

2.2.2   Linear and non-linear waves

A linear wave model is achieved by combining several small linear wave components which are out of phase with respect to each other, these components have different values for amplitude, frequency, and direction. The non-linear wave model follows the same principle, but the difference in the frequency of each wave component is caused by the non-linear interaction between each of the wave components [23, 24].

Airy wave theory

The airy wave theory follows a potential flow approach, this approach assumes that the flow is irrotational as well as inviscid. These assumptions are only valid in cases where some flow characteristics such as turbulence and flow separation can be neglected. According to the airy wave theory framework, the fluid particles are constantly in orbital motion as the free surface of the seawater shows wave propagation. These orbits are circular in shape at deep water and ellipses when the water depth is relatively shallow. The diameter of these orbits reduces at the water layers below the free surface(see Figure 2-3) [24, 26].

direction of wave propagation

deep water circular orbits   transitional water elliptical orbits
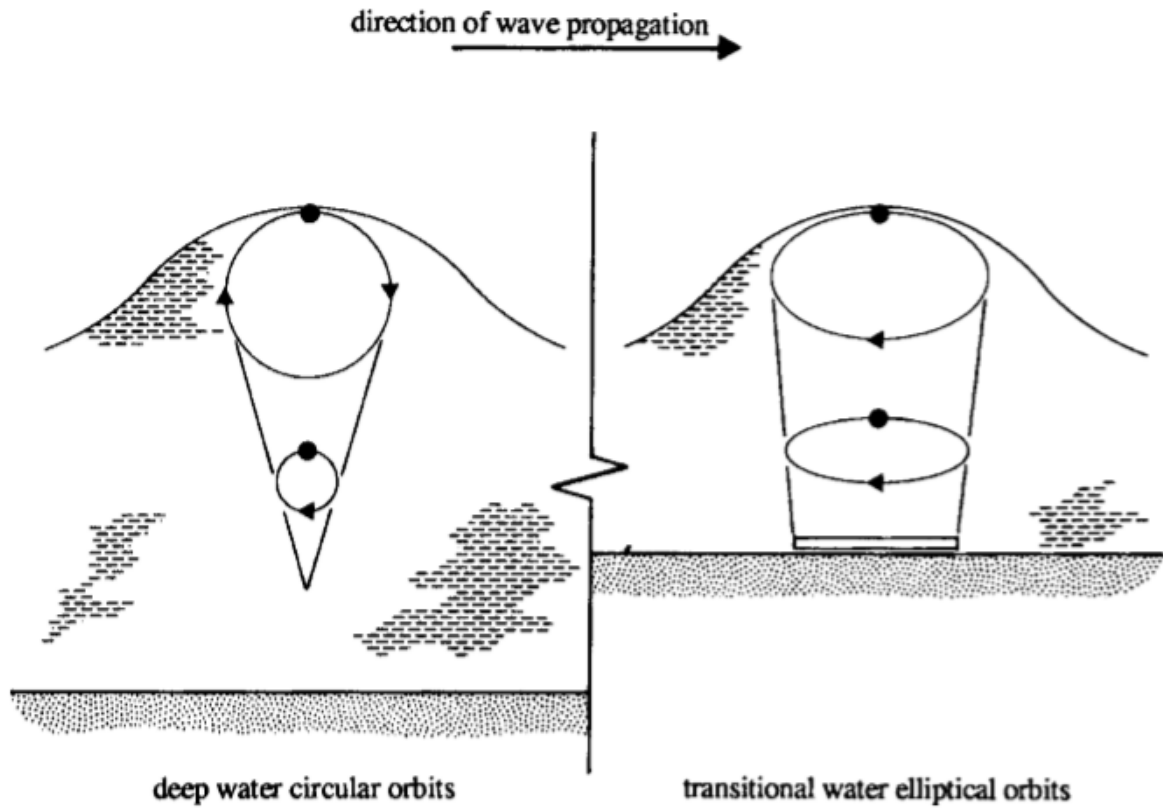
Figure 2-3 Fluid particles motion according to airy wave theory framework [24].

The following equation expresses the non-rotational property of the flow [26]:

$$\nabla \times \vec{U} = 0 \tag{2.3}$$

where $\vec{U}$ is the velocity of particles and ∇ is the differential operator. The first order Laplace differential equation partial derivatives are equal to the velocities in these directions with respect to the directions, so that,

$$\nabla \phi = \frac{\delta \phi}{\delta x}\vec{\imath} + \frac{\delta \phi}{\delta y}\vec{\jmath} + \frac{\delta \phi}{\delta z}\vec{k} = \vec{U} \tag{2.4}$$

The second-order Laplace equation is then obtained from the fluid incompressibility assumption so that,

$$\nabla^2 \phi = 0 \tag{2.5}$$

These derivative equations are utilized to obtain the velocity and acceleration of the particles, which will be used to calculate the induced wave loads on slender structures [26].

Boundary conditions

The Laplace differential equation Eq.(**2.4**) requires a set of boundary conditions to be solved. These boundary conditions are shown in Figure 2-4 [26].
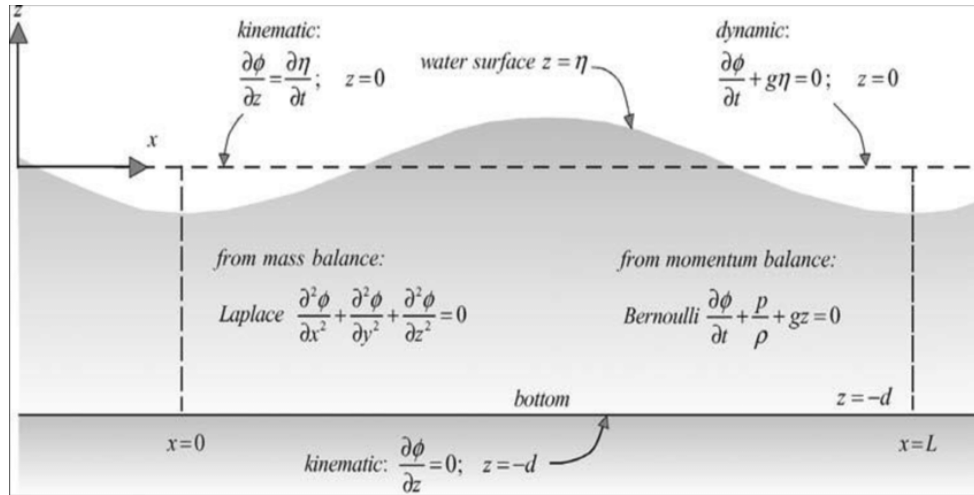
Figure 2-4 Basic equations and boundary conditions for the linear wave theory, in terms of the velocity potential (Holthuijsen, 2007). [Uploaded to Research Gate by Saber M. Elsayed].

The bottom boundary condition

The water is not allowed to flow through the seabed. The flat seabed is located at a water depth of $z = -d$. This boundary condition can be expressed as [26],

$$\frac{\partial \phi}{\partial z} = 0 \quad at\ z = -d \tag{2.6}$$

The wall boundary condition

The water is not allowed to flow through a wall located at a horizontal distance $x = a$. In case the wall moves with a velocity $V(t)$ at time t, the boundary condition is expressed as [26],

$$\frac{\partial \phi}{\partial x} = V(t) \quad at\ x = a(t) \tag{2.7}$$

The surface boundary conditions

A no-leak condition is established by the kinematics of the free surface so that the water is not allowed to flow through the surface. The vertical velocity component of the fluid particle at the free surface is always equal to the velocity of the same free surface. This boundary condition can be expressed as [26],

$$\frac{\partial \phi}{\partial z}\big|_{z=\eta(x,t)} = \frac{\partial \phi}{\partial z}\big|_{z=0} = \frac{\partial \eta}{\partial t} \tag{2.8}$$

where η is the wave surface elevation.

The pressure at the free water surface is constant and equal to the atmospheric pressure. Based on this and by applying the general Bernoulli equation, the dynamic free surface boundary conditions can be expressed as [26],

$$\eta = -\frac{1}{g}\frac{\partial \phi}{\partial t} \quad at \ z = 0 \tag{2.9}$$

By combining the two surface boundary conditions from Eq. **(2.8)** and Eq. **(2.9)**, The following expression can be obtained,

$$\frac{\partial^2 \phi}{\partial t^2} + g\frac{\partial \phi}{\partial z} = 0 \quad at \ z = 0 \tag{2.10}$$

2.2.3   Wave spectrum

It is necessary to have an estimation for the sea state conditions when modeling marine operations. These conditions are usually described in a statistical manner in the form of a wave spectrum. [24].

Wave spectrum is used to describe the short term stationary irregular sea states, it is the power spectral density function of the vertical sea surface displacement. Two main parameters are used in characterizing a stationary sea state, significant wave height *Hs* and peak period *Tp*. Thus, the wave spectrum is often defined by these two parameters [23, 24].

When modeling in wind seas, three spectra are frequently used, The Pierson-Moskowitz spectrum, Brettschneider spectrum, and JONSWAP spectrum. These spectrums have the following features [24]:

1) Pierson–Moskowitz is for fully developed seas only
2) JONSWAP is developed under fetch-limited conditions
3) Brettschneider accounts for the duration and fetch limitation in an empirical manner.
4) All of them are single-peaked spectra

Currently, JONSWAP spectrum is commonly used in both laboratory experiments and for marine design. The scope of this study will also utilize JONSWAP spectrum [24].

JONSWAP Spectrum

JONSWAP spectrum was formulated as a modification of Pierson-Moskowitz spectrum [23]

$$S_J(\omega) = \frac{5}{16} A_\gamma H_S^2 \omega_P^4 \omega^{-5} \ exp\left(-\frac{5}{4}\left(\frac{\omega}{\omega_p}\right)^{-4}\right) \gamma^{\exp\left(-0.5\left(\frac{\omega - \omega_P}{\sigma \ \omega_P}\right)^2\right)} \tag{2.11}$$

$S_J(\omega)$ is JONSWAP spectrum density, A_γ is a normalizing factor, H_S is the significant wave height, ω_p is the angular peak frequency, γ is a non-dimensional peak shape parameter and σ is spectral width parameter [23].

The corresponding spectral moment M_n, of the wave spectra is [23]:

$$M_n = \int_0^\infty \omega^n \ S(\omega) \ d\omega_n \tag{2.12}$$
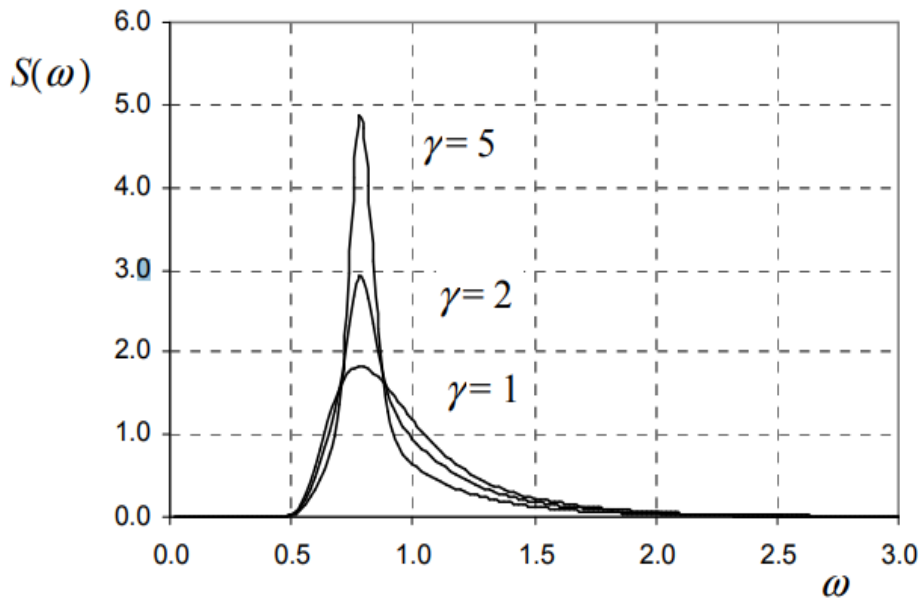
Figure 2-5 JONSWAP spectrum with different peak shape parameter [23].

2.2.4 Wave diffraction

Waves bend around obstructions such as vessels, platforms, or any other offshore structure. The process happens by radiation of wave energy. Figure 2-6 illustrates an incidence of wave train upon the tip of a breakwater [24].
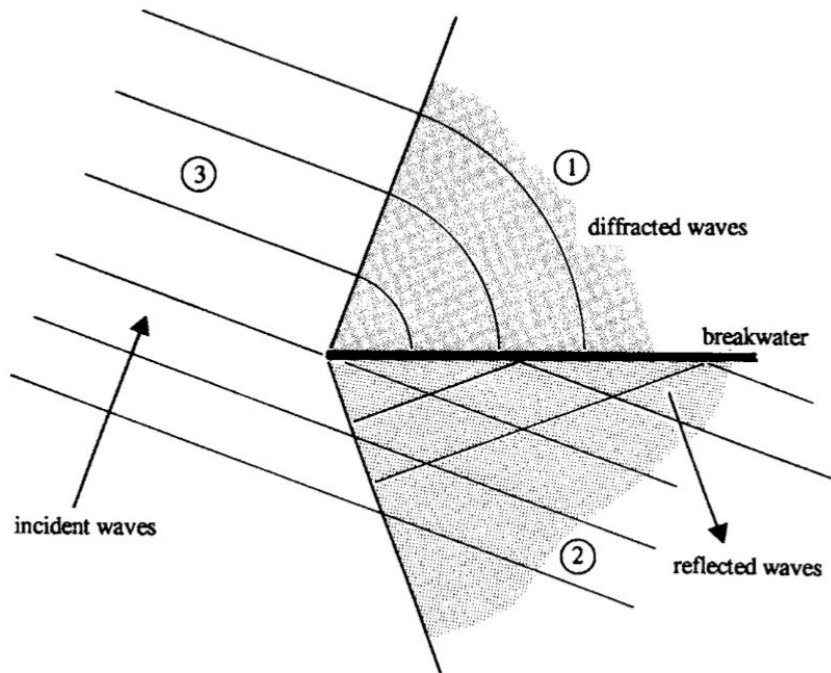
Figure 2-6 Diffraction around an impermeable breakwater [24].

The figure shows three regions [24],

1) Region 1: This is the region where the diffraction occurs. In this region, the waves generate circular arcs that are centered around the tip point of the breakwater. The incident wave height diminishes due to the diffraction and their energy spread over the region.
2) Region 2: This is a region with short-crested waves in which the reflected and the incident waves overlap. In a real-life scenario, the reflected waves from this region will travel to region 3 in a form of radiation. This will extend the generated short-crested waves due to diffraction from region 2 to region 3.
3) Region 3: In this region, the incident waves flow freely undisturbed by any obstructions

2.3 Wave loads during splash-zone crossing

2.3.1 Morison's equation

Morison's equation is used in estimating the acting hydrodynamic forces on a slender structure [11, 27]. The equation is formed from the summation of both drag and inertia forces acting on the slender element.

The inertia component is linear and in phase with the acceleration of the local flow, which is originated from the potential flow theory and oscillating flows. The drag component is quadratic and proportional to the square of the instantaneous flow velocity [11, 27].

The total inline force acting on the slender element $F(t)$ is given by [11, 27]:

$$F(t) = \rho(1 + C_a)V\dot{u} + \frac{1}{2}\rho C_d A u|u| \tag{2.13}$$

where the inertia force F_I is introduced by the term $\rho(1 + C_a)V\dot{u}$, while the drag force F_D is $\frac{1}{2}\rho C_d A u|u|$.

ρ is the fluid density

C_a is the added mass coefficient

V is the volume of the element

$\dot{u}$ is the flow acceleration

C_d is the drag coefficient

A is the cross-sectional area of the body perpendicular to the flow direction

u is the flow velocity

By summing the sectional forces of each element, the total resultant force on the slender structure can be obtained [11].

Morison equation is based on a uniform flow acceleration assumption at the submerged body location. This assumption requires that the diameter of the structural element be much smaller than the wavelength [11].

As a rule of thumb [11],

$$\lambda \geq 5D \tag{2.14}$$

where D is the outer diameter of the slender element and λ is the wavelength. The airy wave theory can be used to provide an estimated value for the wavelength at any given water depth [11],

$$\lambda = T\sqrt{\frac{g}{k}\tanh{(kd)}} \tag{2.15}$$

where T is the wave period, d is the water depth, k is the wave number and g is the gravitational acceleration.
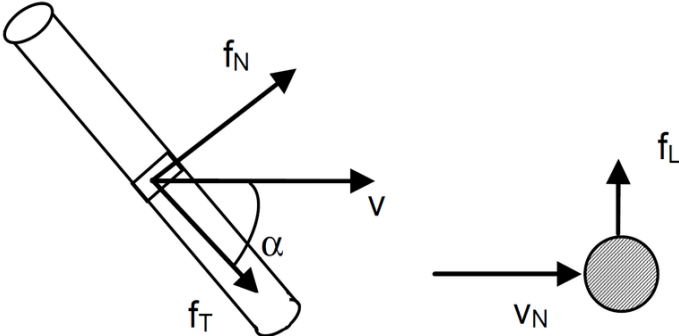
Figure 2-7 Hydrodynamic forces acting on slender element [11] .

Figure 2-7 illustrates the three acting components hydrodynamic forces on a slender element, and the normal velocity component $\overrightarrow{V_n}$ of the water particle. In the case of an inclined slender element, an angle α is formed between the element vertical symmetry axis and the velocity vector $\vec{V}$. The hydrodynamic forces f_N, f_T, and f_L stand for normal, tangential, and lift force respectively.

The normal component of the hydrodynamic forces is expressed in term of inertia and drag forces as previously shown in Eq. (2.13). The tangential force component is relatively small

compared to the normal component and the following expression is used to estimate the tangential force acting on the element:

$$f_T = \frac{1}{2}\rho C_t D u^2 \tag{2.16}$$

where C_t is the tangential drag coefficient and D is the outer diameter of the element.

2.3.2 Hydrodynamic coefficients

Hydrodynamic coefficients are non-dimensional empirical coefficients used in calculating both the inertia and the drag forces from Morison's equation. In general, the coefficients depend on three main factors. These factors are Keulegan–Carpenter number, Reynolds number, and surface roughness [11].

Added mass coefficient

For a cylindrical slender element, the added mass coefficient C_a can be obtained from [11],

$$C_a = \frac{m_a}{\rho A} \tag{2.17}$$

where m_a is the added mass per unit length and A is the element cross section area.

Drag coefficient

Generally, the normal drag coefficient C_{Dn} depends on both Reynolds number and the angle of incidence α. In cases where the flow regime is sub-critical and super-critical, C_{Dn} can be obtained independently from α. As for critical flows, C_{Dn} may show strong variations based on the flow direction and thus α must be taken into account [11].

The tangential drag coefficient C_{Dt} can also be obtained as a function of both C_{Dn} and α by using the following expression [11]:

$$C_{Dt} = C_{Dn}(m + n\,sin\alpha)cos\alpha \tag{2.18}$$

Both m and n depend on the element type as shown in Table 2-1

Table 2-1 Tangential drag coefficients dependency parameters [11].

Element Type	m	n
Bare cables, cylinder	0.02-0.03	0.04-0.05
Faired cables	0.25-0.5	0.5-0.25
6-stranded wire	0.03	0.06

Effect of Reynolds number, Keulegan–Carpenter number and roughness

A significant drop in the drag coefficient can be noticed in Figure 2-8 when Reynolds number value is within the critical flow regime range [11].

When Reynolds number is higher than 10^6 and Keulegan–Carpenter number is large enough, the steady drag coefficient C_{DS} can be obtained as a function of surface roughness Δ from [11],

$$C_{DS}(\Delta) = \begin{cases} 0.65 & ; \Delta < 10^{-4}\,(\text{smooth}) \\ (29 + 4 \cdot \log_{10}(\Delta))/20 & ; 10^{-4} < \Delta < 10^{-2} \\ 1.05 & ; \Delta > 10^{-2}\,(\text{rough}) \end{cases}$$

When the cylindrical element is subjected to a supercritical flow regime, the variation of the drag coefficient C_D can be expressed as a function of Keulegan-Carpenter number K_c from [11],

$$C_D = C_{DS}(\Delta). \psi(K_c) \tag{2.19}$$

where $\psi(K_c)$ is the wake amplification factor.
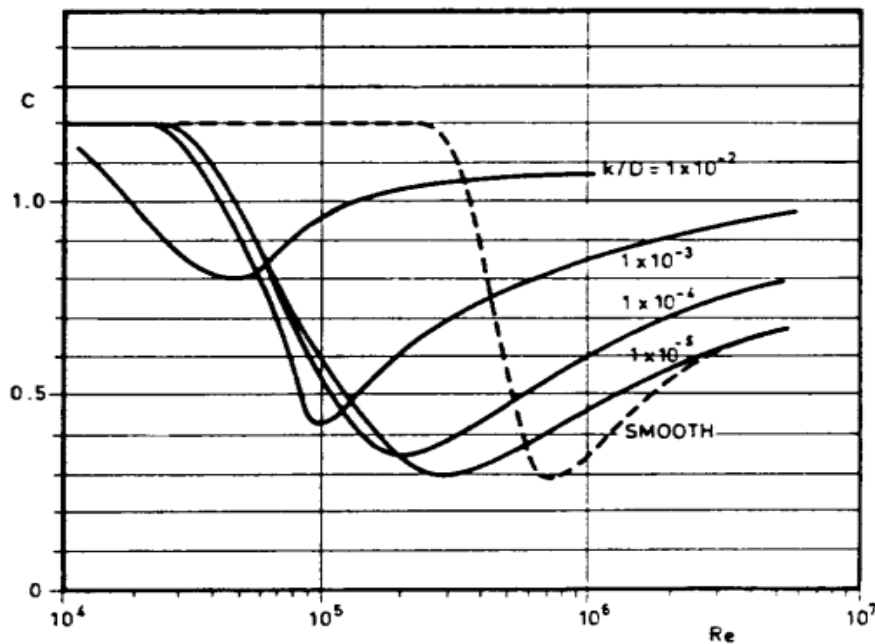
Figure 2-8. Drag coefficient for fixed circular cylinder for steady flow in critical flow regime, for various roughness [11].

2.3.3   Slamming loads

The slamming force $F_s(t)$ acting on an object lowered through the splash-zone is equivalent to the rate of change of fluid momentum. This force is caused by the impact between the lowered object and the water at the free surface. The following equation is used to estimate the slamming force as a function of the rate of change of the instantaneous high-frequency limit heave added mass $A_{33}^\infty(t)$ [11],

$$F_s(t) = v_s \frac{dA_{33}^\infty(t)}{dt} \tag{2.20}$$

where v_s is the constant slamming velocity.

The slamming force $F_s(t)$ can also be expressed in term of the slamming coefficient C_s as follows [11],

$$F_s(t) = \frac{1}{2}\rho C_s A v_s^2 \tag{2.21}$$

where A is the horizontal projected area of the lowered object

C_s is defined by [11],

$$C_s = \frac{2}{\rho A}\frac{dA_{33}^\infty}{dh} \tag{2.22}$$

where h is the submergence relative to surface elevation

2.4 Vessel motion

When a vessel is floating freely without constrains, it experiences six degrees of freedom (DoF) motions. Three of these motions are translational, i.e. surge, sway, heave and the other three are rotational, i.e. roll, pitch, and yaw. Figure 2-9 illustrates the axis of each motion [28]:
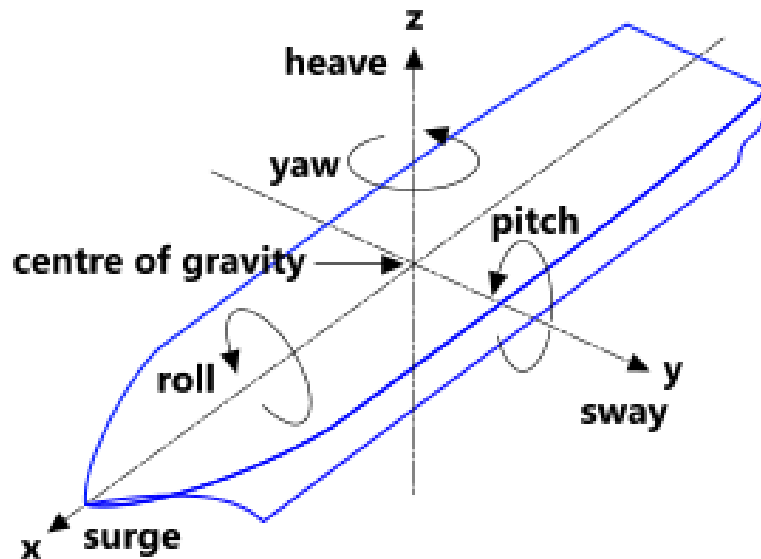
Figure 2-9 Floating vessel 6 DoFs.

The vessel motion depends on its transfer functions response amplitude operators (RAOs). They are defined mainly by the vessel metacentric height and its physical properties. Furthermore, they allow the transfer of the exciting waves into the response of the structure hence the name transfer function [28].

2.4.1 Response amplitude operator (RAO)

Response amplitude operators are a function of frequency and used for the transfer functions and their related phase angles. Each RAO applies to the associated movement of a vessel's CoG at a certain given sea state [28].

Generally, the transfer function is a ratio between the response and wave amplitude. It gives both the amplitude and phase shift of each response with relevance to the sea wave component. This is applicable to each DoF of the vessel and expressed by [28]:

$$H_k(\omega) = A_k(\omega)\, exp\, (k\varepsilon_k(\omega))$$

(2.23)

where $H_k(\omega)$ is the transfer function of the kth degree of freedom, $A_k(\omega)$ is the amplitude of the transfer function, $\varepsilon_k(\omega)$ is the phase angle and ω is the angular frequency [28].

RAO is the absolute value of $H_k(\omega)$ and is also a function of frequency [28].

$$RAO = |\,H_k(\omega)\,| = |\,A_k(\omega)\, exp\, \big(k\varepsilon_k(\omega)\big)\,|$$

(2.24)

2.4.2 Crane tip motion

The six DoFs from Figure 2-9 can be donated as x, y, z for surge, sway and heave, and ϕ_x, θ_y, ψ_z for roll, pitch and yaw. For a given point $P(x_p, y_p, z_p)$ on the local coordinate system of the vessel, such as the crane tip point, the motion of this point can be expressed as [11, 29]:

$$P = \big(x + z_p\theta_y - y_p x\big)i + \big(y - z_p\phi_x + x_p\psi_z\big)j + \big(z + y_p\phi_x - x_p\theta_y\big)k$$

(2.25)

where, i, j and k are the unit vectors along the local coordinate system in x, y and z respectively. This equation assumes that the vessel motions are small so that no major change occurs at the water plane area [11, 29].

The vertical motion of the vessel and the crane tip are the main concern for the over-boarding and lowering operation. The vertical motion of the crane tip has also ahigh influence on the excitation of the pendulum motion of the template [15].

The total vertical motion can be expressed as:

$$P_v = z + y_p\phi_x - x_p\theta_y$$

(2.26)

The previous equation clearly illustrates that besides the heave motion z, the crane tip vertical motion is highly influenced by its location on the local coordinate system with respect to the vessel CoG. For instance, the further the crane tip location is from the CoG in y-direction, the higher the contribution of the roll motion in the equation is [11, 29].

As previously mentioned in section 2.4.1, the transfer function is a ratio between the complex response amplitude and the wave amplitude so that,

$$H_k(\omega) = A_k(\omega) \, exp\left(k\varepsilon_k(\omega)\right) = \eta_a/\zeta_a$$

$$\eta_a = H_k(\omega)\zeta_a = A_k(\omega) \, exp\left(k\varepsilon_k(\omega)\right)\zeta_a \qquad \textbf{(2.27)}$$

where η_a is the amplitude of the given degree of freedom motion, and ζ_a is the amplitude of the wave.

By substituting Eq.**(2.27)** into Eq. **(2.26)**, the total vertical motion becomes:

$$P_v = \left[H_z(\omega) + y_p H_{\phi_x}(\omega) - x_p H_{\theta_y}(\omega)\right]\zeta_a \qquad \textbf{(2.28)}$$

2.5   Probability model

When evaluating a phenomenon with high randomness involved, a precise prediction of the results is impossible to achieve. A statistical probability model is required to express the various possible outcomes of the study and to make up for the lack of certainties regarding future conditions. A probabilistic model can be established in order to assess the limiting conditions for the operation [25].

In order to account for the variability of stochastic waves, different realizations of irregular waves are generated for each wave condition using different seeds. A statistical method is applied to estimate the extreme responses when assessing the allowable sea states [25]. For instance, the critical responses in this study include the pendulum motions of the template during over-boarding, the maximum and minimum loads on the main lift wire and slings during the splash-zone crossing.

Extreme value theory (EVT)

EVT deals with the stochastic behavior of rare extreme events. These extreme events can be significantly greater or smaller than any other recorded events in the sample population. Unlike the central limit theorem (CLT), EVT starts from the limit distribution of the sample maximum. The theory provides a semi-parametric model for the tails of the distribution function [30].

The three types of extreme value distribution (EVD) are [30],

1) Gumbel distribution
2) Fréchet distribution
3) Weibull distribution

Gumbel distribution

The Gumbel EVD, also known as EVD type 1, is widely used in predicting both maximum and minimum extreme responses for offshore structures [31, 32]. The cumulative density function (CDF) of Gumbel distribution is given by,

$$F_x(x) = exp\left[-\exp\left(\frac{x-\lambda}{\kappa}\right)\right] \tag{2.29}$$

where x is the variable, and λ and κ are the location and scale parameters, respectively.

Fréchet distribution

Fréchet EVD is known as EVD type 2. Same as Gumbel, it is also used to model maximum values in a given set of data. It is common in applications such as flood analysis and human lifespans [30]. The CDF of Fréchet distribution is given by,

$$F_x(x) = \exp-\left(\frac{x-\lambda}{\kappa}\right)^{-\beta} \tag{2.30}$$

where x is the variable, λ, κ, and β are the location, scale, and shape parameters, respectively.

Weibull distribution

Weibull EVD is known as EVD type 3. It is commonly used in evaluating a product reliability by modeling failure rates. It is also used in representing numerous physical quantities including wind speed [32]. The CDF of the two parameters Weibull distribution is given by,

$$F_x(x) = 1 - \exp-\left(\frac{x}{\kappa}\right)^{\beta} \tag{2.31}$$

where x is the variable, κ, and β are the scale, and shape parameters, respectively.

Generalized extreme value distribution (GEV)

GEV is a type of the continuous probability distribution developed within the scope of extreme value theory and it combines Gumbel, Fréchet, and Weibull extreme value distributions. Same as the other EVD, it is also used to model the extreme values of a long sequential independent random variables [33].

The CDF of the GEV distribution is given as:

$$F(x; \lambda, \kappa, \beta) = \exp\left(-\left[1 + \beta\left(\frac{x-\lambda}{\kappa}\right)\right]^{-\frac{1}{\beta}}\right) \tag{2.32}$$

where λ, κ, β are the location, scale, and shape parameters of the distribution for the given random variable x.

The variation of the shape parameter β reforms the GEV distribution into one of the previously mentioned three EVDs.

1) When β is equal to zero, the GEV is equal to Gumbel
2) When β is greater than zero, the GEV is equal to Fréchet
3) When β is less than zero, the GEV is equal to Weibull

The parameters for all EVDs can be estimated based on the maximum likelihood method using the maximum values obtained from the time series from each seed. The extreme values can be calculated for a specified target probability of non-exceedance.

Chapter 3*

Numerical Model Set-up

3.1　General

This chapter will introduce the numerical model set-up for over-boarding and lowering phases in the software SIMA-SIMO [34]. The chapter includes sub-sections discussing:

1) The numerical model of lifting vessel, crane, and ballast system
2) The subsea template model for over-boarding and splash-zone crossing
3) The numerical model of the coupling elements
4) The frequency-domain analysis of the system
5) The settings for time-domain simulation and the environmental conditions setting applied in the models

The numerical models of the study case are set up using SIMA-SIMO [34]. An overview of the model can be seen in Figure 3-1. As previously mentioned in Section 1.3, the lifting operation for the subsea template can be divided into the following steps [10, 11]:

1) Pre-lift: In this stage, the vessel is within the designated location to carry out the operation. This is the last stage before the lifting starts.
2) Lift-off: The subsea asset is lifted from the vessel deck.
3) Over-boarding: The subsea asset is translated horizontally from the lift-off location to the lowering point over the sea.
4) Splash-zone crossing: The subsea asset is lowered through the free water surface where the wave kinematics is at its highest.
5) Lowering: The subsea asset is lowered further below the free water surface and closer to the landing position on the seabed.

6) Vessel positioning (optional): The vessel position can be adjusted in case that the deployment position is different from landing location.
7) Landing: The subsea asset is deployed on the seabed designated location.

The numerical models are set-up to study the operational limits for step 3 and step 4, The models consist mainly of five rigid bodies, the lifting vessel, the crane base, the crane boom, the crane hook, and the template.
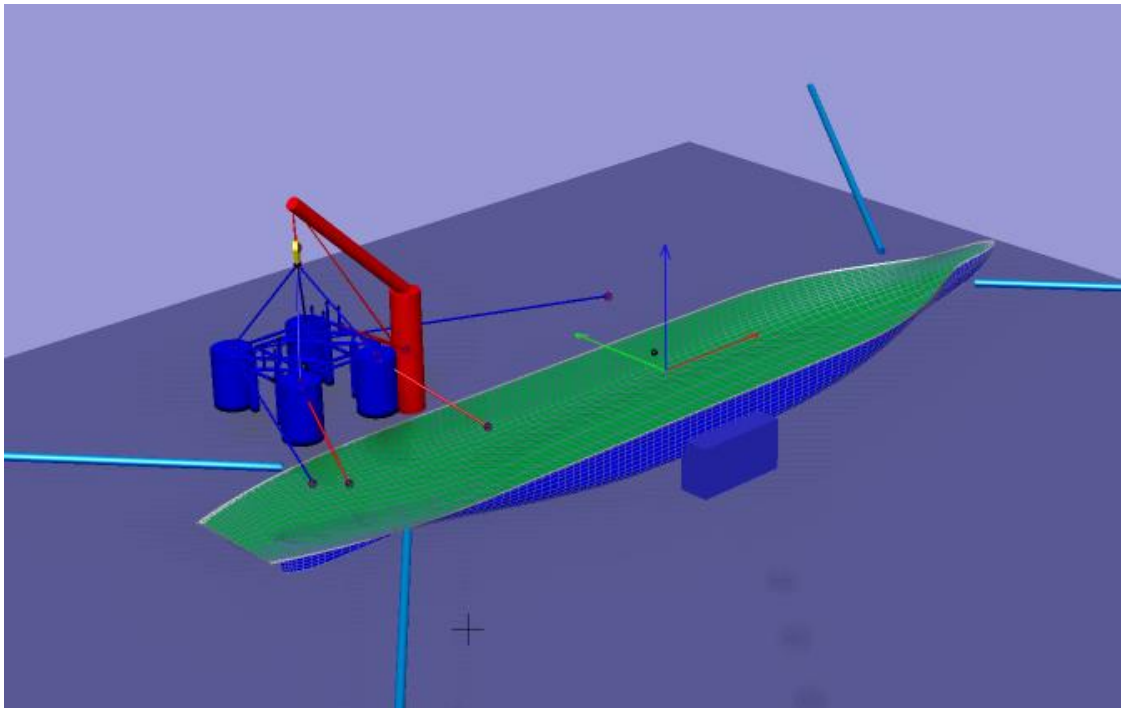
Figure 3-1 SIMA-SIMO model overview.

3.2 Lifting vessel

A typical offshore construction vessel is used for the operation. The vessel model was previously established by Parra in a different numerical study using SIMA-SIMO [35]. The vessel specifications are described in Table 3-1.

Table 3-1 Lifting vessel specification.

Item	Value
Length overall [m]	156.7
Length between perpendiculars [m]	143
Breadth [m]	27
Maximum draught [m]	8.5
Deadweight [t]	12000
Gross tonnage [t]	16954

3.2.1 Time-dependent mass (TDM)

During over-boarding,the template moves from the middle of the vessel to the port side, creating a heeling angle to the vessel. To maintain the stability of the vessel during the operation, the heeling angle should be balanced using a ballast system. In the numerical model, ballast tanks are modeled to pump in and out water to keep the vessel at a stable level during over-boarding.

The flow rate is estimated based on the rotational speed of the crane. Figure 3-2 shows the roll angle of the vessel with and without using the ballast system. It can be observed that without the ballast system, the mean roll angle is around 11 degrees when the template reaches the lowering position. This will affect the vessel performance for the lifting operation. The time history of the flow rate of the ballast system is also shown in Figure 3-2 The flow rate is within the capacity of the ballast system of the construction vessel, with a maximum flow rate of 2.1 m3/s.
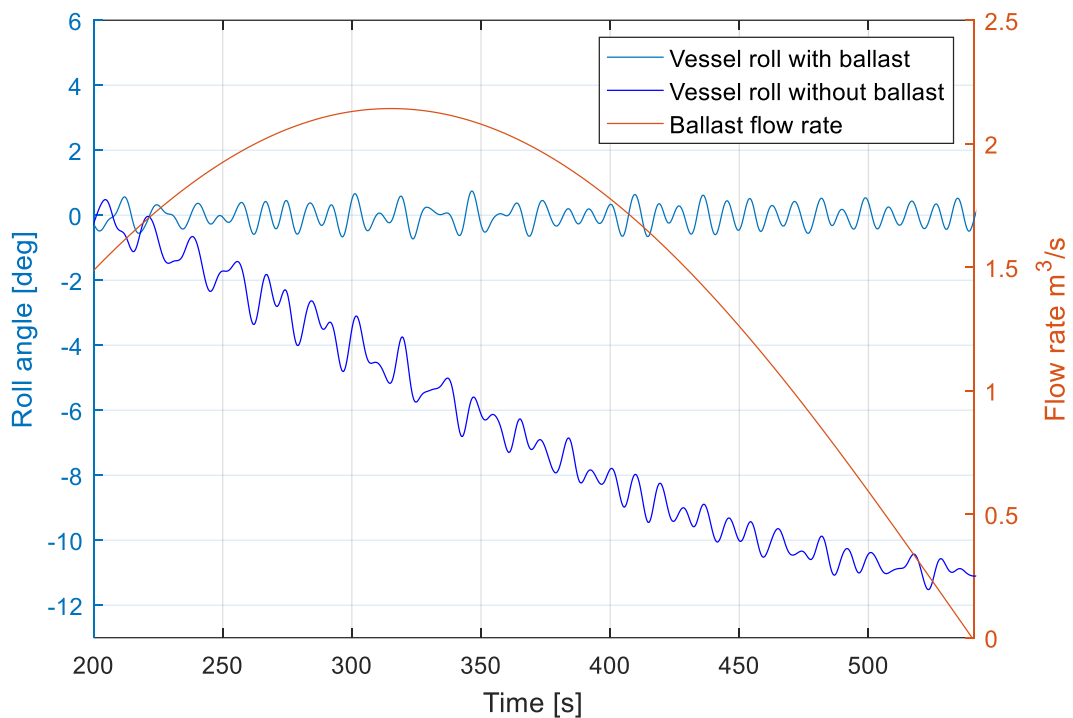
Figure 3-2. Comparison the vessel roll motions with and without using ballast system (Tp = 8s, Hs = 1.8m).

The ballasting effect was modeled by using two TDMs [34], one overcomes the template movement in the x-direction to eliminate the high pitch angle, while the other overcomes the movement in the y-direction to eliminate the high roll angle.

The following tables shows the TDMs points coordinates and the main parameters:

Table 3-2 TDMs coordinates.

	TDM for roll			TDM for pitch	
X	Y	Z	X	Y	Z
0	-15	-8	-15	0	8

Table 3-3 TDM main parameters.

	TDM for roll			TDM for pitch	
Initial volume[m^3]	Max flow rate [m^3/s]	Density [kg/m^3]	Initial volume[m^3]	Max flow rate [m^3/s]	Density [kg/m^3]
0	2.5	1025	903.4	2.5	1025

Initially, the template is placed on deck with its CoG in-line with the vessel center line and offset 50.449 m along the x-axis (see Figure 3-3). This will induce an initial pitching moment but without any rolling moment.
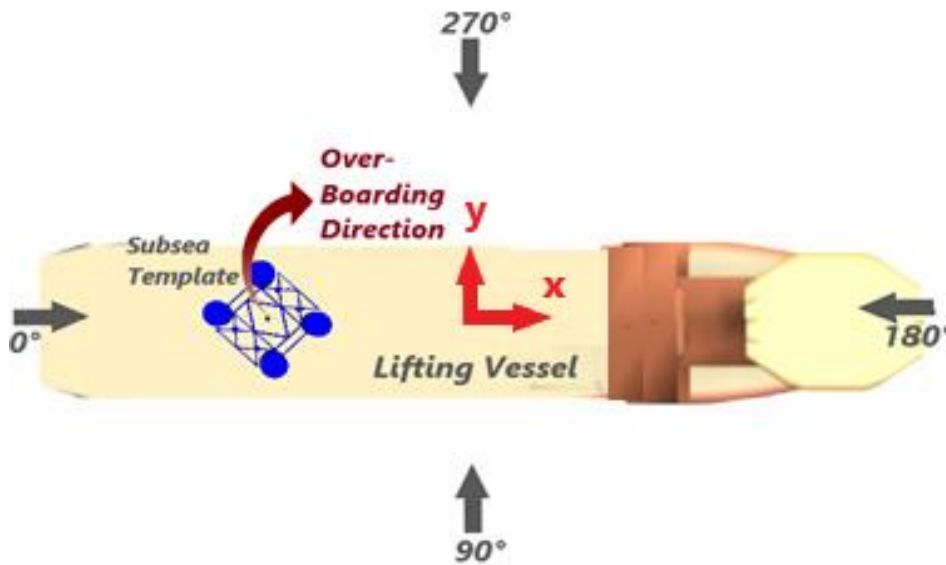
Figure 3-3 Modeled vessel and template in SIMO.

The translation motion in x and y direction was calculated by the following equations:

$$Y(t) = Y_c - R cos(\theta(t))$$
(3.1)

$$X(t) = X_c - R sin(\theta(t))$$
(3.2)

Y_c is the crane base coordinate in y-direction , X_c is the crane base coordinate in x-direction, R is the crane working radius between the template COG (crane tip) and the crane base, $\theta(t)$ is the angle between the original and the new template coordinate at each second.

The calculated coordinate of the template at each second of the operation is used to develop a moment balance between the template and the ballasting system, thus to calculate the required ballast flow rate.

$$W_t * Y(t) = m_r(t) * g * Y_r \tag{3.3}$$

$$W_t * X(t) = m_p(t) * g * X_p \tag{3.4}$$

W_t is the template weight force, $m_r(t)$ is the ballast water mass for roll, $m_p(t)$ is the ballast water mass for pitch, Y_r is the Y coordinate for the roll TDM and X_p is the X coordinate for the pitch TDM.

3.2.2 Crane model

The crane tip position is [-50.4 m, 0 m, 54.2 m] in the global coordinate when the system is at rest and the crane working radius is set to 18 m. Table 3-4 shows the crane technical specifications.

Table 3-4 Vessel's crane specifications.

Item	Value
Max. lift capacity [tons]	400
Min. lift radius [m]	10
Max. lift radius [m]	40
Max. lift height [m]	53
Crane base diameter [m]	4.4
Crane boom diameter [m]	1

Each of the crane parts is modeled as an articulated structure body. The articulated structure are connected in a master-slave relation. Each slave has a pre-described type of motion and each body may be specified to move along or around one of the DoF of its master body [36].

According to SIMO user manual, the following must be considered when the articulated structure is being modeled [36]:

1) The main master of the articulated structure cannot be an articulated structural member.

2) Each of the members must have a body-fixed coordinate system.

3) The link between a master and a slave member must not be disconnected at all.

4) The relative motion between the slave and the master can only take place along or around one of the principal axes of the master's coordinate system.

5) The series of bodies must not be arranged in loops

For simplicity, only two parts are used to model the crane in SIMO, the base, and the line. The vessel is defined as the main master body for the crane base and the motion sequence for the crane base is set according to Table 3-5.

Table 3-5 Crane motion sequence in SIMO.

Item	Value
Motion mode	Rotation around Z-axis (ψ)
Initial position [deg]	-43.75
Final position limit [deg]	-180
Rotational speed [deg/s]	-0.4
Acceleration [deg/s^2]	2
Motion start Time [s]	200
Motion stop Time [s]	540.5

The crane base is defined as a master body for the crane boom, as a result, the crane boom follows the same motion sequence that is defined for the crane base. An initial tilting angle is set around the crane boom local x-coordinates to ensure that the crane tip is 42m above the template CoG.

3.3   Subsea template model in SIMO

A typical subsea template is to be installed on the seabed. Figure 3-4 presents the side and top views of the subsea template, where the position of the CoG is highlighted.

The total length of the subsea template is 20.8 m and the width is 17.4 m. The overall height of the template, from the bottom of the suction anchors to the top of the guideposts, is 12.9 m. The template body mainly consists of four hollow suction anchors, four hollow washout sleeves, and eight guideposts attached to the top of the template.

The total mass of the template is 263 tons. The dimensions of the main tubular members of the template are listed in Table 3-6. The hoisting system for the template lifting operation includes the crane lift wire, slings, and the winch.

The slings connect the template to the hook of the crane block, and the lift wire is between the crane block and the crane tip. Because of the large dimension of the template structure, four slings on top of the four suction anchors are arranged to distribute the loads on the template.
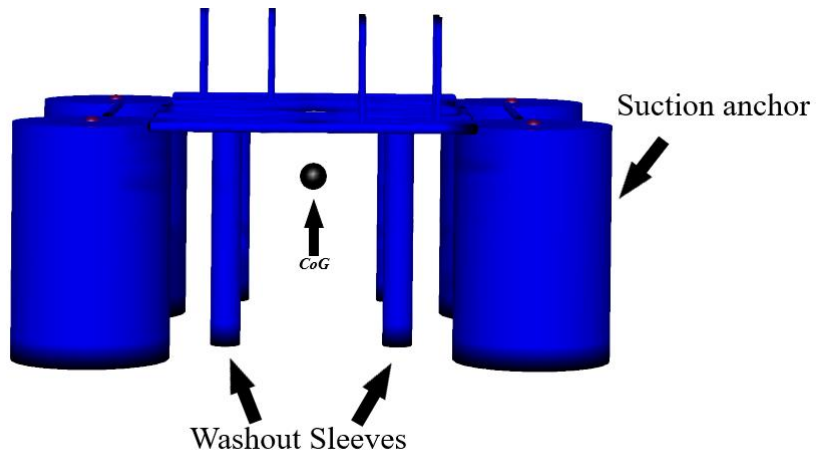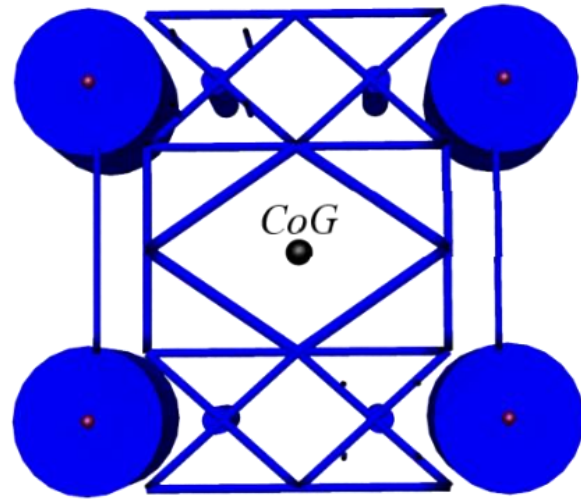
Figure 3-4 Template model top and sideview in SIMA-SIMO for over-boarding phase.

Table 3-6. Subsea template specification.

Item	Value
Overall height [m]	12.9 m
Overall length [m]	20.8 m
Overall width [m]	17.4 m
Mass dry in air [ton]	263 ton
Suction anchors outer diameter [m]	5.5 m
Washout sleeves outer diameter [m]	0.98 m
Suction anchors and washout sleeves wall thickness [m]	0.02 m
Suction anchors height [m]	8.225 m
Washout sleeves height [m]	7.725m
Carbon steel density [kg/m^3]	7850 kg/m^3

3.3.1 Slender elements

For large volume bodies, such as the template, slender elements can be defined to construct the body shape, volume and mass. These elements are defined within the body local coordinate system with a specific volume, and distributed mass [34]. 36 slender elements are used to construct the template body in SIMO for the over-boarding phase.

The template model requires modification for the lowering phase compared to over-boarding. The upper structure is modeled by using four slender elements only to avoid complexity when introducing the hydrodynamic calculations to the model. Each suction anchor is now modeled using three slender elements instead of one in order to accurately distribute the hydrodynamic forces across each anchor. Figure 3-5 shows the new template model in SIMO for the lowering phase.
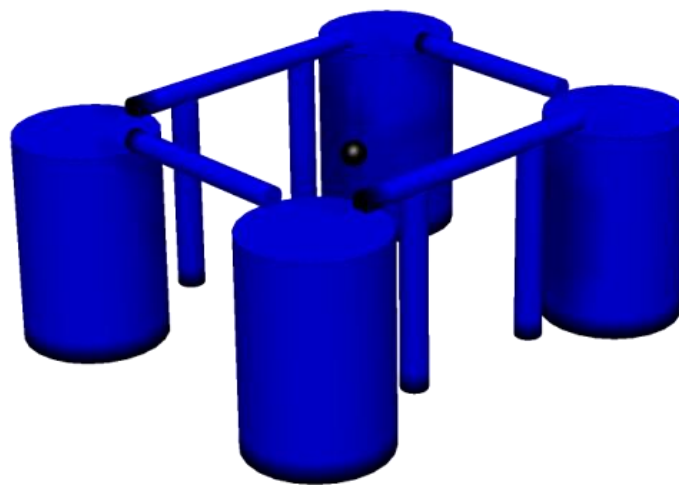
Figure 3-5. Template model in SIMO for splash-zone crossing phase.

The contribution from each of the slender elements to the mass matrix of the main body is calculated and added in the local body coordinates. After computing the mass matrix, SIMO can output both the CoG local coordinates and the total mass of the main body [34]. The CoG coordinates and the mass of the template in SIMO are compared with the actual values. It can be seen from Table 3-7 and Table 3-8, that the deviation is minimum and the model accuracy is adequate.

Table 3-7 Template modeled and actual CoG.

CoG coordinates in SIMO			Actual CoG coordinates		
X	Y	Z	X	Y	Z
0	0	-1.297	0	0	-1.293

Table 3-8 Template modeled and actual mass.

Mass in SIMO [ton]	Actual mass [ton]
263.33	263

3.3.2 Estimation of added mass and damping for the template

Before the estimation of the added mass and damping is carried out, the validity of Morison's equation in section 2.3.1 must be checked. This validation is performed by utilizing Eq. **(2.14)** and **(2.15)** for the operational range of peak periods.

The water depth of the subsea filed is approximately 115m and $k = 2\pi\lambda^{-1}$

$$\lambda = T\sqrt{\frac{9.81}{k}\tanh(k*115)}$$

Table 3-9 Calculated wave length at given peak periods.

Tp [s]	6	8	10	12
λ [m]	55	99	154	222

The structural element with the largest diameter is the suction anchor with a value of 5.5m (see Table 3-6). At 6s peak period,

$$5*D = 27.5\ m, \qquad \lambda > 5D$$

Thus, the use of Morison's equation to estimate the slamming loads acting on the subsea template is valid for the operational peak period range.

3.3.2.1 Estimation of added mass

Horizontal added mass for suction anchors

The horizontal added mass for the suction anchors is estimated by DNVGL-RP-N103 [11], as shown in Figure 3-6.
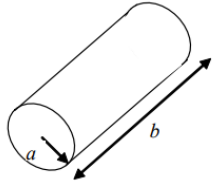
Table A-2 Analytical added mass coefficient for three-dimensional bodies in infinite fluid (far from boundaries). Added mass is $A_{ij}=\rho C_A V_R$ [kg] where V_R [m³] is reference volume (Continued)

Body shape		Direction of motion	C_A		V_R
			$b/2a$	C_A	
Right circular cylinder		Vertical	1.2	0.62	$\pi a^2 b$
			2.5	0.78	
			5.0	0.90	
			9.0	0.96	
			∞	1.00	

Figure 3-6. DNV-RP-N103, Added mass for circular cylinder [11].

Each anchor has a height to diameter ratio (H/D) equal to 1.5 , by linearly interpolating the data in Figure 3-6 the added mass coefficient C_a is 0.656. The horizontal added mass for one suction anchor is then calculated from Eq. **(2.17)**,

$$A_{33H} = 1025 * 0.656 * V \tag{3.5}$$

The mass of water inside the anchor will come to addition. With a wall thickness equal to 0.02 m, the mass of water inside will be 197 tons for each anchor. Thus, the total added mass in the horizontal direction for one anchor is then 328 tons.

Vertical added mass for suction anchors

Due to the nature of the suction anchor geometry, the vertical added mass is equal to the mass of the water inside a cylinder with the same dimensions as the anchor plus a sphere of water with a radius equal to the radius of the anchor [17]. This is can be further illustrated in Figure 3-7.
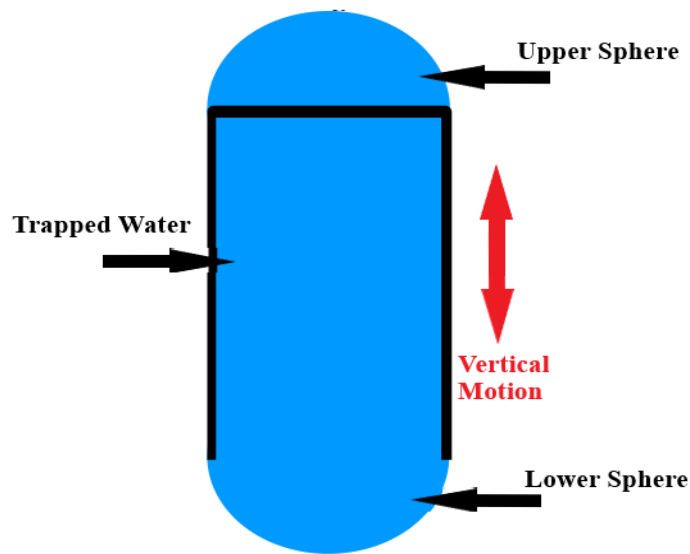
Figure 3-7. Suction anchor vertical added mass illustration.

The vertical added mass A_{33o} is found to be equal to 290 tons from the following equation when the top hatches are closed,

$$A_{33o} = \rho \pi a^2 \left(b + \frac{4}{3} a \right) \tag{3.6}$$

In actual operation, the top hatches are normally open and thus a perforation effect of 6% for each suction anchor takes place. The perforation percentage will cause a reduction in the vertical added mass value according to the following expression from DNV-RP-N103 [11],

$$A_{33} = A_{33o} \left(0.7 + 0.3 \cos \left[\frac{\pi(p-5)}{34} \right] \right) \quad if \ 5 < p < 34 \tag{3.7}$$

where A_{33} is the perforated added mass in heave and p is the perforation percentage. The perforated added mass is then equal to 261 tons for each suction anchor.

Added mass for top structure

Four slender elements equal in mass and volume to the actual structure are used to distribute the structure hydrodynamic forces. The horizontal and vertical added mass for the top structure are estimated by DNVGL-RP-N103 [11] and is equal to 51 tons.

Added mass for washout sleeves

The washout sleeves act as a funnel and do not have a vertical added mass contribution. From Figure 3-6, when H/D is 7.9, the added mass coefficient C_a is 0.94 through linear interpolation. The horizontal added mass for one guide funnel according to Eq. **(2.17)** is,

$$A_{33H} = 1025 * 0.94 * V \qquad \text{(3.8)}$$

With a wall thickness of 0.02 m, the mass of the water inside will be 6 tons. Thus, the total added mass in the horizontal direction for one cylinder is then equal to 12 tons.

3.3.2.2   Estimation of damping

Horizontal damping for suction anchors

The horizontal damping for the suction anchors is estimated by DNVGL-RP-N103 [11]. From Figure 3-8, when H/D is 1.5, the reduction factor κ is 0.5733 through linear interpolation.
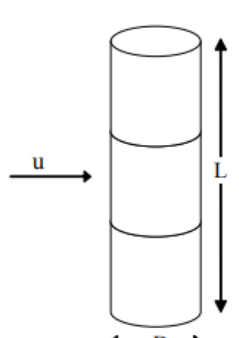
Circular cylinder normal to flow.	L/D	Sub critical flow $R_e < 10^5$	Supercritical flow $R_e > 5 \cdot 10^5$
		κ	κ
	2	0.58	0.80
	5	0.62	0.80
	10	0.68	0.82
	20	0.74	0.90
	40	0.82	0.98
	50	0.87	0.99
	100	0.98	1.00

$$C_{DS} = \kappa C_{DS}^{\infty}$$

κ is the reduction factor due to finite length. C_{DS}^{∞} is the 2D steady drag coefficient.

Figure 3-8. DNV-RP-N103, Damping for circular cylinder normal to flow [11].

As shown in section 2.3.2, the steady drag coefficient $C_{DS}(\Delta)$ for rough cylinders is equal to 1.05. From Figure 3-9, the wake amplification factor $\psi(K_c)$ is 2.1 when the assumed KC number of the flow is 12. Thus, C_{DS}^{∞} can be calculated from Eq. **(2.19)**,

$$C_{DS}^{\infty} = 2.2 * 1.05 = 2.31$$

By substituting in the equation given in Figure 3-8,

$$C_{DS} = 2.31 * 0.5733 = 1.33$$
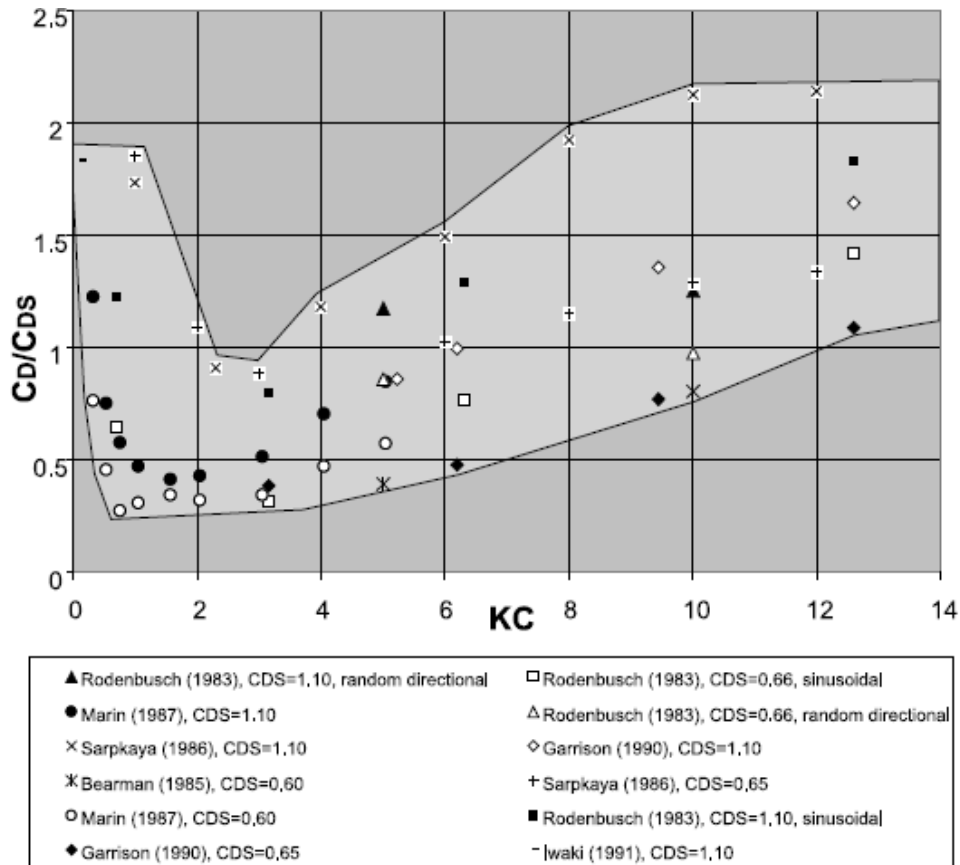
Figure 3-9 Wake amplification factor [11].

The normal drag force as a function of flow velocity can then be calculated from the drag term in Eq. **(2.13)**,

$$\frac{F_D}{u|u|} = \left(\frac{1}{2}\right)(1.33)(1025)(A)\left[\frac{Ns^2}{m^2}\right]$$ **(3.9)**

The tangential drag coefficient C_{Dt} can also be calculated from Eq. **(2.18)**. Since the incident angle α is either 90 or 0 for each template element,

$$C_{Dt} = 0 \ \ at \ \alpha = 90, \ \ \ C_{Dt} = (C_{DS} * m) \ \ at \ \alpha = 90$$

From Table 2-1, m is 0.03 and so C_{Dt} is 0.04 at $\alpha = 90$. When C_{Dt} is substituted in Eq. **(2.16)**, the obtained tangential drag force is significantly small and can neglected.

Vertical damping for suction anchors

Another method of estimating the perforated added mass and damping for anchors is using actual measured data from lab experimental modules. Solaas and Sandvik performed experimental studies to provide accurate measurement of hydrodynamic coefficients for suction anchors [37]. The study utilized free oscillation decay tests for various suction anchors with different H/D ratios. The obtained results from their study are used in estimating the vertical damping of each suction anchor.

Figure 3-10 includes the linear damping data for anchors having a diameter of 5m and a height of 8.9m. [37]. The suction anchor in this study has a diameter of 5.5m and a height of 8.225m.
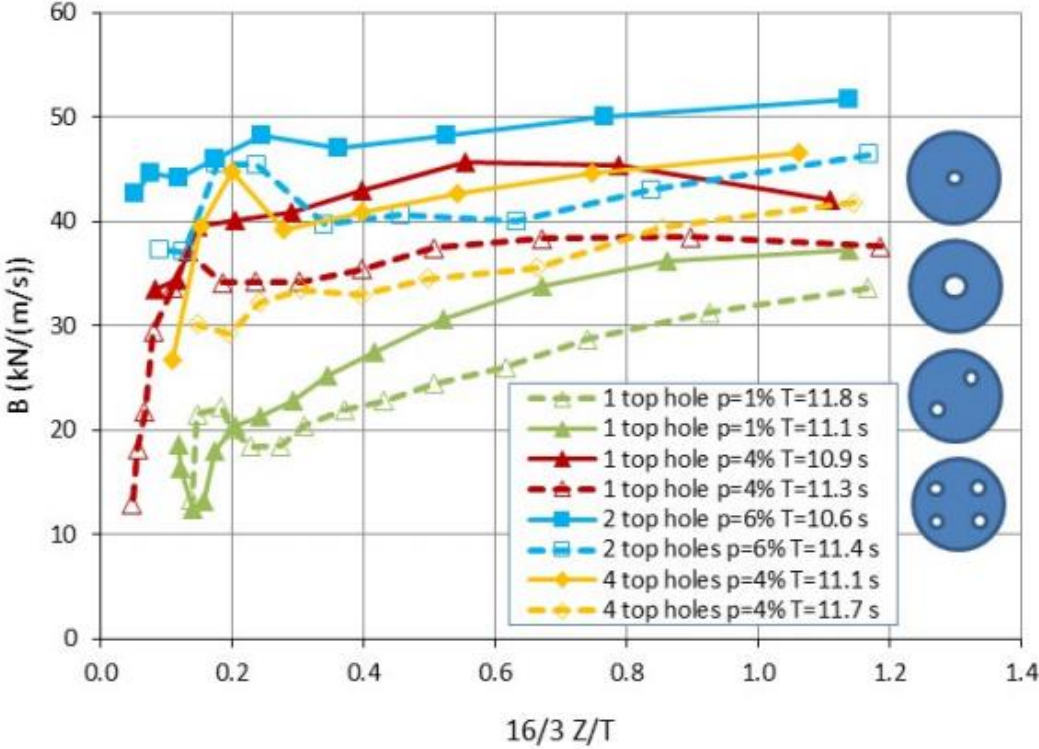
Figure 3-10 Damping for anchors with one or more top hole [37].

The damping is scaled with the diameter in the obtained template model, the vertical damping of each suction anchor with two top hatches and perforation of 6% is then equal to 57 KN.s/m.

Horizontal and vertical damping for washout sleeves

Same as the vertical added mass, the washout sleeves have no vertical damping contribution. The horizontal damping is calculated from DNVGL-RP-N103 with the same procedure used in the section anchor calculations. From Figure 3-8, when H/D is 7.9, the reduction factor κ is 0.6546 through linear interpolation. Thus,

$$C_{DS} = 2.31 * 0.6546 = 1.51$$

From the drag term in Eq. **(2.13)**,

$$\frac{F_D}{u|u|} = \left(\frac{1}{2}\right)(1.51)(1025)(A) \left[\frac{Ns^2}{m^2}\right] \tag{3.10}$$

3.3.3 Slender elements inputs in SIMO

In order to assign the hydrodynamic forces correctly in SIMO, the local coordinate system for the utilized slender elements in the model must be first reviewed from SIMO user manual [36].
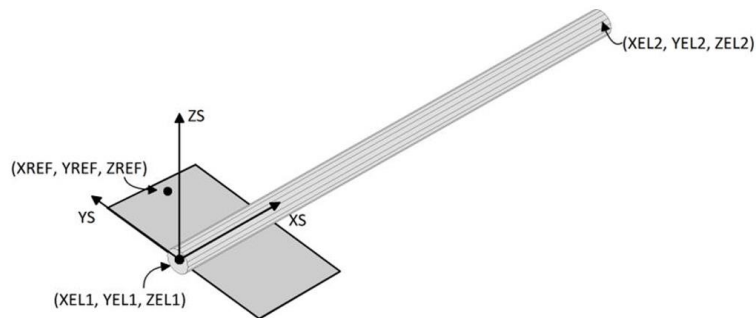
Figure 3-11 Coordinate system [XS,YS,ZS] of the slender element [36].

Figure 3-11 indicates that the x-axis is the longitudinal axis of the element, while the y-axis and z-axis are the lateral ones. Thus, the axial components of the hydrodynamic forces will be presented by the x-axis and the normal components will be presented by the y and z-axis.

For each anchor, a vertical element with the same height as the anchor takes care of the mass distribution, volume, horizontal added mass, and horizontal damping. Input to one of the vertical elements is shown in Table 3-10.

Table 3-10 Input to slender element model considering horizontal forces on the suction anchor.

Item	Value
$C_{2x}[Ns^2/m^3]$	0
$C_{2y}[Ns^2/m^3]$	5800
$C_{2z}[Ns^2/m^3]$	5800
$A_{mx}[kg/m]$	0
$A_{my}[kg/m]$	39910
$A_{mz}[kg/m]$	39910

where C_{2x}, C_{2y}, C_{2z} are the quadratic drag components, and A_{mx}, A_{my}, A_{mz} are the added mass components in x, y, and z directions according to the local coordinate system in Figure 3-11. C_{2y}, C_{2z}, and A_{my}, A_{mz} are obtained by dividing Eq. **(3.9)** and **(3.5)** over the length of the slender element.

The hydrodynamics of the suction anchor top is distributed on two different elements. One small element located at the bottom of the anchor takes care of the hydrodynamic forces that may give slamming forces.

The element is located on the anchor tip because it is more correct to use the wave kinematic at the entrance of the anchor to calculate the forces than to use the kinematic at the free surface outside the anchor. Depth-dependent coefficients (DDC) are used to ensure that the forces

appear when the suction anchor roof at the free water surface. The inputs for one of those elements is shown in Table 3-11 and Table 3-12.

Table 3-11 Input to the small slender element model considering the force when the free surface reaches the top of the suction anchor inside the anchor.

Item	Value
$C_{1x}[Ns/m^2]$	5.7e+05
$C_{1y}[Ns/m^2]$	0
$C_{1z}[Ns/m^2]$	0
$A_{mx}[kg/m]$	2.42e+06
$A_{my}[kg/m]$	0
$A_{mz}[kg/m]$	0

where C_{1x}, C_{1y}, C_{1z} the linear drag components in x, y, and z directions according to the local coordinate system in Figure 3-11. C_{1x} is equal to the vertical damping of the anchor divided by the small slender element length. The small element length is 0.1m and the obtained vertical damping from Figure 3-10 is 57000 N.s/m. A_{mx} is the sum of the perforated mass of the trapped water and the lower half of the water sphere divided by the element length (see Figure 3-7).

Table 3-12 DDC input for suction anchor small bottom element.

Slender element depth in water [m]	RLx	RAMx
0	0	0
-0.1	0.1	0
-8.025	0.1	0
-8.125	0.8	0.9
-8.225	1.0	1.0

where RLx is the relative linear drag in the element x-direction. RAMx is the relative added mass in the element x-direction. From Table 3-12, it is seen that the forces are turned on when the element is submerged between 8.125 and 8.225 m.

One element located at the top of the anchor representing the added mass due to the water above the anchor and damping due to the flow through the ventilation hatches at the top of the anchor when the anchor is submerged. The input to this element is shown in Table 3-13 and Table 3-14.

Table 3-13 Input to the top slender element considering added mass due to water above the anchor and flow through ventilation holes when the anchor is submerged.

Item	Value
$C_{2x}[Ns^2/m^3]$	0
$C_{2y}[Ns^2/m^3]$	5800
$C_{2z}[Ns^2/m^3]$	5800
$A_{mx}[kg/m]$	2.32e+05
$A_{my}[kg/m]$	39910
$A_{mz}[kg/m]$	39910

A_{mx} is equal to the perforated added mass of the upper half of the water sphere divided by the top slender element length. The element has a length of 0.02m, which is equal to the anchor wall thickness.

Table 3-14 DDC input for suction anchor top element.

Slender element depth in water [m]	RLy, RLz	RAMx	RAMy, RAMz
0.1	0	0	0
0	1.0	0.8	1.0
-1.0	1.0	1.0	1.0

where RLy and RLz are the relative linear drag in the element y and z directions. RAMy and RAMz are the relative added mass in the element y and z directions.

3.3.4 Water filling

Water filling of the hollow elements of the template is modeled as TDM. The filling rate and time instant for start and stop are adjusted to winch speed and measured hook load. The water filling starts when the template is fully submerged with a filling rate of 144.4 kg/s. As the filling starts, the template submerged weight increases and thus increasing the load on the lifting wire and slings.

3.4   Couplings elements

3.4.1 Fender couplings

Fender coupling is a contact element, the contact can be between a body and a fixed point in the global coordinate system, or between two bodies. The latter approach is used to define a fender plane on the vessel where the template can lay on by four fender points, one point for each suction anchor. The fender point is defined in the local template coordinate system [34].
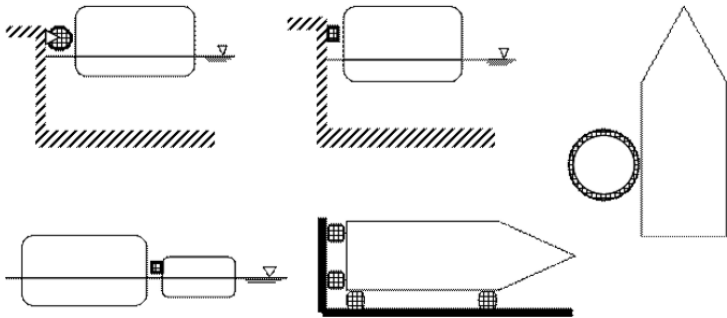
Figure 3-12 Fender coupling in SIMO [34].

The force from a fender will be zero if the projection of the fender point on the fender plane is outside the rectangle of the fender plane and also if the fender point enters the fender plane from below [34].

There are mainly three components that define the fender couplings, these components are friction coefficients, shear stiffness, and damping exponent. After these three main values are set, bot friction force and damping activation distances are defined [34].

The following are the local coordinates of the fender points on the template:

Table 3-15 Fender points coordinates.

Template fender points	X	Y	Z
Fender point 1	7.6955	6.25	-7.225
Fender point 2	7.6955	-6.25	-7.225
Fender point 3	-7.6955	6.25	-7.225
Fender point 4	-7.6955	-6.25	-7.225

The friction coefficients are chosen based on steel-to-steel friction [35]. The main properties of the fender couplings used in the numerical model are summarized in Table 3-16.

Table 3-16 Fender coupling properties.

Item	Value
Dynamic friction coefficient	0.42
Static friction coefficient	0.78
Shear stiffness [N/m]	4.68e+07

3.4.2 Simple wire coupling

The simple wire coupling is modeled as a linear spring which has the following general tension relation [34]:

$$F_T = k * \Delta l$$

(3.11)

where F_T is the tension force, k is the effective axial stiffness and Δl is the wire elongation.

The effective axial stiffness is also given by [34]:

$$\frac{1}{k} = \frac{l}{EA} + \frac{1}{k_o}$$

(3.12)

where E is the modulus of elasticity A is the wire cross-section area and k_o is the crane member flexibility.

The hoisting system for the template lifting operation includes the crane lift wire, slings, and the winch. The slings connect the template to the hook of the crane block, and the lift wire is between the crane block and the crane tip. Because of the large dimension of the template structure, four slings on top of the four suction anchors are arranged to distribute the loads on the template.

The symmetrical distribution of the template mass facilitates the required slings arrangements for lifting and handling the template in the air during the operation. The lifting wire ends are connected to the hook and the crane base through a guide point located at the crane tip. The crane base connection point also acts as the winch point, which is responsible for setting the lift-off and lowering motion sequence in the numerical model. Table 3-17 illustrates winch settings.

Table 3-17 Crane winch settings.

Item	Value
Acceleration [m/s^2]	2
Speed [m/s]	-0.03
Maximum length [m]	200
Drum length [m]	200
Motion start Time [s]	100
Motion stop Time [s]	200

The main lifting wire and slings properties are represented in Table 3-18 and

Table 3-19.

Table 3-18 Lifting wire properties.

Item	Value
Unstretched length [m]	39.8
Connection flexibility [m]	1.3e-07
Damping [N/m]	1.0e+07
Cross section stiffness [N]	1.2038e+09
Breaking strength [N]	1.329e+07

Table 3-19 Lifting slings properties.

Item	Value
Unstretched length [m]	18.189
Connection llexibility [m]	1.3e-07
Damping [N/m]	6.16e+06
Cross section stiffness [N]	3.08e+08
Breaking strength [N]	6.1684e+06

3.4.3 Fixed elongation coupling

Fixed elongation couplings are used to model the tugger lines [34]. Tugger lines are often used in the over-boarding operation to constrain the horizontal motions of the template [11]. Usually, the constant tension mode of the tugger winches can be used, where the winches automatically pay out and pay in to compensate the relative motions and to keep a stable tension in the lines during the operation. In the numerical model, two tugger lines are included between the crane

and the template, and four more tugger lines between the vessel deck and the template. The lines are controlled by tugger winches under constant tension mode. For the over-boarding operations of large structures, both crane and deck tugger lines are necessary to control the motions of the structures during the operations. Some of the tugger lines are activated during the whole operations, while the others are only activated for a limited time, depending on the locations of the winch and the operation requirement. In this study, crane tuggers are used in different models with and without deck tuggers to study the influences of the deck tugger lines on the responses.

The two main crane tugger lines are designed to operate continuously at constant tension during the whole over-boarding phase. However, three deck tugger lines are designed to operate only at certain periods of the operation by defining the engaging and disengaging distances. The arrangement of all the tugger lines are illustrated in Figure 3-13, and their identities in the numerical models are given. The engaging and disengaging distances of the tugger lines are presented in Table 3-20. The defined distance ensures that each tugger line operates at its intended period and disengages right after to make sure that the tugger line does not interfere in other sequential operations. In the numerical model, gradual buildup and decay for the tensions in the tugger times are also implemented when engaging and disengaging the tugger lines. This is to minimize the transient effects on the motions of the template due to the shift of tugger lines.

The operating sequence of the deck tugger lines are summarized as below:

1.   SternL tugger line is engaged at the start of the lift-off at 100s and disengage at around 200s when the lift-off is finished.

2.   Soon after, Starb is activating in the period from around 200s (over-boarding start) until 370s (halfway through the over-boarding phase).

3.   Finally, Bow tugger line takes over at the last phase of the over-boarding process until the end of the simulation.

The remaining deck tugger line, SternR is engaging during the whole simulation to support the main crane tugger lines and to minimize the motions of the template when the other three tugger lines are disengaged. All these tugger lines should contribute in controlling the horizontal motions of the template induced by the vessel motions in order to improve the operational limits, especially at higher sea states.

Table 3-20 The engaging and disengaging distances for deck tugger lines in the numerical model.

Tugger line name	Engaging distance	Disengaging distance
SternL	0 m	12 m
Starb	12.7 m	17 m
Bow	0 m	50 m

Three different tugger line arrangements (TLA) are used later in the numerical study to compare the influences of the tugger lines on the performance of the lifting system.

1) Only the main crane tugger lines with constant tension mode of 5 tons (TLA1).

2) Main crane tugger lines of 5 tons tension together with all deck winches with tensions of 2 tons (TLA2).

3) Main crane tugger lines of 5 tons tension together with all deck winches with tensions of 5 tons (TLA3).
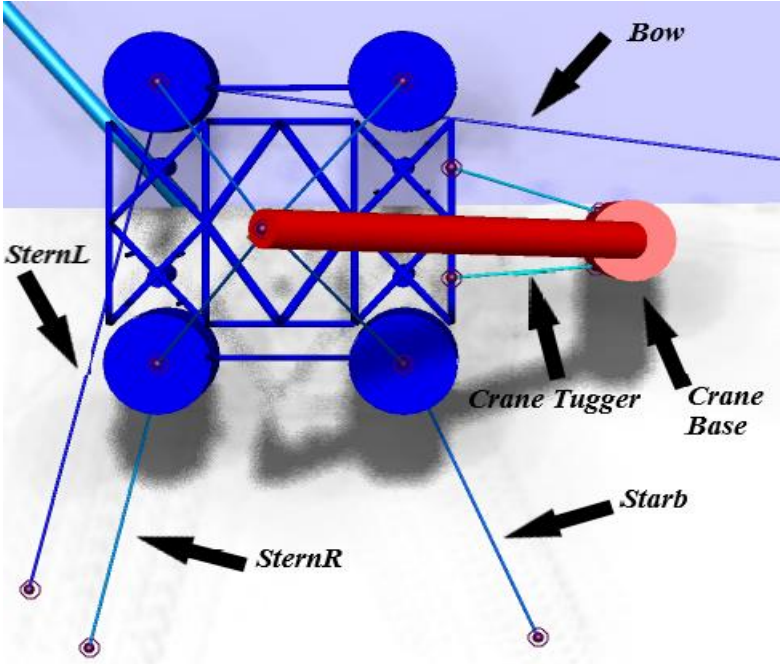
Figure 3-13 Deck winches tugger lines and crane model.

3.5   Eigenvalue analysis

Unlike splash-zone crossing, in over-boarding, the template does not maintain the same relative position to the lifting vessel in the XY plane. Thus, the template critical pendulum response will change depending on the system natural periods at a given template position. The eigenvalues of the system are first obtained from the static analysis in SIMA-SIMO in order to assess the natural periods of the system before evaluating the time-domain simulation results [36]. Eigenvalue analysis is conducted in frequency domain, without including any external forces or damping effect. The natural periods can be obtained by solving the following equation:

$$[-\omega^2(\boldsymbol{M} + \boldsymbol{M}_a) + \boldsymbol{K}] \cdot \boldsymbol{x} = 0 \qquad \textbf{(3.13)}$$

where, ω is the natural frequency; M and M_a are the mass and added mass matrices of the system; K is the stiffness matrix, and x is the motion vector.

3.5.1 Eigenvalue analysis of the installation vessel

Table 3-21 shows the natural periods of the installation vessel alone. Only three modes are within the typical sea waves peak periods range, i.e., modes 1, 2 and 3. These modes are dominated by the vessel pitch, heave, and roll motions, respectively.

Table 3-21 Eigenvalue analysis for the installation vessel.

	Mode	1	2	3	4	5	6
Vessel	Surge[m]	-0.15	0.01	0	0	0.02	**1**
Vessel	Sway[m]	0	-0.01	-0.07	0.14	**-1**	0.01
Vessel	Heave[m]	-0.02	**-1**	0	-0.01	0	0
Vessel	Roll[deg]	0	0.07	**-1**	-0.01	0.03	0
Vessel	Pitch[deg]	**1**	0.28	0	-0.05	0	0
Vessel	Yaw[deg]	-0.01	0.03	0	**1**	0.19	0
Natural period[s]		6.73	8.02	12.69	57.04	82.75	87.1

3.5.2 Eigenvalue analysis of the coupled system

For simplicity and easier identification of the modes, the hook is neglected when calculating the eigenvalues for the coupled system of the vessel and the template. Thus, the coupled system has 12 DoFs corresponds to 12 modes in total. The eigenvalues are obtained from static analysis with the vessel and the template as well as the corresponding tugger lines included in the system. The two most critical positions for the template during the operation are chosen based on the dynamic response in the time-domain simulation, which will be discussed later. The first location is at the end of the 1/3 over-boarding process, and the second location is at the end of the over-boarding. Thus, the eigenvalues of the coupled system are obtained and evaluated when the template reaches these locations. The results are presented in Table 3-22 and Table 3-23.

Table 3-22 Eigenvalue analysis for the coupled system at the end of the over-boarding.

	Mode	1	2	3	4	5	6	7	8	9	10	11	12
Vessel	Surge[m]	0	0	0	-0.01	-0.08	0	0	0	-0.04	0	0.09	0.23
Vessel	Sway[m]	0	0	0	0.06	-0.05	-0.04	0	0	-0.02	0	-0.08	0.28
Vessel	Heave[m]	0	0	0	0.02	-0.02	**0.79**	0	0	0	0	0	0
Vessel	Roll[deg]	0	0	0	**1**	**-1**	**-1**	0	0	-0.03	0	-0.02	-0.02
Vessel	Pitch[deg]	0	0	0	0.06	0.7	-0.25	0	0	0	0	0	0
Vessel	Yaw[deg]	0	0	0	0.02	-0.07	-0.09	0	0	0.08	0	0.02	**0.37**
Template	Surge[m]	-0.06	0	0	0	0.01	0.06	-0.31	-0.01	0	0	0	-0.01
Template	Sway[m]	0	0.06	0	0	-0.01	-0.11	-0.01	0.29	0	0	0	0
Template	Heave[m]	0	0	**1**	0	0	0	0	0	0	0	0	0
Template	Roll[deg]	0.03	**1**	0.11	-0.01	-0.02	**-0.37**	-0.04	**1**	0.01	0	0.01	0
Template	Pitch[deg]	**-1**	0.02	0.02	0	-0.03	-0.2	**1**	0.04	-0.04	-0.02	-0.01	0.01
Template	Yaw[deg]	-0.01	0	0	0	-0.07	-0.03	0.02	0	**1**	**1**	**1**	**1**
Natural period[s]		0.54	0.71	1.01	3.46	6.68	7.97	8.07	8.31	22.68	27.15	33.67	69.39

	Mode	1	2	3	4	5	6	7	8	9	10	11	12
Vessel	Surge[m]	0	0	0	-0.04	-0.02	0	0	0	0	0.13	**-1**	-0.22
Vessel	Sway[m]	0	0	0	0.06	-0.05	0	0.01	0	0	0.14	**0.37**	**-0.79**
Vessel	Heave[m]	0	0	0	0.03	-0.04	0	-0.11	0	0	0	-0.02	0
Vessel	Roll[deg]	0	0	0	**1**	**-1**	0	0.26	0.01	0	**0.41**	**0.37**	0.05
Vessel	Pitch[deg]	0	0	0	0.23	0.2	0	0.04	0	0	-0.02	0	0.01
Vessel	Yaw[deg]	0	0	0	0.01	-0.07	0	0.02	0	0	**-0.39**	**-0.3**	**-0.76**
Template	Surge[m]	-0.06	0	-0.01	-0.01	0.06	**0.31**	0.1	0.01	0.01	-0.02	-0.05	0.01
Template	Sway[m]	0	-0.06	0.01	-0.02	0.02	-0.01	0.29	-0.29	-0.01	0.01	-0.06	-0.01
Template	Heave[m]	0	0	**1**	0	0	0	0	0	0	0	0	0
Template	Roll[deg]	0.03	**1**	-0.15	-0.06	0.06	0.03	**1**	**-1**	-0.04	0.03	-0.21	-0.01
Template	Pitch[deg]	**-1**	0.02	0.01	0.05	-0.21	**-1**	**-0.33**	-0.03	-0.05	0.06	0.17	-0.02
Template	Yaw[deg]	-0.01	0.01	0	0.07	-0.23	-0.27	0.16	-0.19	**1**	**1**	0.48	**-1**
Natural period[s]		0.54	0.71	1	5.06	7.1	7.83	7.96	7.99	13.88	27	32.05	69.94

From Table 3-22 and Table 3-23, among the 12 modes for each case, the natural periods for modes 4-8 are considered critical and they are among the operational wave period range. As can be seen, the modes are coupled with contributions from the vessel, as well as template rotational and translational motions.

In Table 3-23 when the template is in its final location of the over-boarding process, the pendulum modes are observed in modes 7 and 8 where the natural periods are close to 8s. In mode 7, the template pitch motion is dominating and with a relatively large contribution from the surge motion. The natural period increases to 8.3s in mode 8 and the pendulum response appears from the dominating roll combined with sway motion. The coupling between the vessel and the template can be clearly seen in mode 6, where the vessel roll and heave motions of the vessel induce the rotations of the template. Modes 9-12 are dominated by yaw motions of the template and the natural periods are outside the operational wave period range.

Compared to Table 3-22, the critical natural periods in Table 3-23 show minor differences when the template is located at the end of the first third of the over-boarding process. However, the dominating modes are different compared to the previous location. At the first third of the over-boarding, mode 6 is entirely dominated by the template pendulum motion, while at the end of over-boarding, this mode is dominated by the vessel roll and heave motions with less contribution from the template pendulum motion. Modes 7 and 8 are also dominated by the template pendulum motion in Table 3-23, and the vessel contribution is negligible. The differences in the contributions of different motions at the two positions are due to the change of the crane tip position, as well as the change of the deck tugger line engagement.

3.6   Time-domain simulation settings

3.6.1   Environmental conditions

The selected environmental conditions are listed in Table 3-24. Hs is the significant wave height, and Tp is the spectral wave peak period. For selected Tp, Hs will vary in order to search for the allowable sea states. At each combination of Hs and Tp the irregular waves are modeled by JONSWAP spectrum with a peak enhancement factor of 3.3. The directional spreading of

wave energy is considered using short-crested waves characterized by the wave spectrum S(ω) and the directional spreading function D(θ) [23]:

$$S(\omega, \theta) \ = \ S(\omega)D(\theta) \tag{3.14}$$

$$D(\theta) \ = \ \begin{cases} C(n)cosn(\theta - \theta_0) & |\theta - \theta_0| \leq \pi/2 \\ 0 & |\theta - \theta_0| \ > \ \pi/2 \end{cases} \tag{3.15}$$

where θ_0 is the main wave direction about which the angular distribution is centered. The parameter n is a spreading index describing the degree of wave short-crestedness with n $\rightarrow \infty$ representing a long-crested wave field. C(n)is a normalizing constant as follow:

$$C(n) = \frac{1}{\sqrt{\pi}} \frac{\Gamma(1 \ + \ n/2)}{\Gamma(1/2 \ + \ n/2)} \tag{3.16}$$

where Γ denotes the Gamma function. Consideration should be taken to reflect an accurate correlation between the actual sea state and the index n. In this study, a constant n = 2 is used in the spreading function, which is reasonable to represent wind-generated seas [23].

Table 3-24 Environmental conditions.

Item	Value
Wave spectrum	JONSWAP spectrum
Spreading type	Cosine function
Spreading index	2
Wave directions	180°
Peak period *Tp*	6s, 8s, 10s, 12s
Significant wave height *Hs*	Varies to find allowable sea state

3.6.2   Over-boarding phase simulation settings

The two time-domain simulation approaches are considered, i.e., the transient and the steady-state approaches. In both approaches, step-by-step integration methods are applied to solve the coupled equations of motion using an iterative routine. The equations of motion are solved by Newmark-beta numerical integration with a time-step of 0.02 s. The wave excitation forces on the construction vessel are pre-generated from the transfer functions obtained from the frequency-domain analysis at their mean positions using Fast Fourier Transformation (FFT). The radiation effects on frequency-dependent added mass and damping forces are included in terms of coupled retardation functions in the time domain. The coupling forces are directly calculated for each time step based on the relative motions between the bodies [34].

3.6.3   Splash-zone phase simulation settings

During the lowering phase, the calculation of wave responses for each time-step is performed by summing the cosine harmonic components with a time-step of 0.02 s. The calculations are

carried out for the instantaneous locations of each slender element of the template. This will give a more correct wave kinematics and load for each element as the template being lowered, it will also enable simulation of horizontal and vertical transport [34].

The time series generated will repeat themselves with a period $Tp = 2\pi/\Delta\omega_{k\ min}$, where $\Delta\omega_{k\ min}$ is the smallest increment of the frequency [34].

Chapter 4*

Operational Criteria

4.1 General

In this chapter, the operational criteria for both over-boarding and splash-zone crossing phases are discussed. This includes determining the extreme responses of each phase and the required statistical model. A properly fitted statistical model is essential for the study in order to provide a good estimate for the target probability of non-exceedance at any given sea state.

The extreme values are sensitive to the selection of the target probability of non-exceedance. Often, a value between 0.9 to 0.99 is used based on the associated risks of the operation. A high probability of non-exceedance may introduce high uncertainties in the extreme values when the sample size (seed number) is small [6].

4.2 Over-boarding phase operational criteria

In this study, 25 wave seeds are used for each sea state. A target probability of non-exceedance of 0.9 is considered to provide a reliable prediction of extremes, and thus is used in the assessment of the allowable sea states.

The horizontal motions of the template are considered as the critical responses. The operational criterion is to ensure that the extreme horizontal displacement of the template during over-boarding is within a limiting value. The limiting value is often decided based on the deck arrangement to avoid collisions with other equipment onboard. For the current lifting system, a limiting value of 3 m is used. Thus, the criterion to assess the allowable sea states is limiting the extreme pendulum motion of the template within 3 m. The extreme pendulum motion corresponds to a target probability of non-exceedance of 0.9.

*Section 4.2 of this chapter is included in a paper with the title 'Numerical Analysis of an Over-boarding Operation for a Subsea Template'. This paper has been submitted to the Journal of Ocean Engineering and Science.

To simulate the operation, two simulation approaches are normally used:

1.   A steady-state approach which is based on finding the most critical position for the template during the over-boarding phase and running the simulations at this position under various wave conditions.

2.   A transient approach which is based on repetitive simulation of the whole transient over-boarding phase with different irregular sea waves realizations.

Both approaches are used in this study to assess the allowable sea states for the over-boarding process.

4.2.1   Transient time-domain simulation approach

In the transient approach, the winch starts at 100 s to avoid initial transient effects with a constant speed of 0.03 m/sec for lift-off and stops at 200 sec. Then, the crane bottom starts to rotate at 200 sec. The whole simulation length is 1000 sec. Over-boarding takes place between 200 and 541s.

During the over-boarding process, the mean X and Y displacements of the template go through large changes due to the changing positions of the crane tip. In order to evaluate the dynamic pendulum motions, the mean values of the X and Y displacements need to be subtracted from the total motions. Figure 5 illustrates the mean and the total displacements of the template in X and Y directions during the over-boarding phase.

The coordinate system refers to Figure 4-1. The mean motions in the figure are calculated based on the crane tip positions in the still water with prescribed rotations.

The equivalent dynamic pendulum motion is then calculated from the combined X and Y displacement by subtracting their mean values. Thus, the pendulum motion at one suction anchor location is formulated as follows:

$$A = \sqrt{(A_x - \overline{A_x})^2 + (A_y - \overline{A_y})^2}$$

(4.1)

where, A is the equivalent dynamic pendulum motion for a given suction anchor location. Ax and Ay are the total pendulum motions in X and Y. $\overline{A_x}$ and $\overline{A_y}$ are the mean motions for the given anchor in X and Y.

However, it can be seen from Figure 4-1 that the motions of the crane tip in still water deviate from the actual mean motions from the dynamic time histories. As a result, the calculated equivalent pendulum motion from Eq. **(4.1)** will be higher than the true dynamic pendulum motions due to these differences.

These differences are caused by the defined engaging and disengaging mechanism of the deck tugger lines according to Table 3-20. In the real operation, the operators working onboard control this winch motion manually to reduce the dynamic effects and it is challenging to implement this manual interference in the transient approach.

When using the transient approach, 25 seeds are applied for each irregular wave condition. The maximum dynamic pendulum motions are obtained for all seed, and the extreme pendulum motions are calculated from the fitted Gumbel distribution
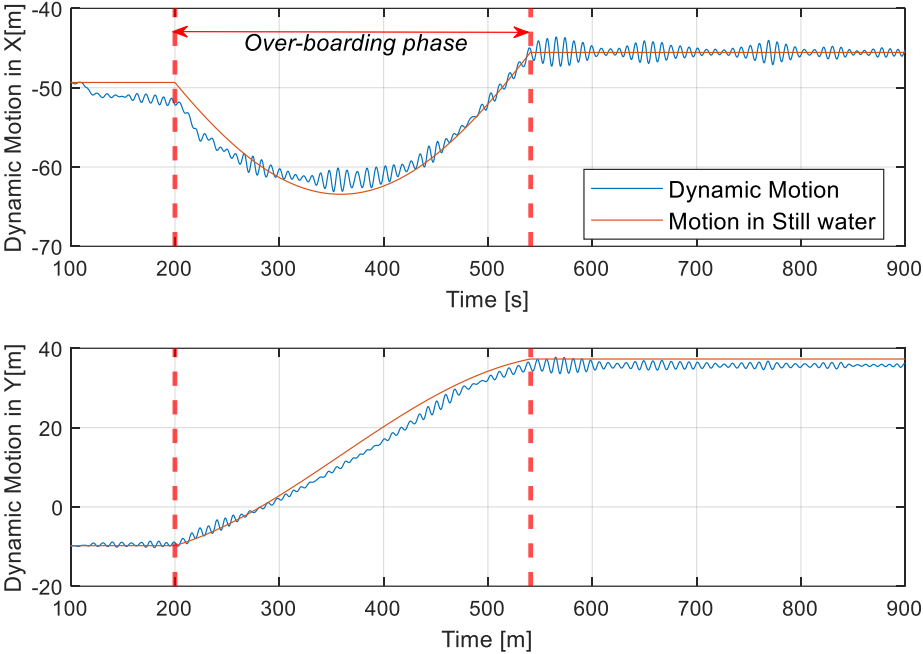

Figure 4-1 Comparison of crane tip motions in still water and at the sea state of Tp = 8s and Hs = 1.25m during the whole time-domain simulation.

.

To compare with the transient approach, the steady-state analysis is also used for the allowable sea state assessment in order to reduce the effect of the excessive motion of the system during the transient time-domain simulations.

4.2.2 Steady-state time-domain simulation approach

The steady-state approach is considered for the most critical crane tip positions based on the dynamic responses in the transient time-domain simulation. The first critical location is at the end of the 1/3 over-boarding process, and the second critical location is at the end of the over-boarding. The crane tip location is set at each critical position with no rotations to neutralize the dynamic effects of the crane rotation and to minimize the effects due to the engaging and disengaging of the deck tugger lines.

In this study, two different set up of simulation lengths are applied for each sea state when using the steady-state approach:

1.   Assume the system can stay at the critical positions for the whole over-boarding process (around 400s) and carry out the simulation for each sea state with a duration of 25 processes. (SS1)

2.　　Assume the system can stay at the critical positions only for a short period (150s) during the whole over-boarding process and carry out the simulation for each wave condition with a total of 3750s at the critical positions. This corresponds to 25 seeds of simulation with 150s each. (SS2)

In the first approach, the maximum pendulum motion value is extracted every 400s to obtain a total of 25 maximum values for Gumbel fitting. However, it is found that this approach is over-conservative since the template will not maintain at the same critical position for such a long period during the real operation. The second approach is less conservative but more practical. It assumes that the template will remain at the critical position for about 1/3 duration of the whole process. Since the first critical position is close to the end of the 1/3 of the process, using 1/3 of the duration (150s) is considered reasonable. The required tugger lines are continuously engaged at the given template position on deck during the steady-state simulations. The dynamic motions in X and Y are subtracted from their mean values at the given crane tip location to obtain the dynamic oscillations time history.

Figure 4-2 represents the total and subtracted motions in both X and Y for a 1000s duration when the crane tip is set at the end of the over-boarding. The instantaneous dynamic X and Y motions are fitted into Gaussian distribution, and the probability density functions (PDF) are also plotted.

From the standard deviation values of the fitted PDF, the pendulum oscillations in X are almost twice as those in Y. This is because that the crane tugger lines control the motions of the template in Y, while the motions in X are not controlled efficiently.

The equivalent pendulum motions for assessment of the sea states are then obtained following Eq. **(4.1)**. Compared to the motions obtained using the transient approach (Figure 4-1), the responses using the steady-state approach are closer to stationary processes. The unreal dynamic effects from the engagement of the tugger lines are thus avoided using this approach.
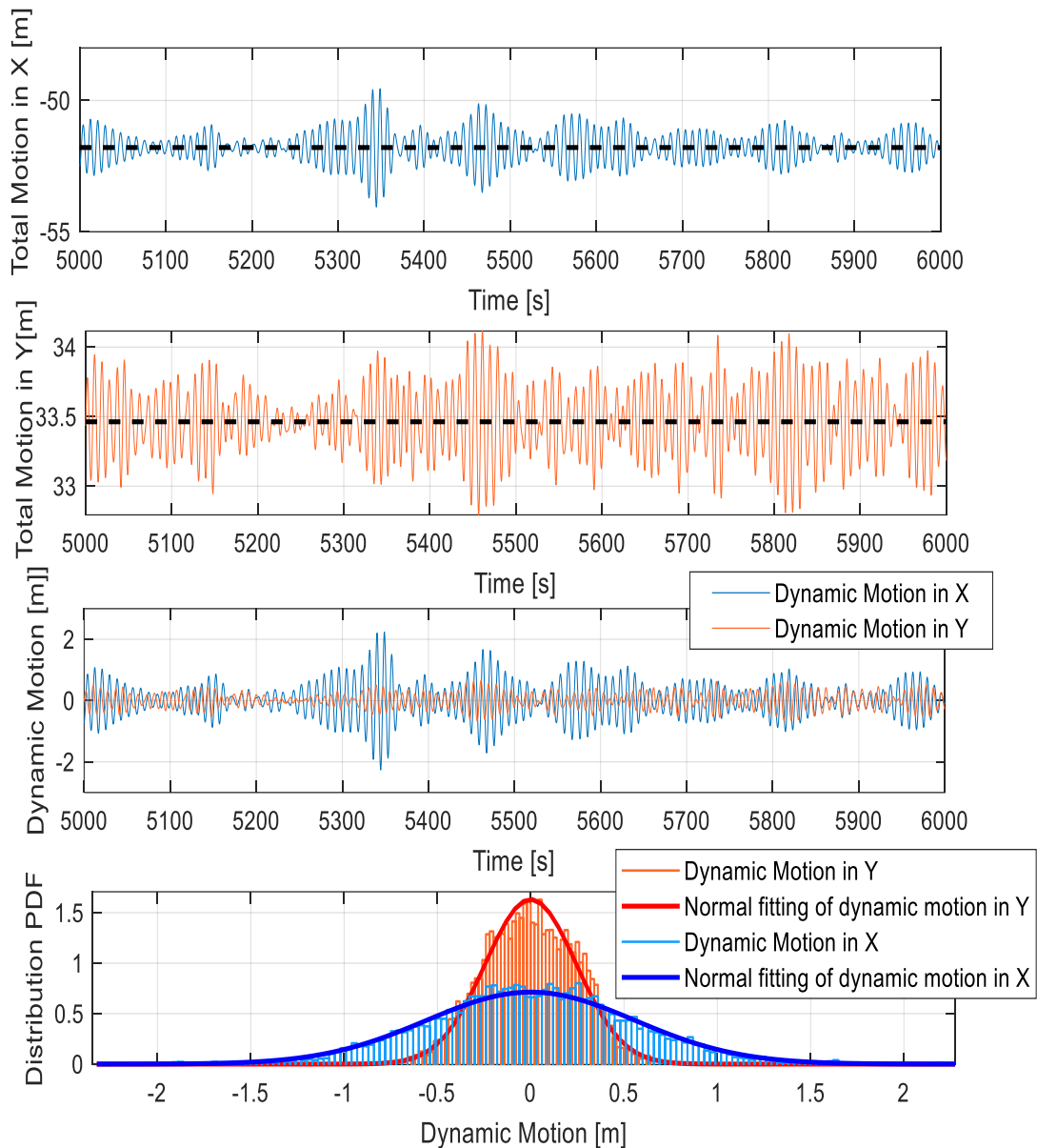
Figure 4-2 Time history of the total and dynamic motions in X and Y using steady-state approach at the end of the over-boarding (Tp = 8s and Hs = 1.2m).

4.3 Lowering to splash-zone operational criteria

As the template suction anchor roof crosses the splash-zone, an intense fluctuation in tension forces for both the main lift wire and slings takes place (see Figure 4-3). This is due to the slamming forces acting on the roof of each anchor as it reaches the free surface. DNVGL-ST-N001 and DNVGL-RP-N103 guidelines are used to set the limiting criteria for the operation based on the experience slamming forces [1, 11]. According to the concerns mentioned in section 1.3.2, the two main limiting criteria for the splash-zone crossing are:

1) Snapping load on the main lifting wire
2) Slacking load on the main lifting wire and each sling

4.3.1 Maximum load criteria

According to DNVGL-ST-N001, the recommended dynamic amplification factor (DAF) for a static hook load (SHL) within a range of 100 to 300 tons is 1.25. Since the operation SHL is around 275 tons, the maximum allowable dynamic hook load (DHL) is set to 345 tons [1].

This DHL value is completely within the vessel's crane operational range. The crane has a DAF value of 1.3 and a maximum static load of 320 tons at the 18m working radius of the operation. As a result, the crane can operate safely till a maximum dynamic load of 416 tons.

4.3.2 Slacking criteria

According to DNVGL-RP-N103, the required minimum margin against slack in slings and hoist line is 10% of the submerged weight. For structures where some elements will be flooded after submergence, the submerged weight should be taken as the minimum static weight when flooding has not yet started [11].

The subsea template has an overall submerged weight of 230 tons, thus with a 10 % margin against slack, the force in the main lift wire should not be less than 23 tons, while for each sling, the force should not be less than 6 tons.

The results from Figure 4-3 demonstrate that most of the extreme dynamic responses occur when the suction anchor roof reaches the splash zone crossing. A similar tension force profile can also be noticed for each of the four slings as shown in Figure 4-4.
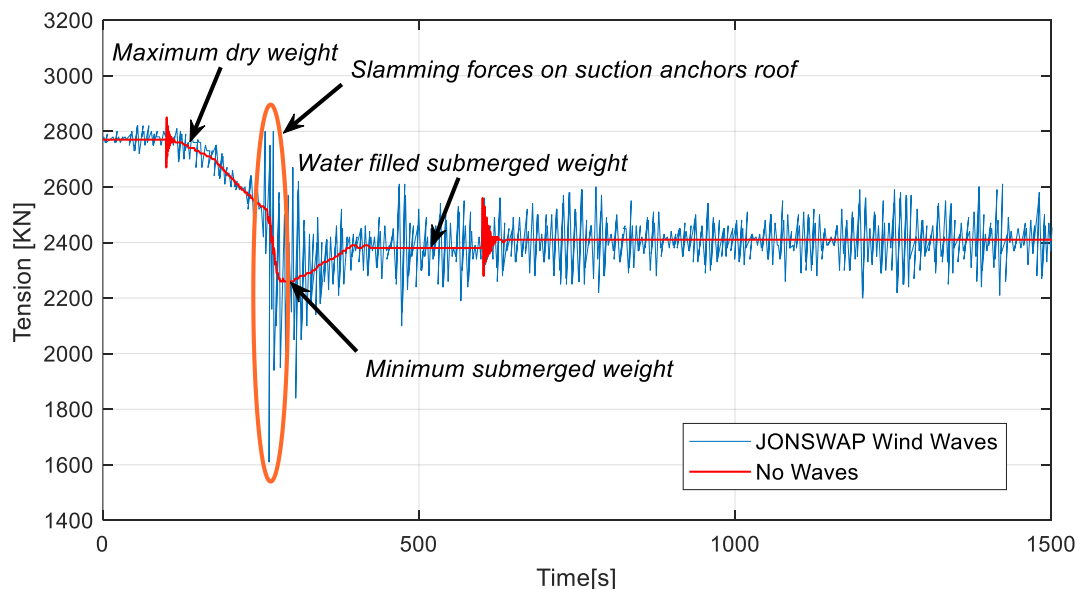

Figure 4-3 Lift Wire Tension at Tp = 10s and Hs = 1.9m.

Figure 4-4 shows that sling 1 and 3 have higher initial tension force while sling 3 and 4 experience more fluctuation at splash zone crossing.
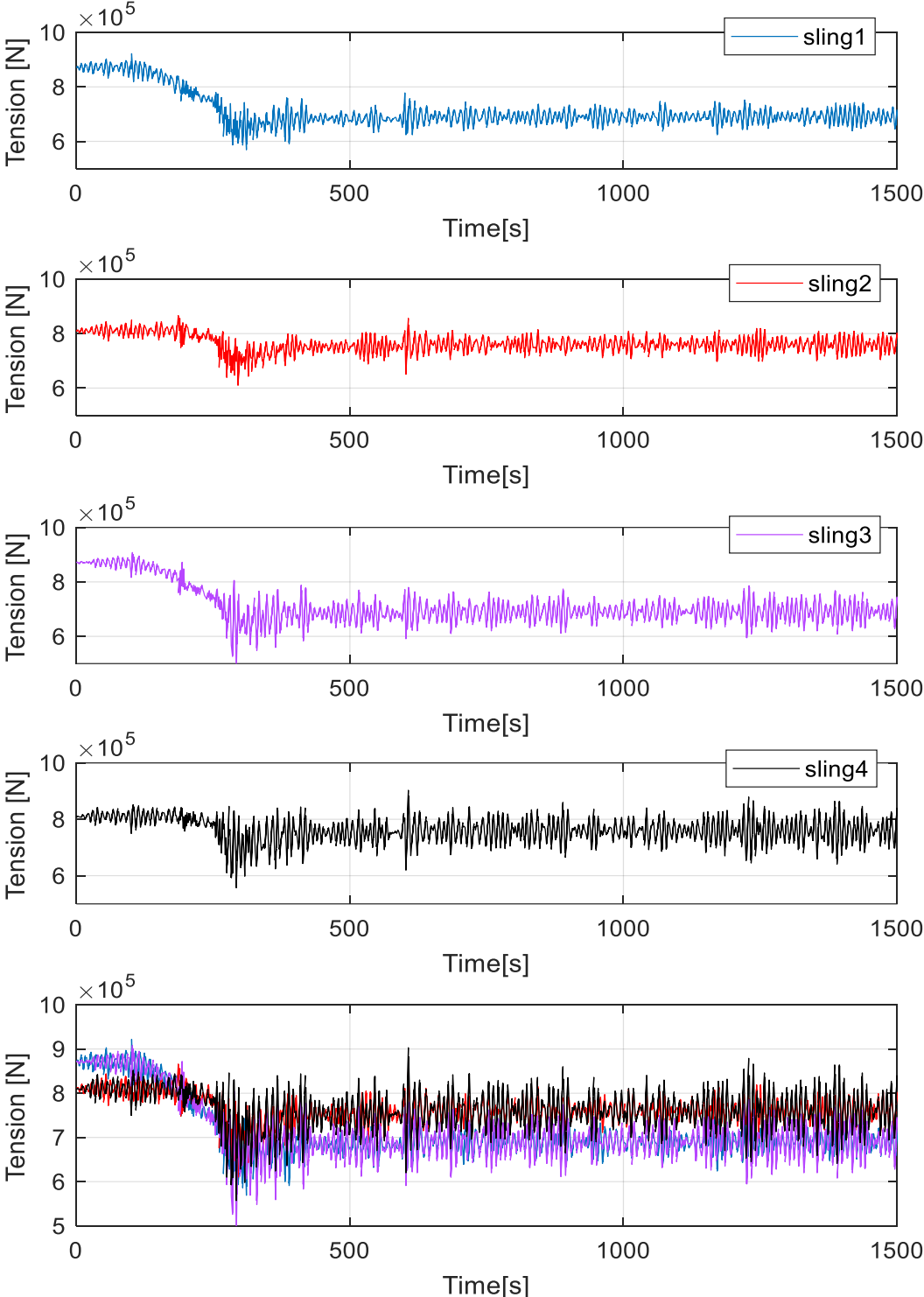

Figure 4-4 Slings Tension at Tp = 10s and Hs = 1.9m.

This due to the tugger lines pulling on sling 1 and 3 side towards the crane base, thus increasing the tension on them. Furthermore, both suction anchor 3 and 4 are facing the wave direction. As a result, the dynamic responses on slings 3 and 4 are higher compared to slings 1 and 2. However, when the template is fully submerged the tugger lines forces start pulling upward, thus decreasing the tension forces on sling 1 and 3 side (See Figure 4-5).
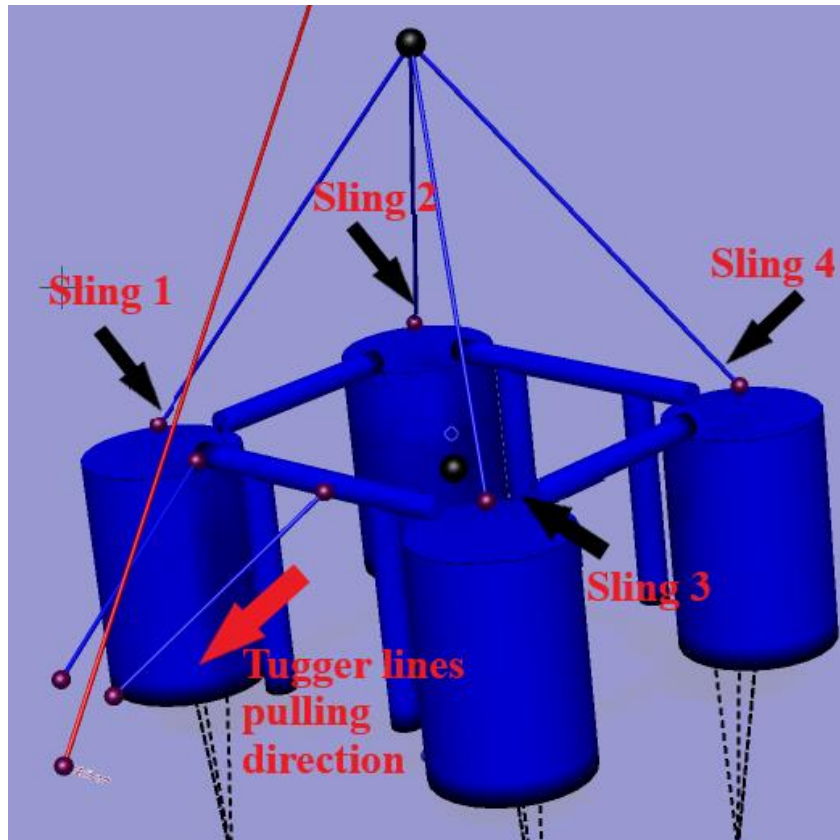
Figure 4-5 Subsea template slings arrangement.

In order to assess the maximum and minimum tension, three evaluation approaches are chosen based on the number of sea realizations (seeds). The increasing number of seeds will allow a proper statistical assessment of the operation extreme responses based on the introduced EVDs in section 2.5

1) Fitting 25 maxima for lift wire tension and 25 minima for lift wire and each sling tension at each given sea state.
2) Fitting 50 maxima for lift wire tension and 50 minima for lift wire and each sling tension at each given sea state.
3) Fitting 100 maxima for lift wire tension and 100 minima for lift wire and each sling tension at each given sea state.

The splash-zone crossing is more critical than the over-boarding due to the higher dynamic responses on the structure. Accordingly, a 0.98 probability of non-exceedance is assigned for the splash-zone statistical model instead of the 0.9 used in the over-boarding. This is to increase the restrictions on the operation allowable sea state.

4.4 Operational criteria of the combined phases

As previously mentioned in section 1.1, lifting operations are usually classified as weather restricted operations. In some offshore operations, sequential activities can be interrupted due to deteriorations in weather conditions. When this happens, the whole operation is placed on hold until the weather condition improves [7].

However, in lifting operations, the sequential activities cannot be interrupted and placed on hold due to the weather and sea state conditions [7]. This means that the over-boarding and the splash-zone crossing activities cannot be interrupted during the installation. Once the template is in the air, the operation does not stop until the template reaches the seabed.

In each phase, the limiting parameters causing the lowest allowable sea state will be governing the execution of the whole lifting operation.

Chapter 5*

Over-boarding Dynamic Responses

5.1   General

In this chapter, the dynamic responses of the over-boarding phase are discussed. The responses are demonstrated for both the transient and steady-state approaches. The obtained allowable sea state from each approach is compared based on the introduced operational criterion in Chapter 4. In each approach, the extreme pendulum motion responses determine the operational limits. The evaluation of extremes is conducted through the introduced statistical models in section 2.5.

5.2   Dynamic responses using the transient approach

Two peak periods, 6s and 12s are chosen to compare the response of the vessel roll motion for the same Hs, see Figure 5-1. From the figure, the induced roll motion at 12s peak period is clearly higher compared to 6s because 12s is closer to the natural period of the vessel roll motion. The mean roll motions for both cases are close to zero due to the use of ballast system. By fitting the instantaneous roll motion into Gaussian distribution, the standard deviations of the vessel role motion are 0.46 and 0.25 deg at 12s and 6s, respectively.

The template equivalent pendulum motions for different wave peak periods are evaluated in Figure 5-2. The result shows high dependency of the motions on the chosen peak period at the same Hs. The pendulum motions for both peak periods are fitted with Rayleigh distribution in Figure 5-2. The shape parameter is 0.44 and the standard deviation is 0.29 m at Tp = 6s. However, as the peak period increases to 12s, the shape parameter and the standard deviation increases significantly to reach 0.71 and 0.45 m, respectively. The pendulum motion tends to be more centered around its mean value for low peak periods at the same Hs.
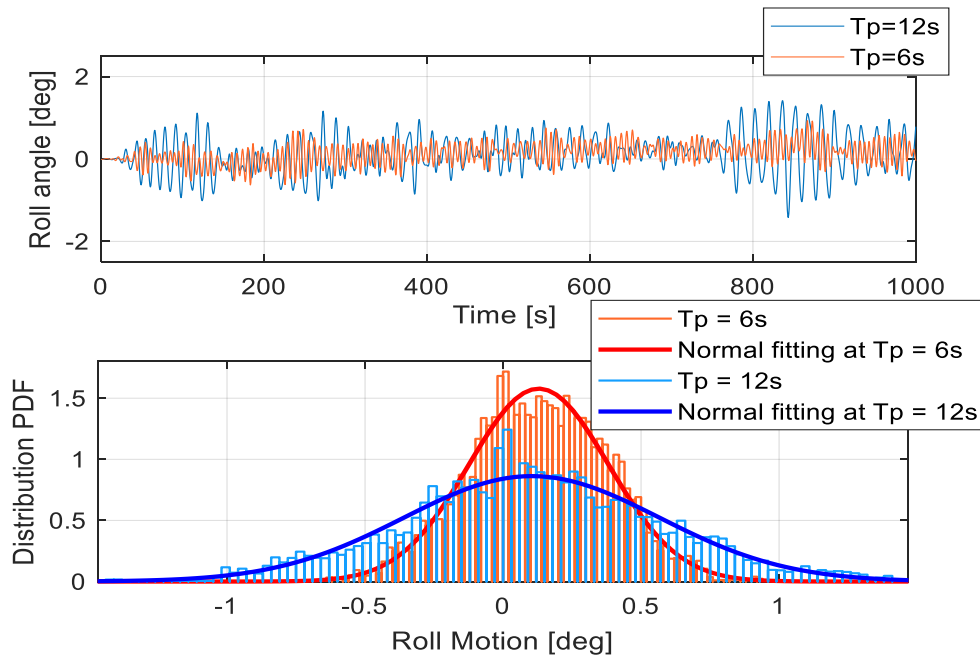
Figure 5-1 Time histories of the vessel roll motion using transient approach for Tp = 12s and 6s (Hs = 1.2m).

Figure 5-2 also shows that high pendulum motions occur close to the end of the 1/3 of the over-boarding (250s) and at the final location of the template during the operation (540s). Similar trends are also observed for various sea states. These two positions are therefore chosen as the critical positions for the steady-state analysis as well as the previously discussed eigenvalues analysis.
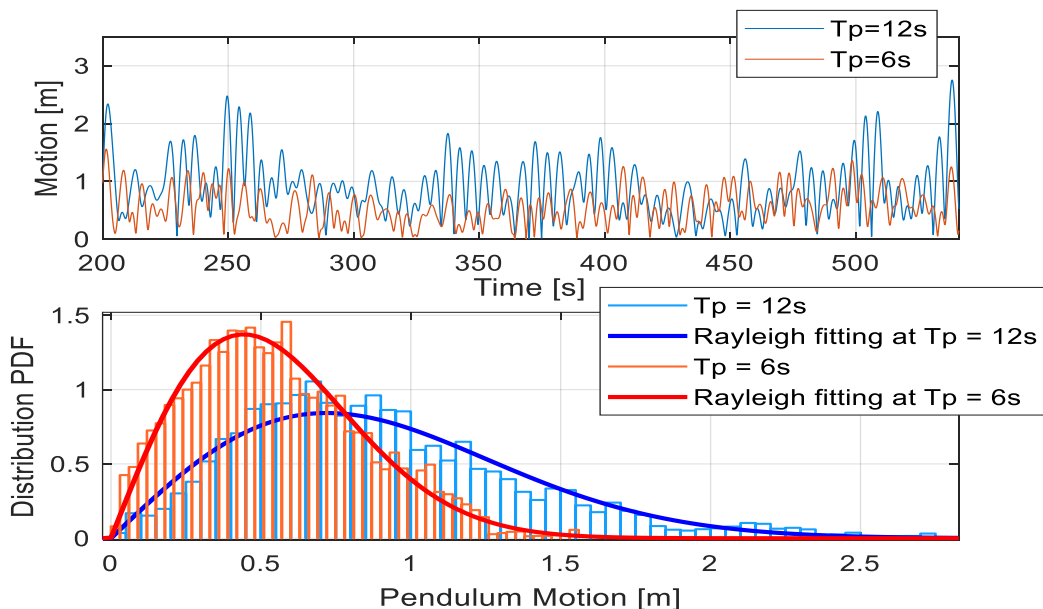
Figure 5-2 Time history of the pendulum motion for Tp = 12s and 6s at (Hs = 1.2m).

Figure 5-3 Deck tugger lines tension force profile at Tp = 8s and Hs = 1.2m using TLA3.

During the transient analysis, the deck tugger lines operate according to the pre-defined sequence in Table 3-20. Figure 5-3 presents the time histories of the tensions in different deck tugger lines during the over-boarding process using TLA3. As mentioned, the buildup and decay phases are added to avoid the sudden change of the tension during engaging and disengaging instants. It can be seen from Figure 5-3 that all tugger lines ope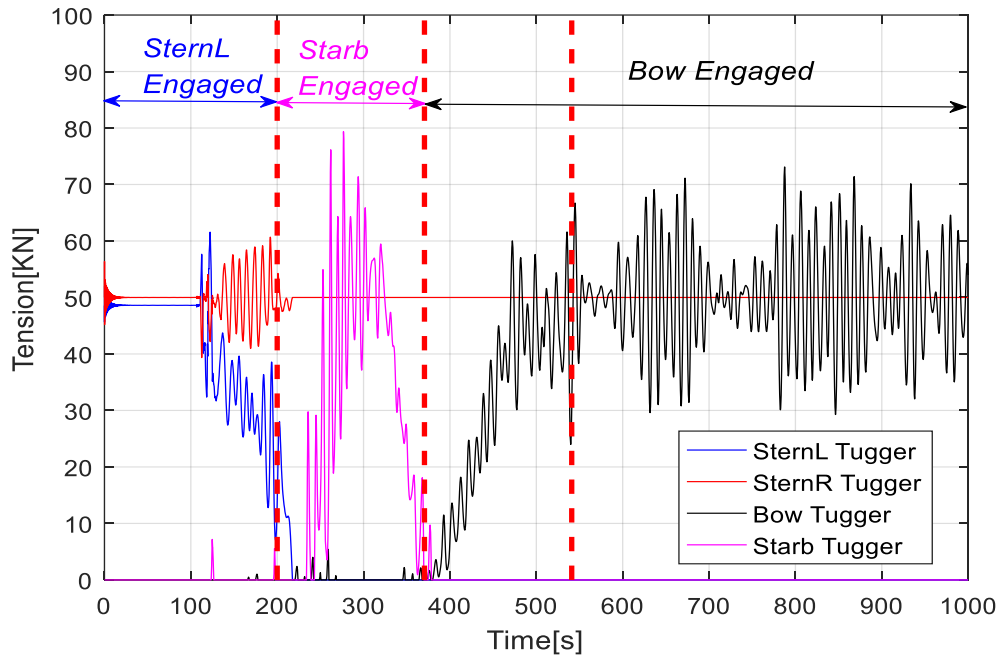rate at the pre-defined phase and the mean tensions are 5 tons. However, larger fluctuations of the tensions are observed. The fluctuations in the tension forces for both Bow and Starb tugger lines are much higher than SternL and SternR. These fluctuations are caused by the increased template motions during the over-boarding process.

5.3   Dynamic responses using the steady-state approach

Figure 5-4 presents the dynamic pendulum motions of the template at the two critical positions using steady-state simulations. The maximum response of the pendulum motions for the given sea state at both positions does not reach the limiting value 3m. The comparison also shows a slightly higher responses when the template is at the end of the over-boarding process. The pendulum motions are fitted into Rayleigh distribution in Figure 5-4, and the fitted distribution agree well with the original simulation data. The uncertainties of the fitting of the pendulum motions (Figure 5-2) reduce greatly in the steady state compared to that in the transient phase, as shown in Figure 5-4. This is because that the system conditions are stable in the steady state without changes in the mean positions and the disturbances from the engagement of different tugger lines.
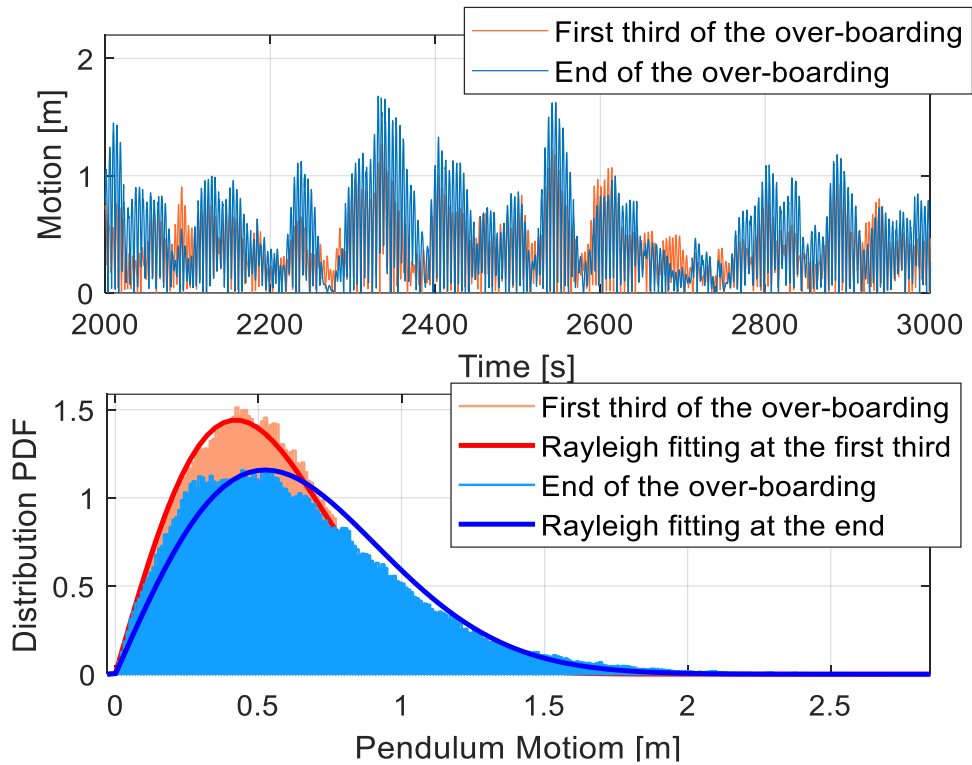
Figure 5-4 Time histories of the pendulum motions using steady-state approach (Tp = 8s, Hs = 1.2m).

The time histories of the tension in the deck tugger lines when the template is located at the end of the over-boarding position are shown in Figure 5-5. Only SternR and Bow tugger lines are continuously engaged at this position. The instantaneous tension forces are fitted into Gaussian distribution. The fittings show that the distributions of the tension at the two locations are similar, the evenly distributed forces over the two tugger lines help to keep the template stable before being deployed through the sea surface.
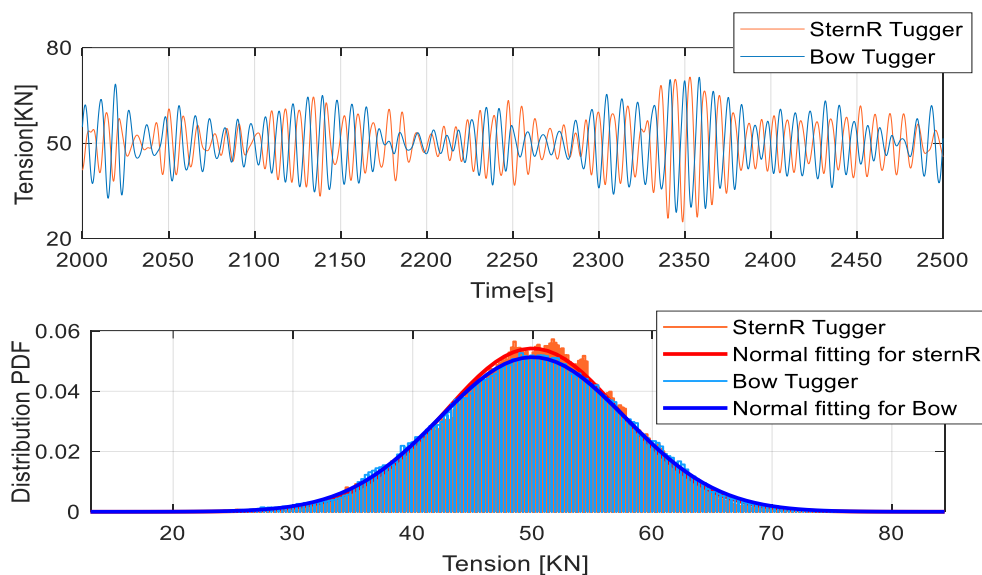
Figure 5-5 Time history of the tensions in the deck tugger lines with TLA3 using steady-state approach (Tp = 8s, Hs = 1.2m).

5.4 Allowable sea states based on the transient approach

The extreme values of the pendulum motions from different wave seeds are fitted into Gumbel distribution to compare with the operational criterion. Figure 5-6 shows an example of a fitted extreme values of pendulum motion into a Gumbel distribution probability paper. Although uncertainties do exist in the tails, the fitting shows that the sample in general follow the Gumbel distribution well.

For the presented condition, the extreme pendulum motion corresponds to the non-exceedance probability of 0.9 is around 2.80m. By evaluating the extreme values for different sea states and comparing with the limiting criterion, the allowable sea states can be found.

Table 5-1 presents the allowable sea states using different tugger line arrangements (TLA) as discussed in the modelling section. The operational limits are significantly low at the higher peak periods compared to 6s peak period. These results are consistent with the eigenvalues of the coupled system in the static analysis.

The static modeling and the dynamic responses of the template and the vessel showed that the 6s peak period will most likely has less induced pendulum motion, as most of the critical natural periods are around 8s. However, adding the deck winches with an increased tugger line tension helped to achieve higher allowable sea states for the operation.

The improvement is more obvious in the sea states with 6s peak period, while the higher peak periods show slightly less improvement. Despite the small differences, it is concluded that TLA3, i.e., crane and deck tugger lines with 5 tons tension, provide the highest sea states compared to other tugger line arrangement.

It should be noted that all the dynamic responses in this study are based on numerical simulations which applies linear wave theory for waves. The allowable Hs values at 6s presented in Table 5-1 exceed the application range for linear wave theory. In addition, the Hs values with Tp of 6s are normally lower than 4m in the real sea. Thus, the results indicate the operations can be operated at any Hs when Tp is 6s.

Table 5-1 Allowable Hs values for different TLA using transient time-domain approach.

Tp [s]	TLA1 [m]	TLA2 [m]	TLA3 [m]
6	4.5	4.9	5.5
8	1.3	1.3	1.4
10	1.1	1.2	1.3
12	1.2	1.3	1.6
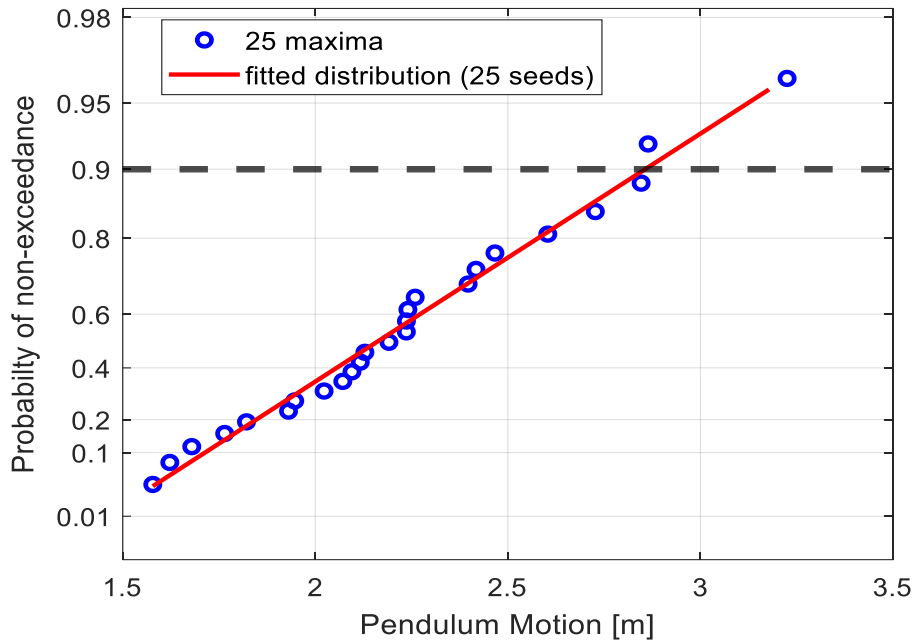
a) Transient Approach
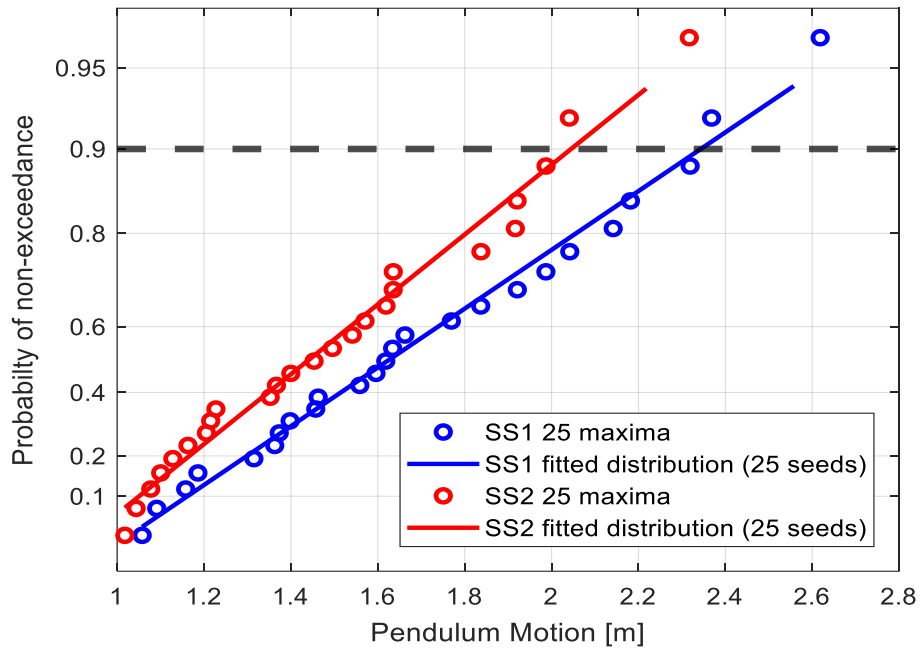
b) Steady State Approach

Figure 5-6 Fitting the extreme values of the pendulum motion into Gumbel probability paper using 25 seeds (TLA3, Tp = 8s and Hs = 1.2 m).

5.5 Allowable sea states based on the steady-state approach

In the steady-state approach, the maximum pendulum motion values are extracted using both SS1 and SS2 corresponding to a simulation duration of 400s and 150s, respectively for each wave seed. A total of 25 maximum values are fitted into Gumbel probability paper with the same method followed in transient time-domain simulation.

Figure 5-6b present the fittings of the extreme values under the same sea state using the two steady-steady approaches. Compared to Figure 5-6a , the uncertainties of the Gumbel fitting seem to be reduced when using the SS1 steady-state methods.

For the same non-exceedance probability of 0.9, the extreme pendulum motions decrease significantly from 2.80m using transient method to 2.35m using SS1 and 2.07m using SS2. This is because the motions using the transient methods are over-estimated due to the influence of changing tugger lines in the whole process. Moreover, using SS2 provides lower extreme values due to the shorter simulation time compared to SS1. By evaluating various Hs values for the target Tp, the allowable sea states are determined based on the results at the most critical suction anchor position.

Table 5-2 and Table 5-3 show the allowable sea states using SS1 and SS2 approaches for three TLAs. It is obvious that the sea states have been improved significantly for longer Tp using the steady-state approach than the transient approach. When the simulation time for each seed is 150s (SS2) instead of 400s (SS1), the sea states increase again. This provides more realistic sea states and the allowable Hs values can reach over 2m with Tp of 12s.

Table 5-2 Allowable Hs values for different TLA using steady-state SS1 approach (400s for each seed).

Tp [s]	TLA1 [m]	TLA2 [m]	TLA3 [m]
6	5.6	6.1	6.3
8	1.3	1.5	1.6
10	1.3	1.5	1.6
12	1.7	1.9	2

Table 5-3 Allowable Hs values for different TLA using steady-state SS2 approach (150s for each seed).

Tp [s]	TLA1 [m]	TLA2 [m]	TLA3 [m]
6	5.9	6.4	6.6
8	1.5	1.6	1.8
10	1.5	1.7	1.8
12	1.8	2	2.2

Similarly, as observed from the transient approach, tugger lines arrangement TLA3 leads to the highest sea states. This again proves the importance of deck handling operations during the over-boarding operation.

For a better comparison, the sea states from the different approaches using tugger line arrangement TLA3 are summarized in Figure 5-7. As mentioned earlier, because the sea states are unrealistically high at 6s, they are not included in the figure.

The comparison shows clearly that different approaches applied in the time-domain simulation influence the sea states greatly. The results from this figure can be used further together with the sea states obtained for the splash zone crossing phase in order to plan for the whole deployment operation of the template.
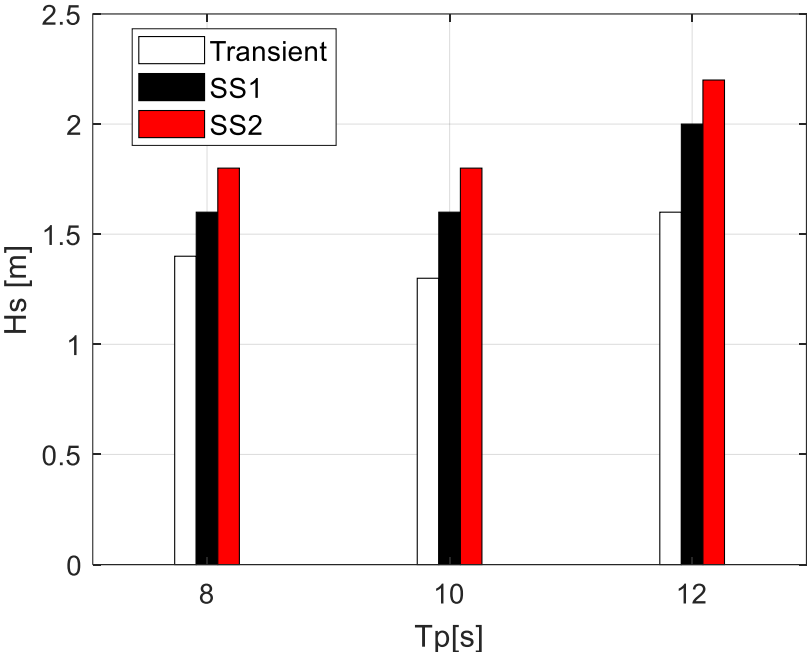

Figure 5-7 Allowable sea states using different time-domain approaches with tugger line arrangement TLA3.

Chapter 6

Splash-zone Dynamic Responses

6.1   General

In this chapter, the dynamic responses of the splash-zone crossing phase are discussed. The responses are demonstrated for both shielding and non-shielding models. The obtained allowable sea state from each model is compared based on the introduced operational criterion in Chapter 4. In each model, the extreme responses of the lift wire and slings tension determine the operational limits. The evaluation of extremes is conducted through the introduced statistical models in section 2.5. The chapter will also address the limitations of modeling the shielding effect in SIMO.

Several sensitivity studies are discussed in the chapter. These studies demonstrate the influence of changing specific modeling parameters on the dynamic responses. The simulation results are also compared with the actual crane logging data for the same installation vessel. This comparison is to validate the accuracy of the introduced modeling methodology in this study.

6.2   Splash-zone crossing with and without shielding effect

The wave kinematic RAO in disturbed waves region due to the vessel obstruction is calculated in WADAM program. The results is obtained by applying the potential wave theory (section 2.2.2) to solve the fluid domain near the vessel [6]. The contour plot in Figure 6-1 illustrates the RAOs of the disturbed wave elevation near the installation vessel used in the model. The subsea template initial position is highlighted with red dots in the XY coordinate system.

At 12s peak period, the elevations of the disturbed waves are close to the incident wave with RAO value close to 1. However, at 6s peak period, the elevations are considerably reduced due to the shielding effect provided by the vessel. It is also noticed that vessel shielding effect is stronger when the coordinates moves further towards the vessel stern for low peak periods. At 6s and 8s peak period, the wave elevations RAO is close to 0.5 near suction anchors 1 and 2, while near anchors 3 and 4, the RAO is close to 0.7. This align with the results shown in Figure 4-4. The figure showed that the slings tension force fluctuation is higher for slings 3 and 4.
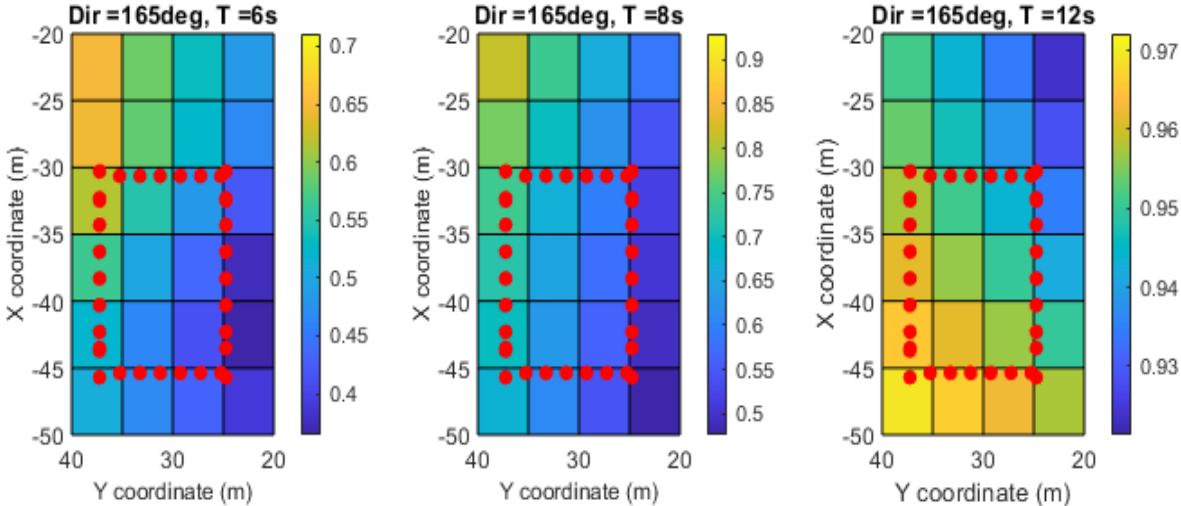

Figure 6-1 RAOs of wave elevation in XY coordinates near the vessel at the template initial position and a wave direction of 165 deg.

It is possible to include the effect of the vessel shielding for the analysis in SIMO with the structure in stationary positions. The installation vessel acts as a breakwater obstruct against the wave spreading as previously mentioned in section 2.2.4. The diffraction of waves will have significant influence on the template splash-zone crossing analysis.

However, when the winch is running, and the subsea template is changing its vertical position in water, the effect of shielding is not accurate. This is due to the absence of the exponential decay of the wave kinematic with the increasing depth according to the potential wave theory (Section 2.2.2). This absence will affect the wave kinematic which in turn will influence the slamming force calculation. From Eq. **(2.13)**, the total hydrodynamic forces from Morison's equation are function of the flow velocity and acceleration.

However, simulations with shielding effect can still provide proper estimation for the hydrodynamic responses just below the free water surface when the suction anchor roof reach the splash-zone without being deeply submerged. HydroD-WADAM results for wave elevation/pressure and velocity must be available for a specified point where the template anchors are located both in horizontal and vertical direction. Then the endpoints of each slender element on the numerical model must be connected to these points.

As previously mentioned, the largest dynamic forces in the lifting wire and slings were observed when the top of the suction anchors were close to the free surface (section 4.3). Therefore, a

HydroD-WADAM calculation are performed to obtain diffracted wave data at the endpoints of the submerged slender elements which are assigned for the template in this vertical lowering position. The slender element model of the subsea template with the corresponding points of the diffracted wave data is shown in Figure 6-2.

To evaluate the effect of shielding, a short part of the numerical simulation is performed where the subsea template is moved from a position with the top of the suction anchors above the free surface to just below.
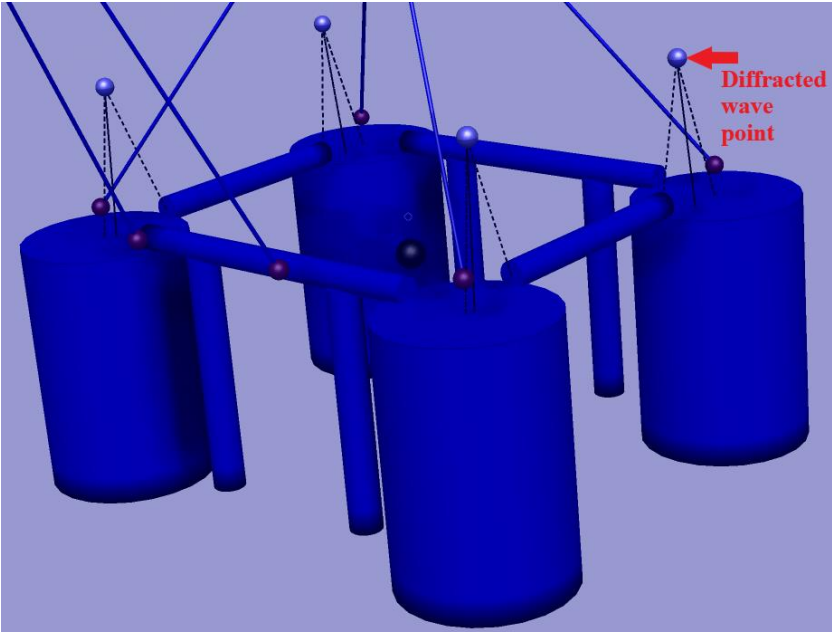

Figure 6-2 Diffracted waves points in SIMO splash-zone model.

6.2.1   Dynamic responses without shielding effect

The different tension force time histories showed that the lift wire maximum limit is more critical for the operation than the slack limit. They also show that the critical dynamic responses on the lift wire exceed the slings. This can be seen clearly from Figure 6-4. The figure compares the tension force time history for the main lift wire and slings from five different seeds. In each seed, none of the slings reach the minimum defined slack limit for the operation.

It is also noticed that the splash zone crossing dynamic responses can be extremely high at different sea realizations for the same sea state. This is due to the randomly generated wave phase angle at each seed. Figure 6-3 provides a better comparison for the splash zone crossing dynamic responses on the lift wire between two different sea realization having the same peak period Tp and significant wave height Hs. Seed 29 clearly exceeds seed 48 in terms of maximum and minimum tension on the lift wire.
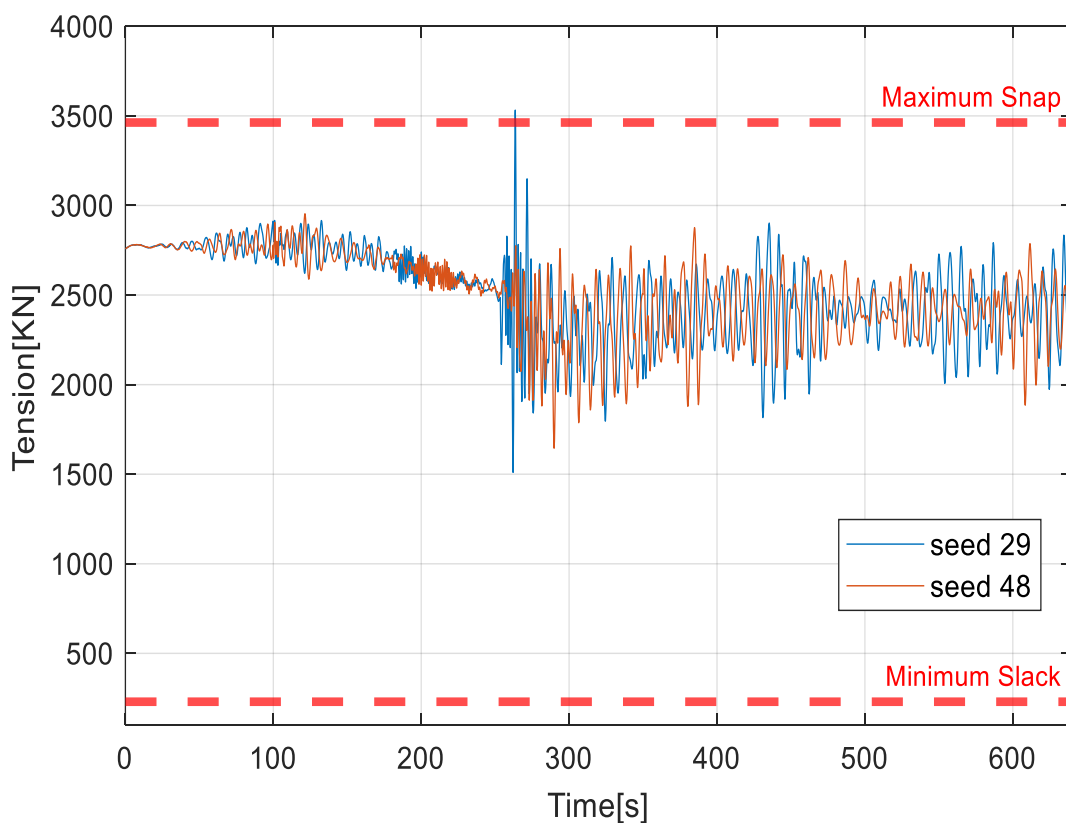
Figure 6-3 Lift wire tension at Tp = 8s and Hs = 2m for two different sea realizations.

The EVDs are used in order to develop a proper statistical model for extreme responses. In similar splash-zone numerical studies, Gumbel distribution usually provides proper fitting for the extremes [6]. However, in this study, the statistical evaluation of the maximum lift wire tension shows improper fitting when utilizing Gumbel statistical model.

Figure 6-4 Comparing lift wire and slings tension at Tp = 8s and Hs = 2m for five different sea realizations.

Similar behavior is also noticed when the 2 parameters Weibull distribution is used in the fitting. Both Gumbel and Weibull are commonly used distributions for fitting extreme values, and usually, a proper fitting for the maxima can be obtained.

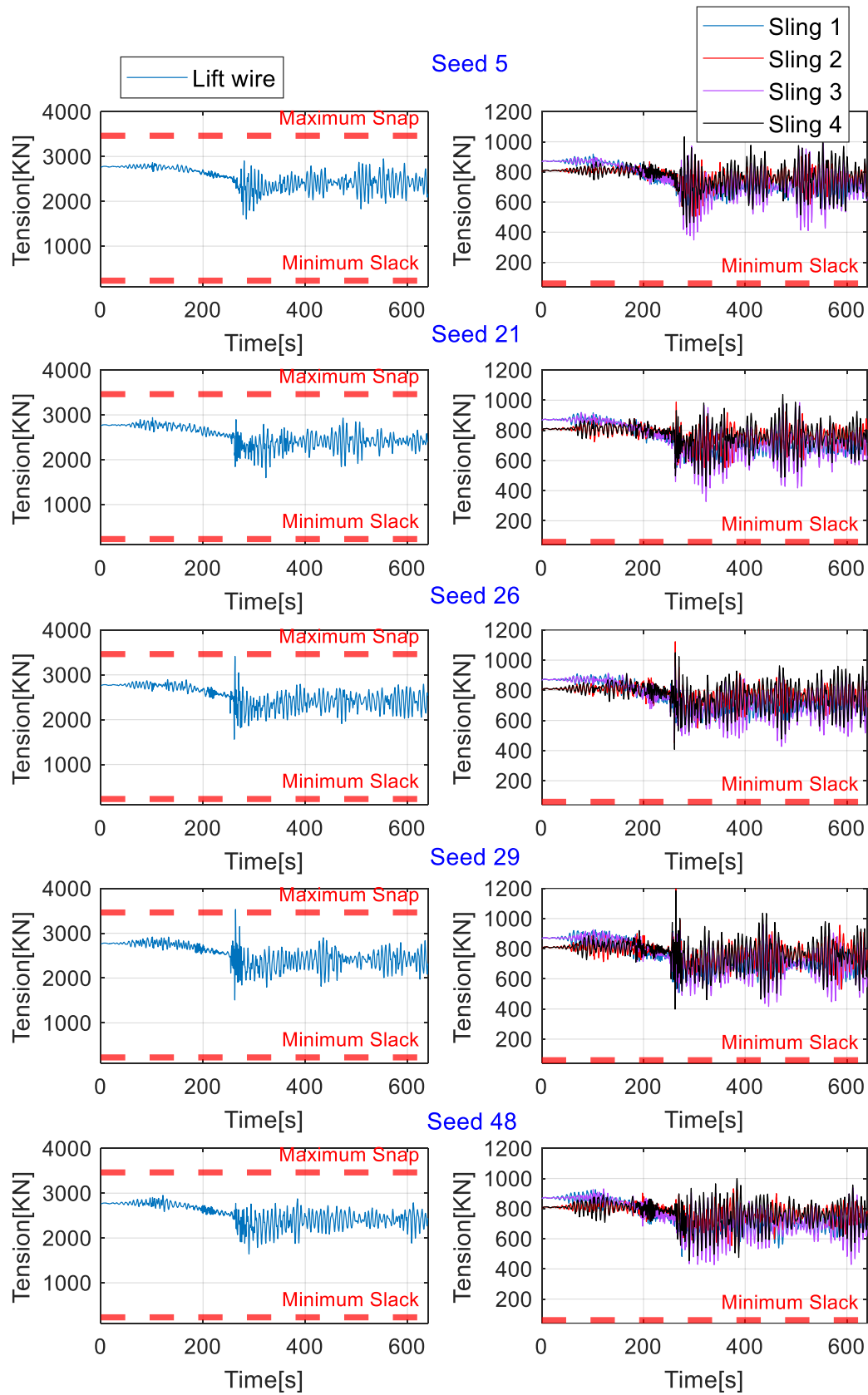The most proper fitting is found when the Generalized Extreme Value (GEV) distribution is used for the model. Figure 6-5 compares the fitted PDF of 100 lift wire tension maxima using Gumbel, Weibull, and GEV distributions. The maxima are obtained at the same sea state from 100 different realizations.

Although the fitting shows uncertainties near the tail of the distribution, the maxima still follow the GEV distribution in general. The GEV provides a proper statistical model for the limiting criteria when 0.98 probability of non-exceedance is being used with a sufficient amount of data.

The probability plots are also compared for the 3 distributions in Figure 6-6 with the same sample of data. The lower part of the figure shows that Gumbel and Weibull probability plots are completely off fitting at both tails of the distribution.

The top plot for GEV on the other hand shows an extremely well-fitting for the majority of the data and the scattering range is narrower at the tail end compared to Gumbel and Weibull.
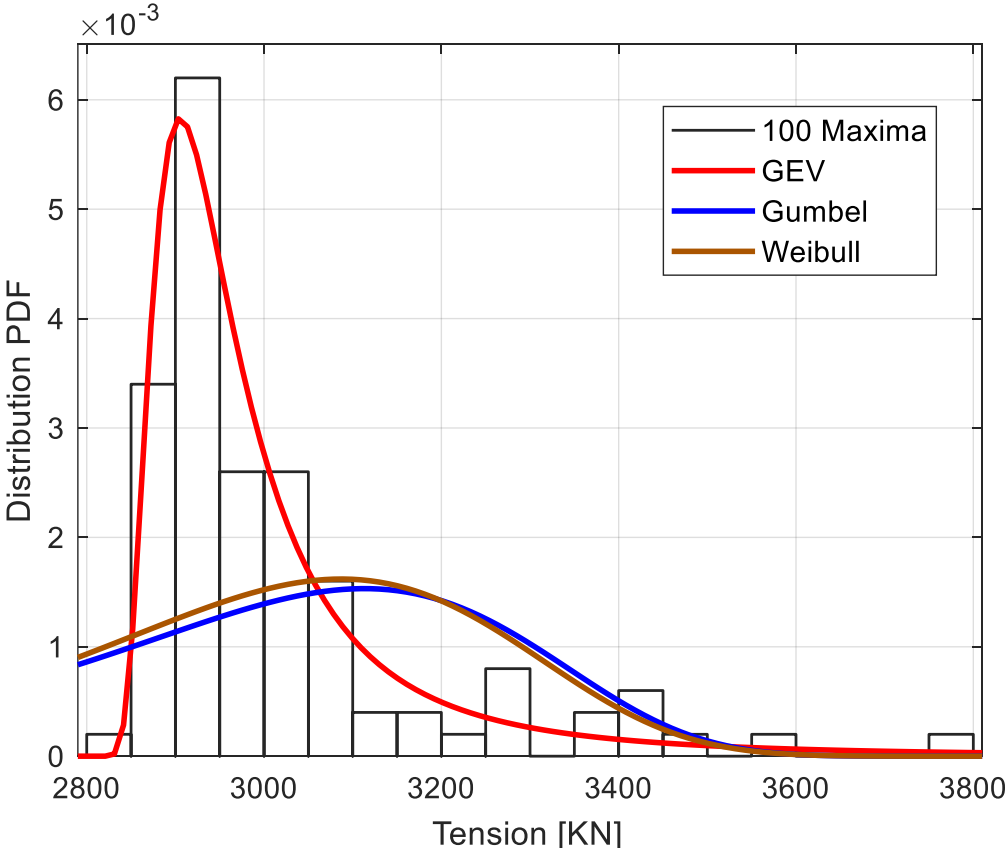
Figure 6-5 PDF fitting for lift wire 100 maxima at Tp = 8s, Hs = 1.8m with different EVDs.
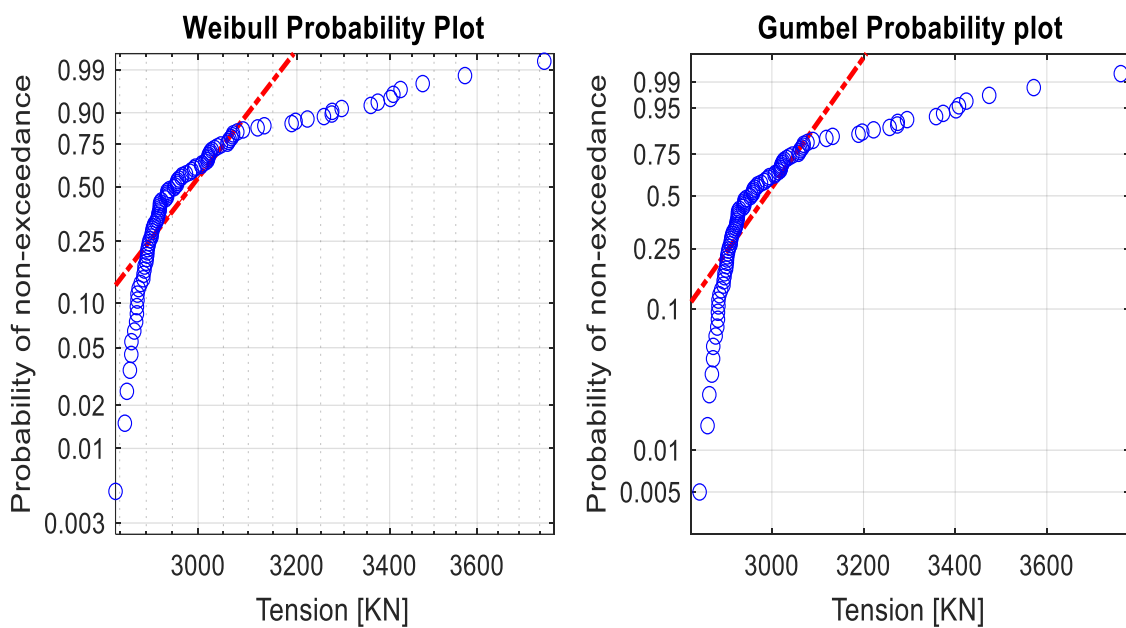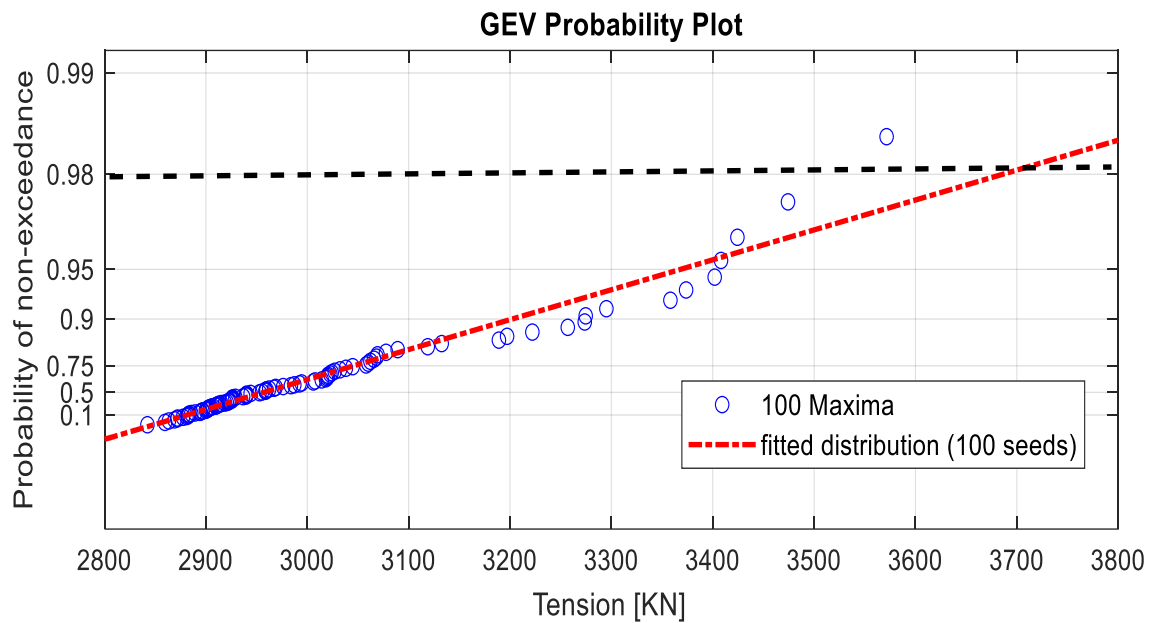
Figure 6-6 Probability plot fitting for lift wire 100 maxima at Tp = 8s, Hs = 1.8m with different EVDs.

The lift wire minimum tension is also evaluated with the 3 EVDs using the obtained 100 minima from the same sea state realizations. Unlike the maxima PDF, Figure 6-7 shows that the minima generally follow both Gumbel and Weibull. The fitting at the high density of the distribution is better than GEV fitting. The figure also shows a slightly better fitting at the distribution tail when Gumbel fitting is utilized. As a result, Gumbel distribution is chosen as a proper statistical model for the lift wire minima.
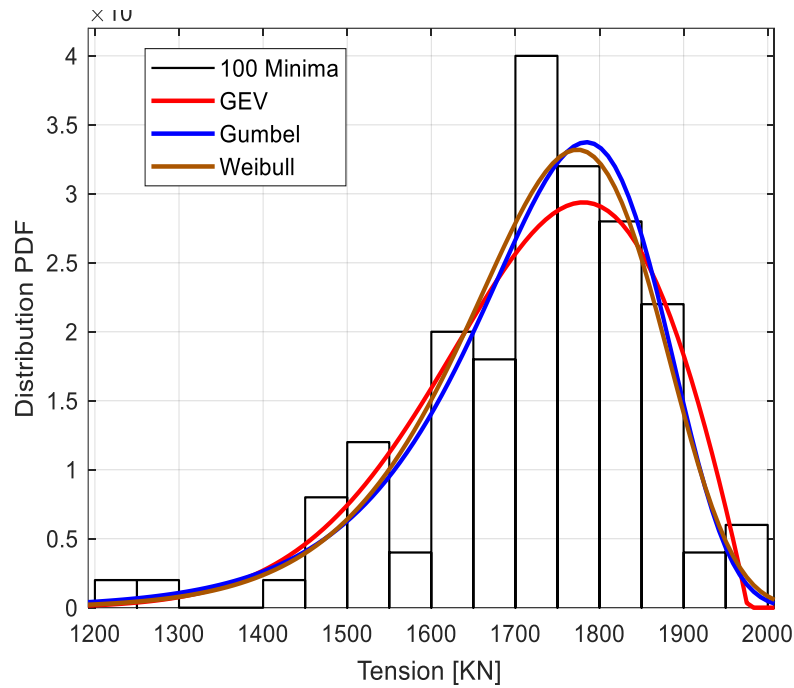
Figure 6-7 PDF fitting for lift wire 100 minima at Tp = 8s, Hs = 1.8m with different EVDs.

It is noticed that a minimum of 75 seeds is required in order to achieve the assigned 0.98 target probability of non-exceedance for the maximum lift wire tension. The lower number of seeds did not achieve the target probability when GEV distribution is utilized (see Figure 6-9). It is also noticed that the scattering range of the data near the tail gets narrower when the sample size is increased from 25 to 100. On the other hand, 50 seeds were sufficient to achieve the same target probability for the lift wire minima when Gumbel distribution is utilized (see Figure 6-8). This outcome is mainly due to the higher uncertainties near the tail of the GEV distribution fitting for the maxima in comparison to the Gumbel distribution fitting for the minima.
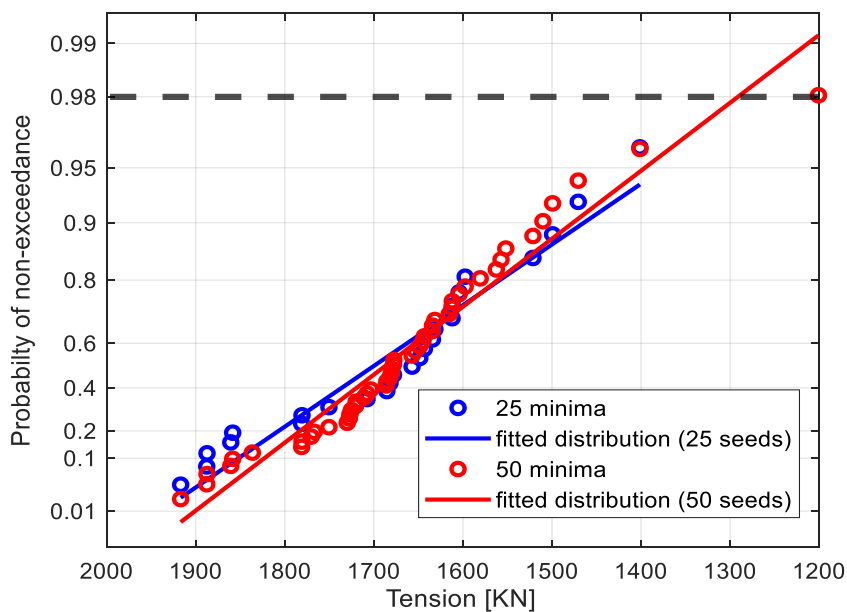
Figure 6-8 Lift wire minima Gumbel fitting at Tp = 8s and Hs = 2m.

Figure 6-9 Lift wire maxima GEV fitting at Tp = 8s and Hs = 2m.

6.2.2   Dynamic responses with shielding effect

The shielding effect shows an overall decline in the magnitude of the slamming force acting on the suction anchors roof. Figure 6-10 compares the lift wire tension time history with and without shielding effect for the same sea state. It is noticed that when the shielding effect is included the dynamic forces are reduced considerably when the suction anchor reaches the splash-zone.
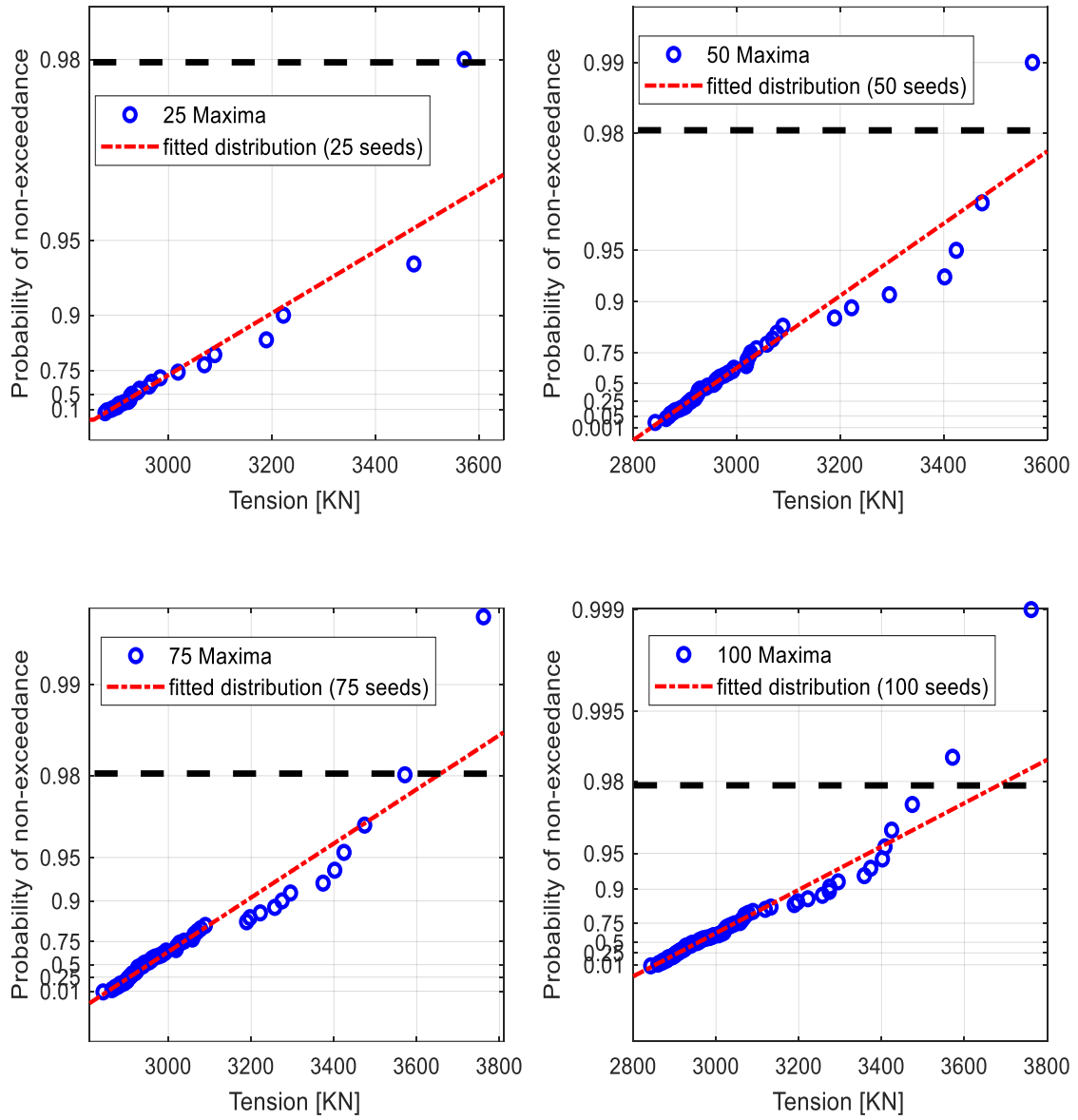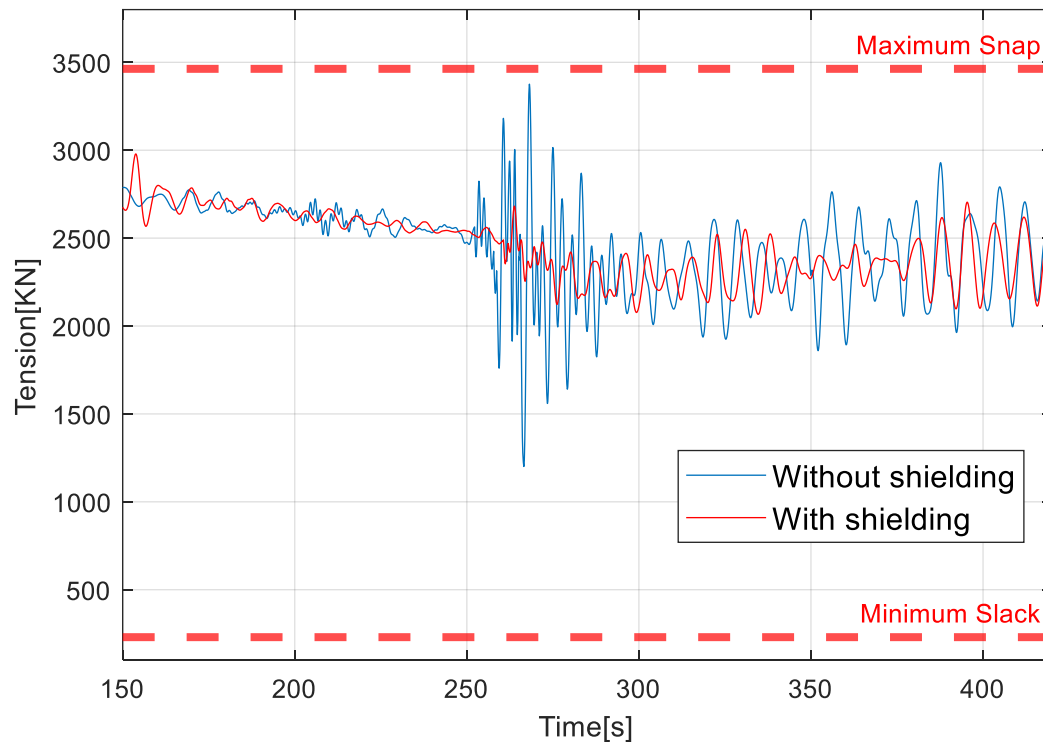

Figure 6-10 Lift wire tension at Tp = 6s and Hs = 2.5m with and without shielding.

The PDF fitting of the maxima for both shielding and non-shielding models at 6s peak period in Figure 6-11 shows a higher deviation in tension force range from its mean value when the shielding effect is not utilized. It also shows that the tension force is more centered around a lower mean value with almost twice the density when the shielding effect is active.

The considerable drop in the maxima is more noticed at short waves with lower peak periods. At higher peak periods, the PDFs in Figure 6-12 and Figure 6-13 shows less influence from shielding on the maxima. Moreover, when the 12s peak period is reached, the two PDFs at 12s peak period in Figure 6-14 start to become more identical and the influence of the shielding effect provided by the vessel decays significantly.

However, the shielding effect still shows an overall increase in all the allowable sea states across all peak periods. The standard deviations for the introduced PDFs across the different peak periods are also compared with and without the shielding effect in Table 6-1. The same 165 deg wave direction is kept in all the PDFs comparison.
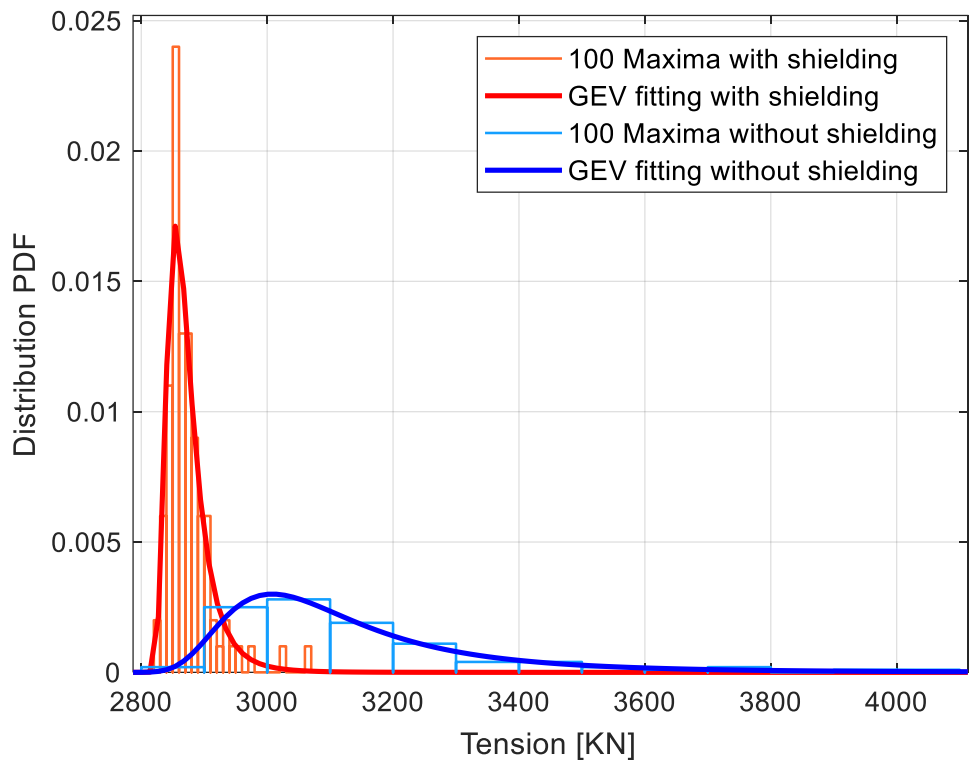
Figure 6-11 PDF fitting with GEV at Tp = 6s and Hs = 2.5m with and without shielding.

Figure 6-12 PDF fitting with GEV at Tp = 8s and Hs = 2m with and without shielding.
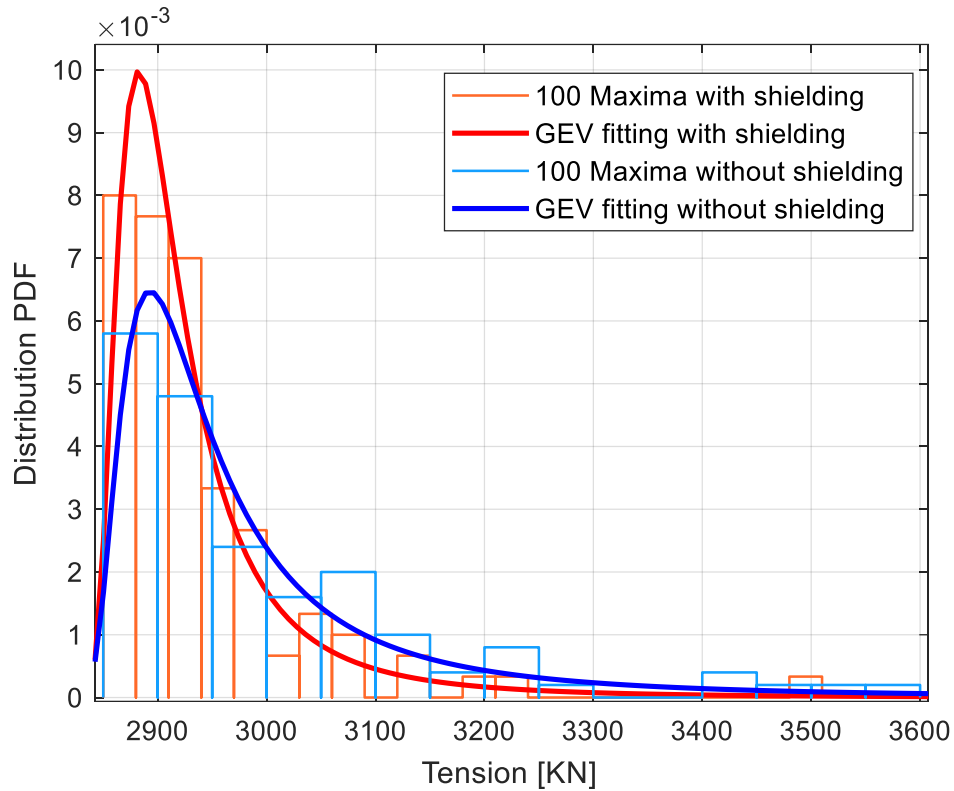
Figure 6-13 PDF fitting with GEV at Tp = 10s and Hs = 2m with and without shielding.
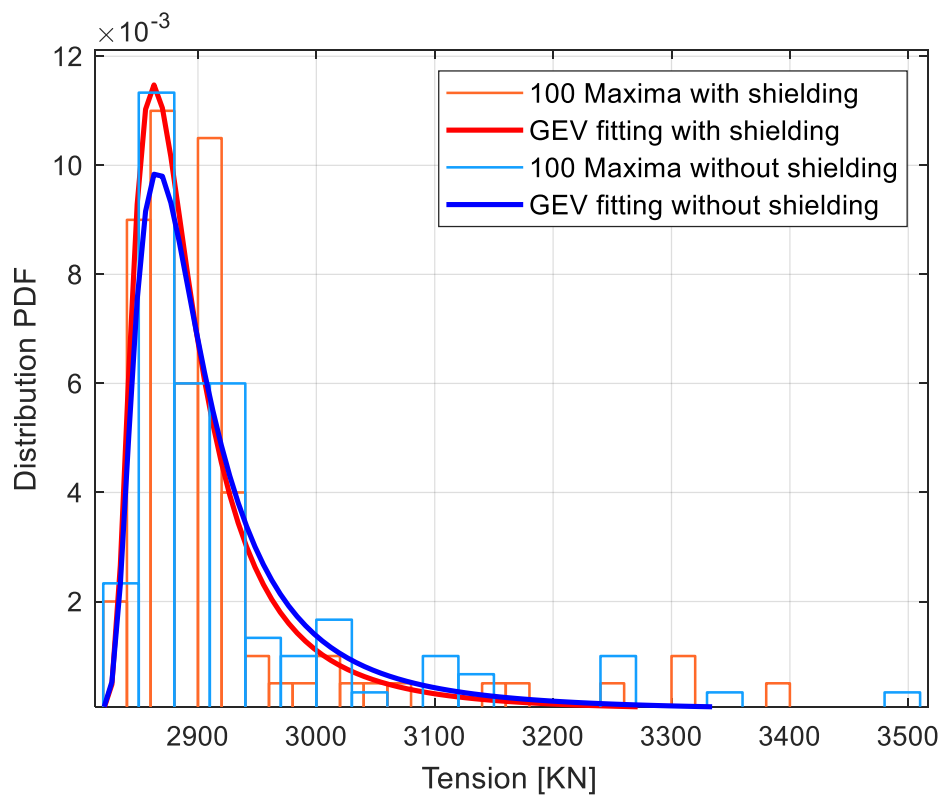
Figure 6-14 PDF fitting with GEV at Tp = 12s and Hs = 2m with and without shielding.

Table 6-1 Lift wire maxima standard deviation with and without shielding effect.

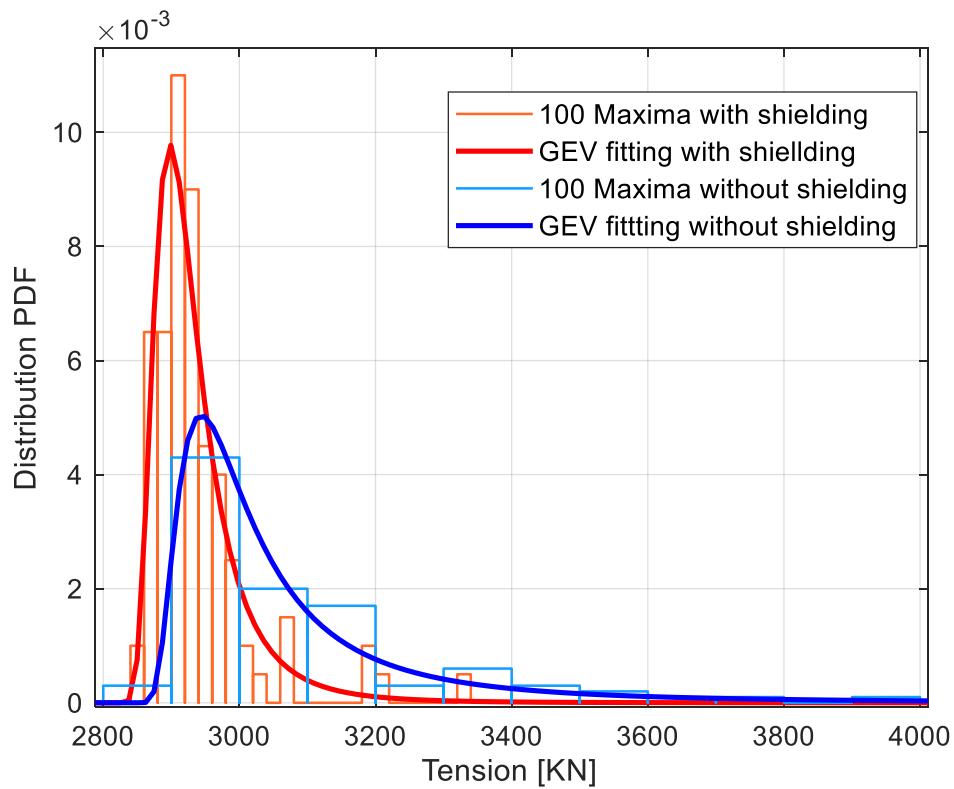| Tp [s]	Hs [m]	Std.Dv with shielding [KN]	Std.Dv without shielding [KN]
6	2.5	37.12	216.88
8	2	76.33	194.12
10	2	91.09	150.26
12	2	100.2	113.19

Table 6-1 shows a significant drop in the standard deviation of the 100 maxima for both 6s and 8s peak periods when the shielding effect is utilized. However, this drop starts to be less when the 10s peak period is reached. Furthermore, the influence of the vessel shielding starts to decay when the 12s peak period is reached with less than 15 KN drop in standard deviation value. When shielding is applied, the low deviation in the GEV fitting for 6s and 8s peak periods makes it possible to achieve the assigned 0.98 target probability of non-exceedance with only 50 maxima as shown in Figure 6-15. Such outcome was not possible without the shielding effect due to the high deviation of the extreme responses near the tail of the fitting (see Figure 6-9).
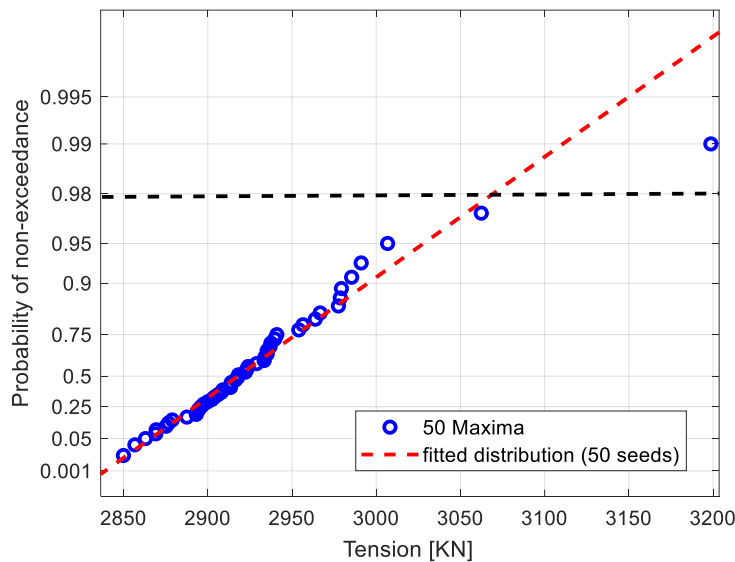
Figure 6-15 Lift wire maxima GEV fitting at Tp = 8s and Hs = 2m with shielding.

Table 6-2 shows the obtained allowable sea states for splash zone crossing with and without shielding effect based on the GEV statistical model.

Table 6-2 Allowable Hs value for splash-zone crossing with and without shielding.

Tp [s]	Hs with shielding [m]	Hs without shielding [m]
6	4.2	2.1
8	2.8	1.7
10	2.5	1.8
12	2.4	2.3

Same as the over-boarding, the allowable Hs values at 6s with shielding presented in Table 6-2 exceed the application range for linear wave theory. Thus, the results indicate the operations can be conducted with shielding at any Hs when Tp is 6s. The 12s has the lowest limiting Hs among all the evaluated peak periods. It is also the least influenced by the vessel shielding effect (see Figure 6-14).

6.3 Sensitivity studies on splash-zone crossing dynamic responses

6.3.1 Influence of changing wave direction with shielding effect

The RAO of the vessel is significantly influenced by the wave direction. The vessel is always deployed with the bow facing the apparent wave direction during the operation. When the bow is facing the waves, the vessel RAO is significantly low, especially for the heave and roll motions.

According to Eq. **(2.28)**, these two motions, including the pitch, control the crane tip responses as the operation takes place. The results of the installation vessel RAO was obtained from a numerical study performed by Parra, C.A [35]. The RAO of the vessel across different wave periods is shown in Figure 6-17.

From Figure 6-17, the amplitude of both roll and heave motion is significantly low when the wave direction is 180° or 0° at low peak periods. Although the pitch motion shows an opposite behavior, the distance between the vessel CoG and the crane tip on the pitch axis is shorter than the roll axis. Thus, the roll motion will have more influence on the crane tip. This indicates that the vessel will be more stable for the operation when facing the waves from the bow or stern sides.

The installation vessel provides a shielding effect for wave direction between 0° and 180°. This shielding range is shown in Figure 6-16. In order to further investigate the effect of the vessel RAO on the splash-zone dynamic responses at different wave directions, 100 seeds are generated for four wave directions within a range from 25° to 165°.
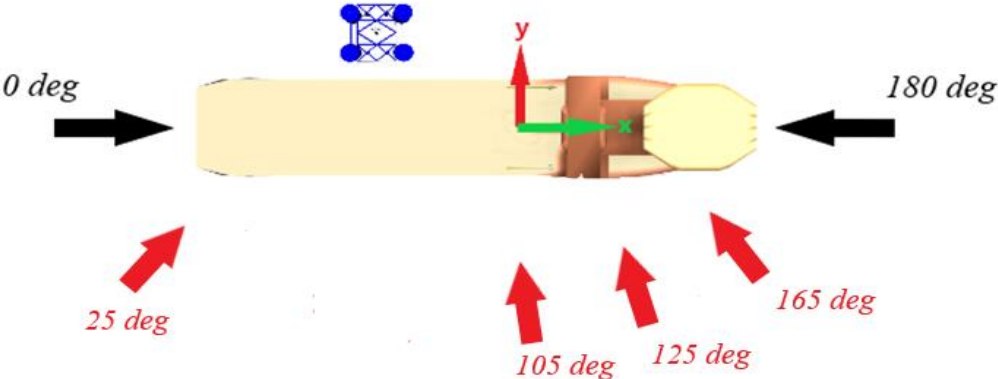
Figure 6-16 Wave directions in SIMO.
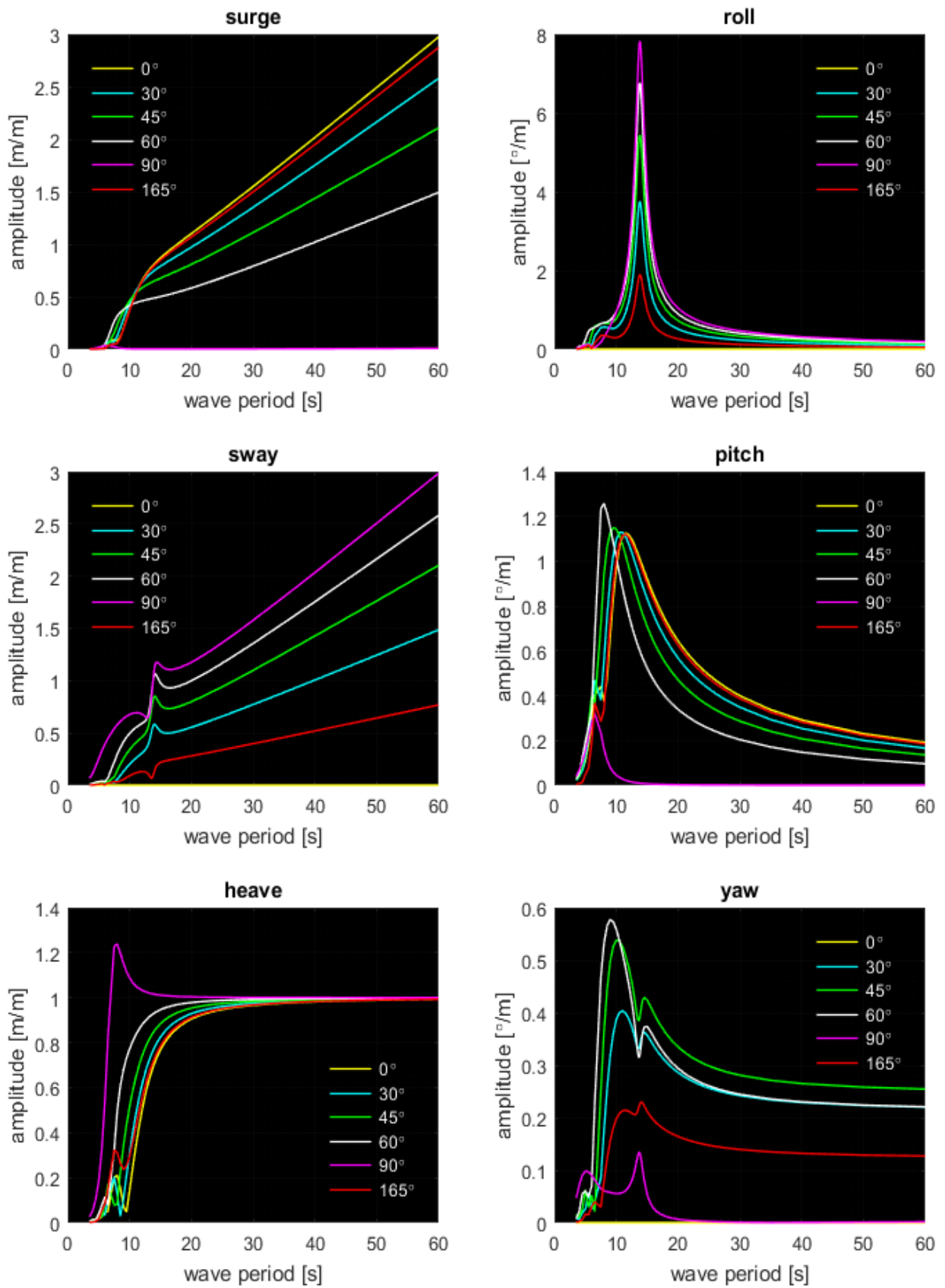
Figure 6-17 RAO of the installation vessel [35].

The chosen peak period for evaluation is 6s since the shielding effect showed a significant influence on the dynamic responses with short waves. The same 2m significant wave height is set and 100 maxima for the lift wire tension are obtained for each wave direction. The GEV fitting for lift wire maxima in Figure 6-18 is used to compare the PDFs at each wave direction.
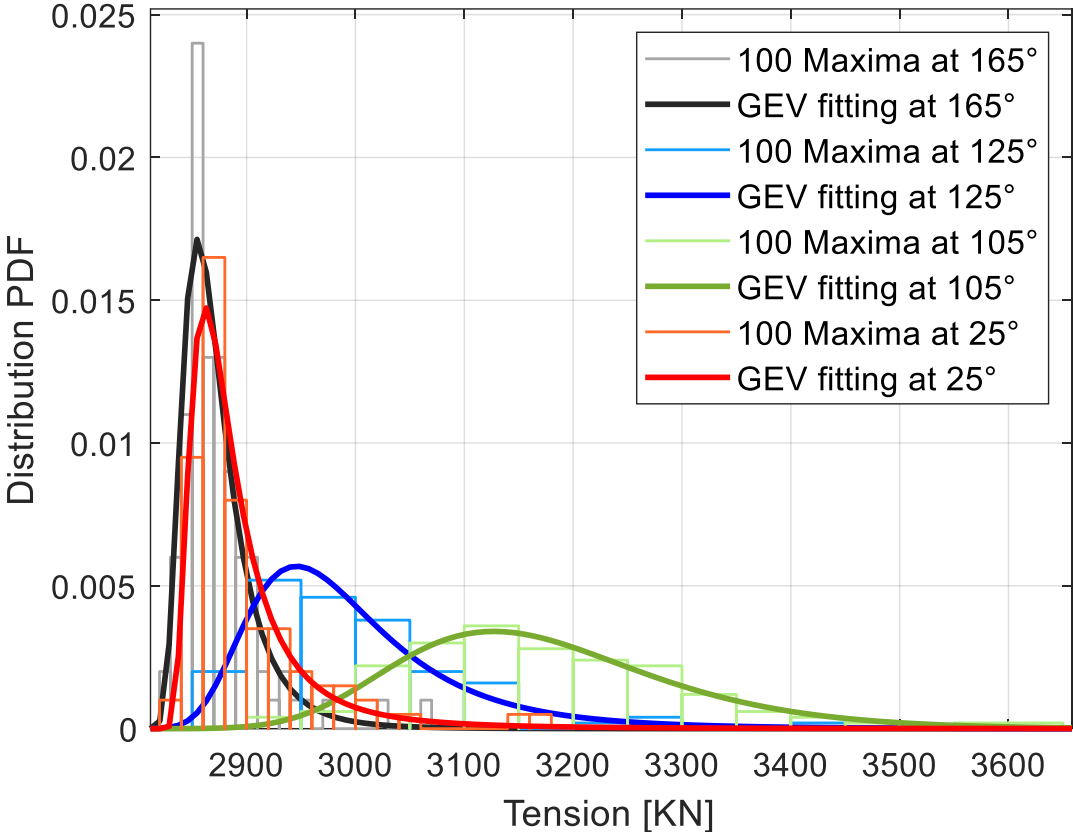
Figure 6-18 Lift wire 100 maxima PDF fitting with GEV at Tp = 6s and Hs = 2.5m for different wave direction.

Figure 6-18 shows that the best results for the maxima are obtained when wave direction is facing the vessel bow and stern at 165° and 25° respectively. Overall, 165° wave direction showed the lowest standard deviation values for the maxima. The largest standard deviation values are obtained when the wave direction is near 90° and facing the vessel starboard. The 105° wave direction has by far the highest standard deviation values for the maxima among all the evaluated directions.

Although the slack limit of the lift wire is less critical in this operation as previously shown at the start of the lowering assessment, Gumbel fitting of 100 minima at each of the 4 wave directions is also compared in Figure 6-19. Same as the maxima, the optimum slack limits are obtained near the vessel bow and stern with 165° wave direction having the lowest slack mean and standard deviation for the lift wire minima.
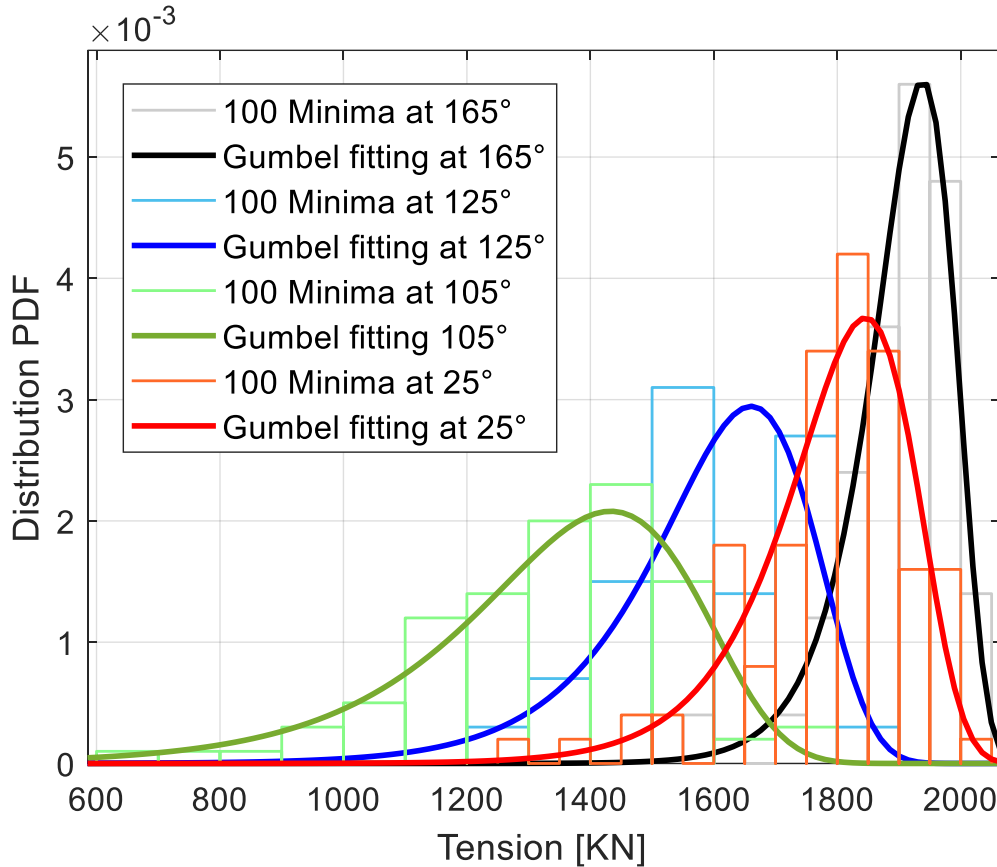
Figure 6-19 Lift wire 100 minima PDF fitting with Gumbel at Tp = 6s and Hs = 2.5m for different wave direction.

Table 6-3 compares the standard deviation values for the lift wire 100 maxima and minima at each of the four wave directions. The standard deviation of both maxima and minima is highest when the wave direction is 105°. When 165° direction is used, the deviation of the extreme values is considerably less.

Table 6-3 Lift wire maxima and minima standard deviation with different wave directions.

Wave direction [deg]	Maxima Std.Dv with shielding [KN]	Minima Std.Dv without shielding [KN]
25	58.85	129.93
105	127.96	204.94
125	95.61	141.94
165	37.13	88.98

Figure 6-20 compares the roll and heave motions of the vessel at 165° and 105°. The figure shows that the responses of both motions at 105° are almost twice as high compared to 165°. These results are expected after evaluating the motions RAO in Figure 6-17. The high roll and heave motion at 105° will increase the induced crane tip motion during the operation according to Eq. (2.28). To further illustrate the effect of the increased crane tip motion at 105° on the lowering dynamic responses, Figure 6-21 is used to compare the lift wire tension at 105° and

165°. The figure shows less fluctuation in the tension force when at165°. The slamming loads when the suction anchor roof reaches the splash-zone are also considerably less compared to 105°.
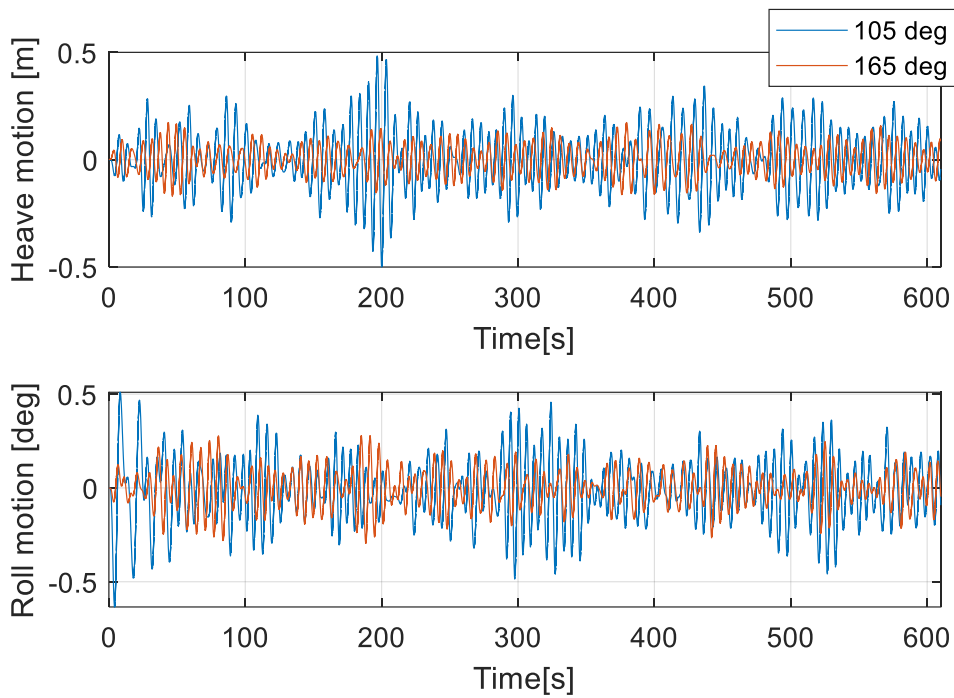
Figure 6-20 Vessel roll and heave motions at Tp =6s and Hs = 1.9m with 105 and 165 deg wave direction.
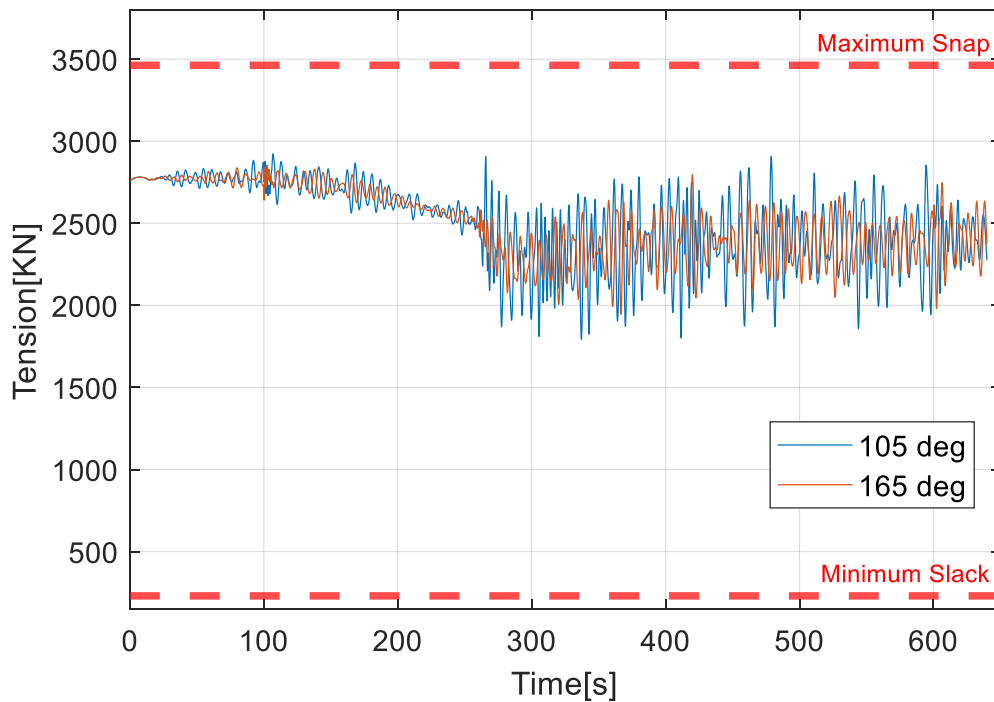
Figure 6-21 Lift wire tension at Tp = 6s and Hs = 1.9m with 105 and 165 deg wave direction.

Figure 6-22 compares the RAOs of three peak periods at the two previously addressed wave directions in Figure 6-20 and Figure 6-21. The figure shows that the RAO depends on the wave direction. At 6s peak period, the wave elevations RAO has a maximum value of 0.5 at 105° wave direction. It is also noticed that the shielding effect is stronger towards the bow for low peak periods in this direction.

Although the shielding effect is stronger at 6s peak period when the wave direction is 105°, it is more optimum to operate at 165° wave direction due to the less induced vessel roll and heave motions. The outcome of WADAM calculation aligns with obtained allowable sea states in Table 6-2. The results obtained earlier in this section showed that the shielding effect has more influence on the operation dynamic responses in short waves at 6s and 8s peak periods.
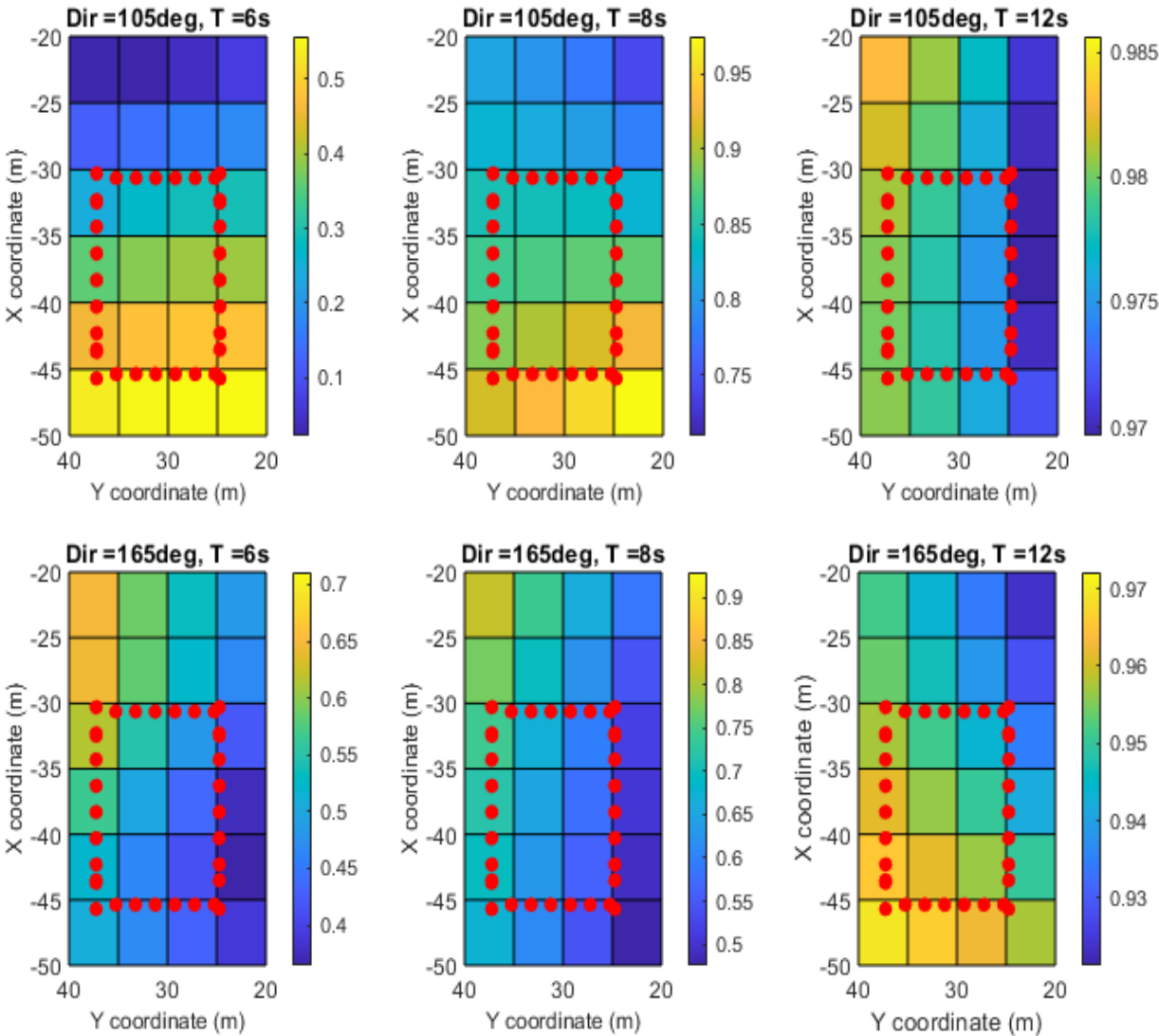
Figure 6-22 RAOs of wave elevation in XY coordinates near the vessel at the template initial position with two different wave directions.

6.3.2 Influence of DDCs

DDCs can be specified in SIMA-SIMO as an additional modeling option. DDCs are not necessary to specify if the element will be fully submerged and assumed unaffected by surface effects throughout the time-domain simulation. The data group will not be relevant and can be omitted [34].

However, if a horizontal inclined fixed slender element crosses the water surface, the slamming force is calculated only if the DDCs are given. DDCs are applied to the center of each strip and are mainly intended for nearly horizontal slender elements or fixed body elements. For tilted elements, a scaling factor will be calculated, proportional to the submerged part of each strip [34]. Depth dependent scaling of hydrodynamic coefficients was previously introduced for each suction anchor in Table 3-12 and Amx is equal to the perforated added mass of the upper half of the water sphere divided by the top slender element length. The element has a length of 0.02m, which is equal to the anchor wall thickness.

Table 3-14 of section 3.3.3. Without a properly identified scaling, the dynamic responses on the lift wire and slings can be extremely different from the currently used model in the simulations. Figure 6-23 compares the time history of the lift wire tension with and without DDC.
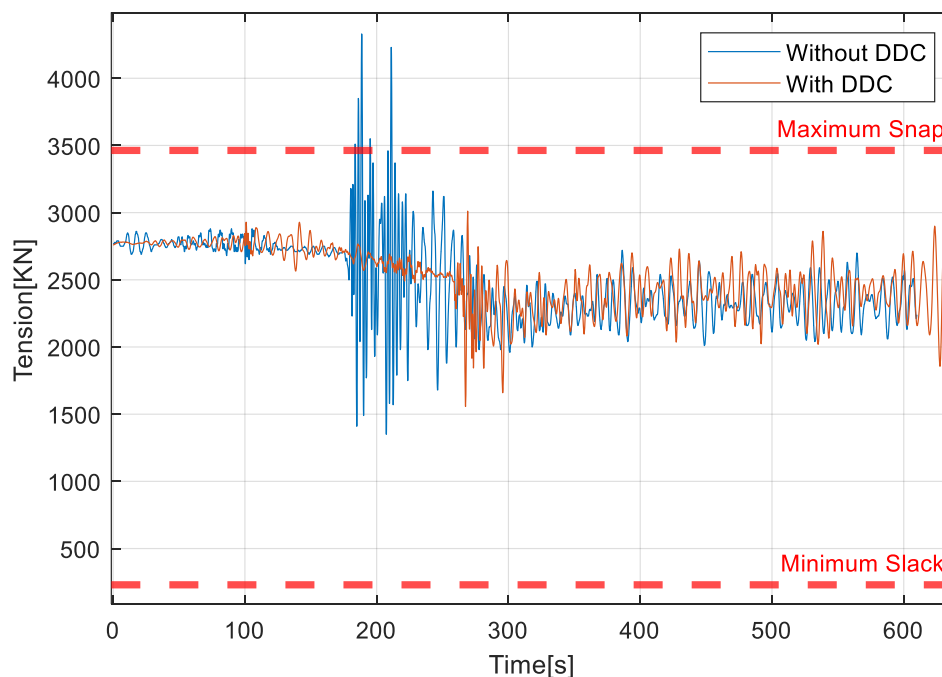
Figure 6-23 Lift wire tension at Tp = 8s and Hs = 1.9m with and without DDC.

The blue time history shows a sudden intense activation of the slamming forces around 180s when the suction anchor bottom reaches the free water surface. This sudden activation of the force takes place due to the specified small slender element at the anchor tip (section 3.3.3). The element takes care of the hydrodynamic coefficients that may give slamming forces.

The absence of DDC causes early activation of the slamming forces when the anchor bottom tip reaches the free surface. Once proper scaling coefficients are identified, the slamming forces

start to activate gradually around 270s as the suction anchor roof reaches the splash zone (red time history in Figure 6-23). This will make the responses more reasonable and similar to the ones normally expected in the real life installation process.

6.3.3 Influence of the main crane tugger lines

Unlike the over-boarding phase, only the two main crane tugger lines are engaged all the time during the splash zone crossing without any involvement from the deck winches. The template induced motion in lowering is less compared to the over-boarding since no translation motion is required to take place in XY plane.

However, when the template reaches the splash zone, the wave kinematic is at its highest and it does not start decaying exponentially until the template is deeply submerged. For large bodies such as the template, 3 out of the 6 DOFs discussed in section 2.4 have no self-restoring moment (coefficients). These 3 DOFs are surge, sway, and yaw. In order to supplement the absence of a self-restoring moment, tugger lines are used to add external stiffness to the template and help in maintaining the template position during the lowering phase for safe deployment.

It is noticed that the absence of tugger lines has a minor influence on lift wire tension. Figure 6-24 compares the tension time history with and without the tuggers for the same sea state. The influence has a similar explanation scenario to the forces acting on the slings in Figure 4-4. The tension on the lifting wire is less before submergence with no tugger lines pulling on the template toward the crane base. However, the tension is higher after submergence since the tugger lines are not pulling upward in the direction of the buoyancy.
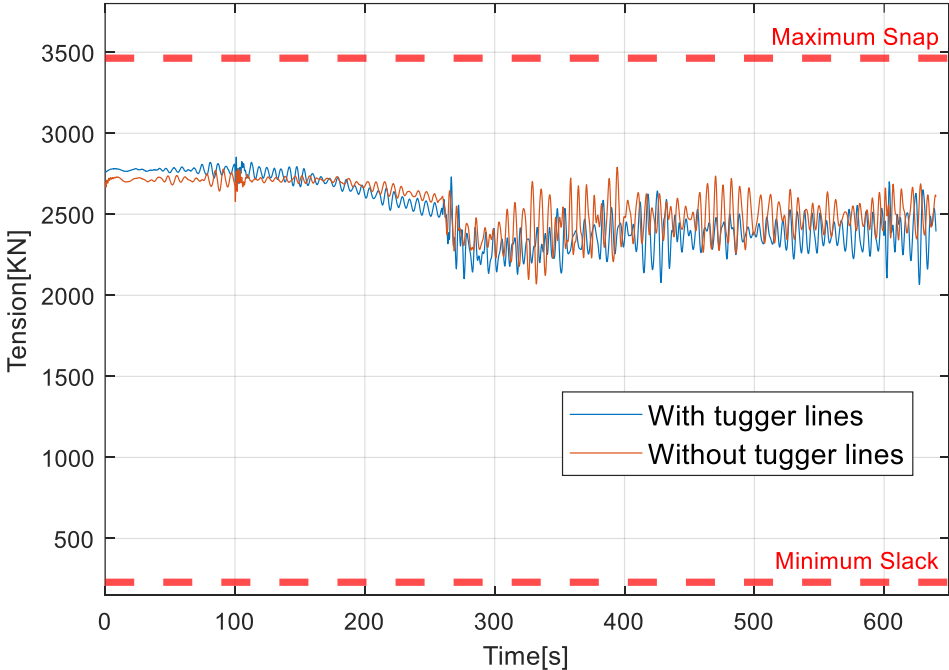
Figure 6-24 Lift wire tension at Tp = 6s and Hs = 1.9m with and without tugger lines.

The template yaw motion was the most influenced by the absence of the crane tugger lines. Although the increased yaw motion did not have any major drawback on the allowable sea

states, the large change in the template initial yaw angle can be problematic for the deployment process later on and thus compromising both the time and the safety of the operation.

Figure 6-25 compares the template yaw motion during the lowering phase with and without engaging the two main crane tugger lines. The same sea state and wave direction are kept for both cases.
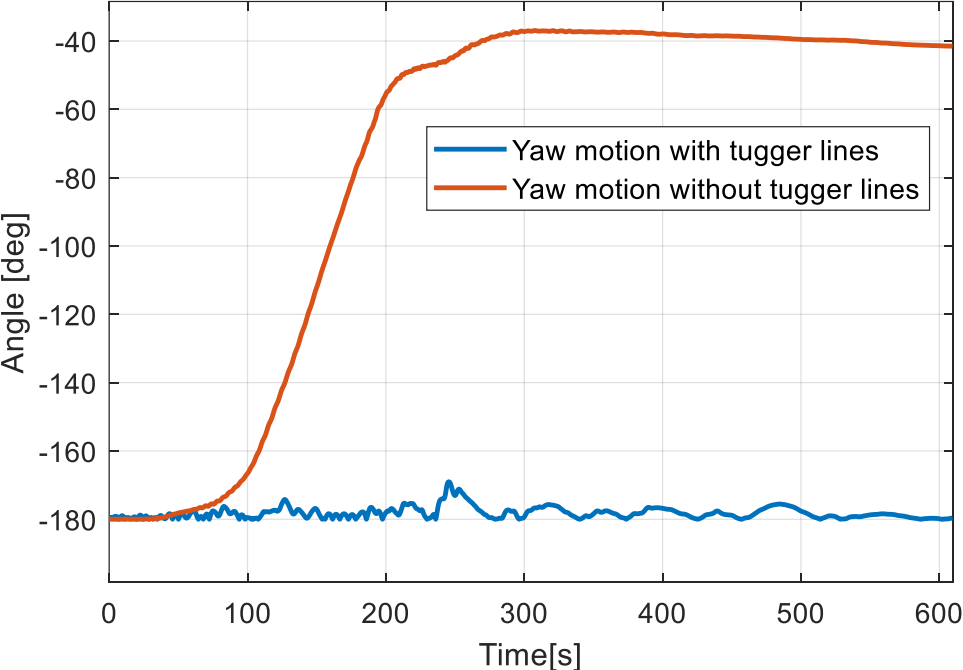
Figure 6-25 Template yaw motion at Tp = 6s and Hs = 1.9m with and without tugger lines.

The figure shows an extreme increase in the template yaw angle from 180 to almost 40 deg when no tugger lines are used. This increase is undesirable for the deployment and thus it is necessary to maintain a mean yaw angle around 180 deg. The template mean yaw angle is kept around 180 deg when 5 tons crane tugger lines are used. The figure also indicates less fluctuation in the yaw motion after 300s from the start of the lowering. At this point, the template is deeply submerged, and the wave kinematics starts decaying, thus decreasing the induced yaw motion of the template.

6.3.4 Influence of suction anchor sizing

The splash-zone crossing operational criteria in section 4.3 showed that the dynamic responses are mainly influenced by the slamming loads acting on the suction anchor roof. These loads are a function of the suction anchor size. This simply means that larger suction anchors will experience higher slamming loads during the operation. For instance, when the suction anchor volume increases, the volume of the trapped water will increase, and thus increasing the hydrodynamic added mass components. The increase of suction anchor diameter will also increase the hydrodynamic drag components acting on the anchor walls. To further evaluate the sizing influence, two cases are investigated by resizing the template anchors. The new

hydrodynamic forces and coefficients are calculated accordingly. In one case, only the anchor diameter is increased for the same height; while in the second case, the height is increased for the same diameter.

Table 6-4 compares the original and the new anchor sizes of each case.

Table 6-4 Suction anchor sizing cases.

	Height [m]	Diameter [m]
Original size	8.225	5.5
Case 1	9.225	5.5
Case 2	8.225	6

75 seeds are generated for each case to obtain 75 maxima for the lift wire tension. Figure 6-26 compares the GEV fitting of the maxima for each case. The shielding effect is applied for all cases at the same sea sates.
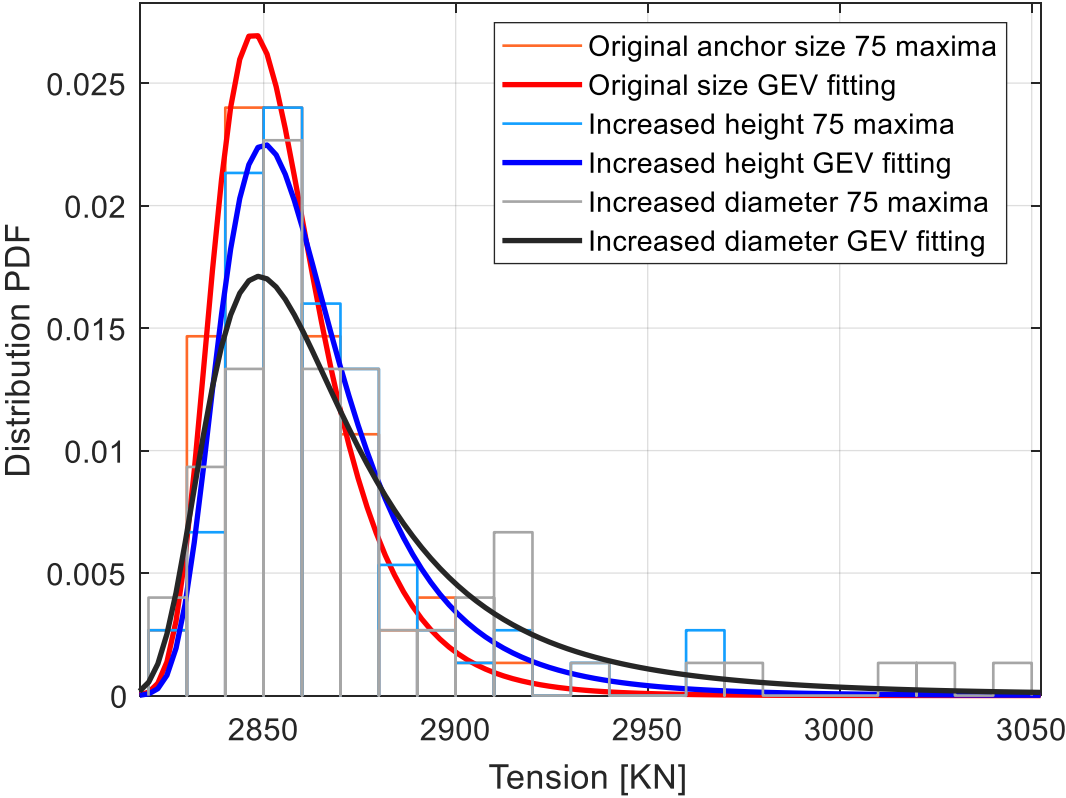
Figure 6-26 Lift wire 75 maxima GEV fitting with anchor resizing at Tp = 6s and Hs = 1.9m.

The figure shows a slight increment in the lift wire extreme responses when the suction anchor height is increased to 9.225m (Case 1). However, when the diameter is increased to 6m (case 2), the deviation is much higher and the extreme responses near the tail are more noticeable than the previous case. This indicates that the size of the anchor diameter has more influence on the operation dynamic response than the height. This outcome can be explained through a theoretical visualization of the vertical added mass for cases 1 and 2. Eq. (3.6) in section 3.3.2.1 showed that the hydrodynamic added mass is calculated from the mass of the trapped water

plus a sphere having the same radius as the anchor. Thus, the vertical added mass is mainly a function of the anchor diameter and height.
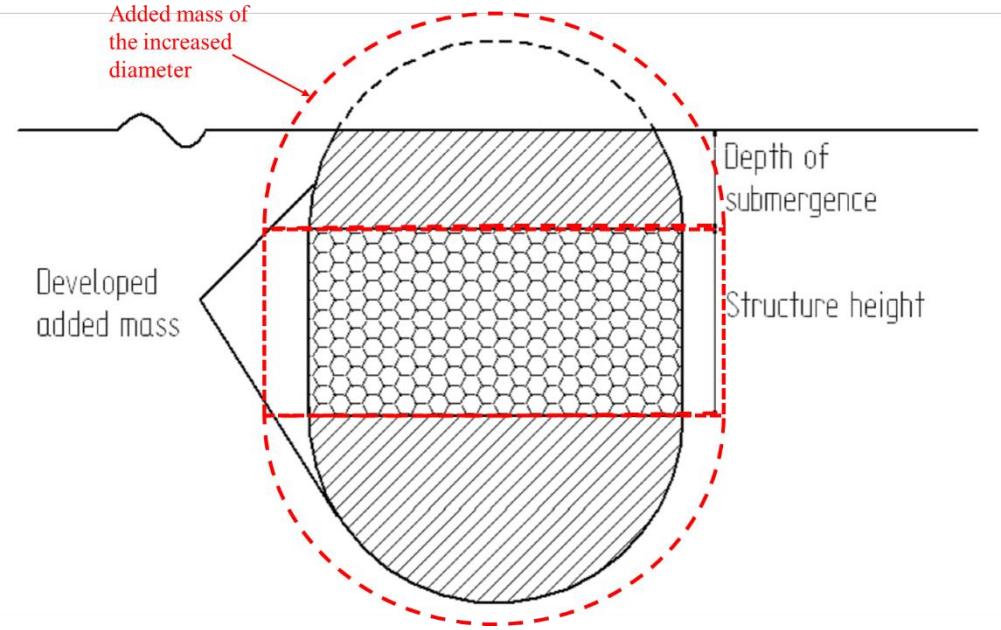
a) Vertical added mass with the increased diameter
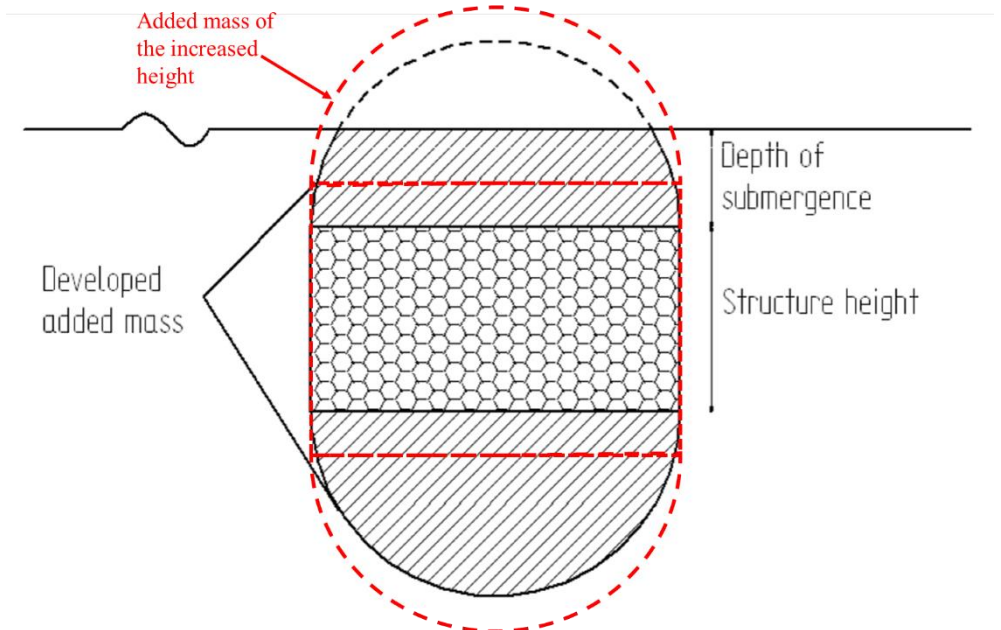
b) Vertical added mass with the increased height

Figure 6-27 Resized suction anchor vertical added mass visualization.

Figure 6-27a shows that the increase of the anchor diameter will impact both the mass of the trapped water and the sphere. However, in Figure 6-27b, the increase of the anchor height will only have an impact on the trapped water mass without any further influence on the sphere.

Thus, the overall vertical added mass is more influenced by the anchor diameter size. The unperforated vertical added mass for case 1 is 314 ton, and 354 ton for case 2.

As for the horizontal added mass, the anchor submerged volume for case 1 is 219 m^3, and 233 m^3 for case 2. This means that the horizontal added mass contribution will be larger in case 2 according to DNVGL-RP-N103 table in Figure 3-6. Furthermore, the vertical drag component is a function of the anchor cross-section area without any involvement of the height.

6.4   Model validation with actual measurements

6.4.1   Crane measurement system

According to DNVGL-ST-0378, a safe load indicator (SLI) must be included within the lifting crane model. The SLI ensures the safety of the operation by providing measurement data. This will allow the crane to remain within the designed safe lifting capacity [38]. Normally, the SLI will consist of:

1) Display panel integrated with a microprocessor
2) Boom length and angle sensors
3) Crane tensiometer (load cell sensor)
4) Wind speed sensor

When the sensors are mounted on the crane, they provide a monitoring function for the lifting load applied on the crane and the hook through the display panel.

The measured hook load through the SLI can be stored in the form of a logging time history. This time history can be used for future reference with similar operations. This will help in improving the overall efficiency of the operations and avoid future errors. The data can be also used in validating the results from numerical models which will be illustrated in the next section.

6.4.2   Measured hook load comparison with modeling results

The crane logging time history for the same installation vessel is provided in this study. The logging data is from a previously installed subsea template. The template had a similar footprint to the one used in this study. However, the overall weight was quite less. The current template model was modified in SIMO to match that of the installed one. The actual logging data is then compared with obtained dynamic responses for the splash-zone crossing with and without shielding effect.

Figure 6-28 compares the results from SIMO with the actual crane measurement without the shielding effect. It is clear from the figure that the slamming force on the suction anchor is significantly overestimated in SIMO without shielding. The maximum dynamic responses in SIMO is almost 2400 KN, while the logging data does not exceed the maximum dry weight at any point of the time history. The minimum dynamic response is also larger in SIMO. However,

the estimation of the buoyancy force and the activation time of the slamming forces is quite accurate in the model. This indicates that the applied scaling for the DDC is adequate.
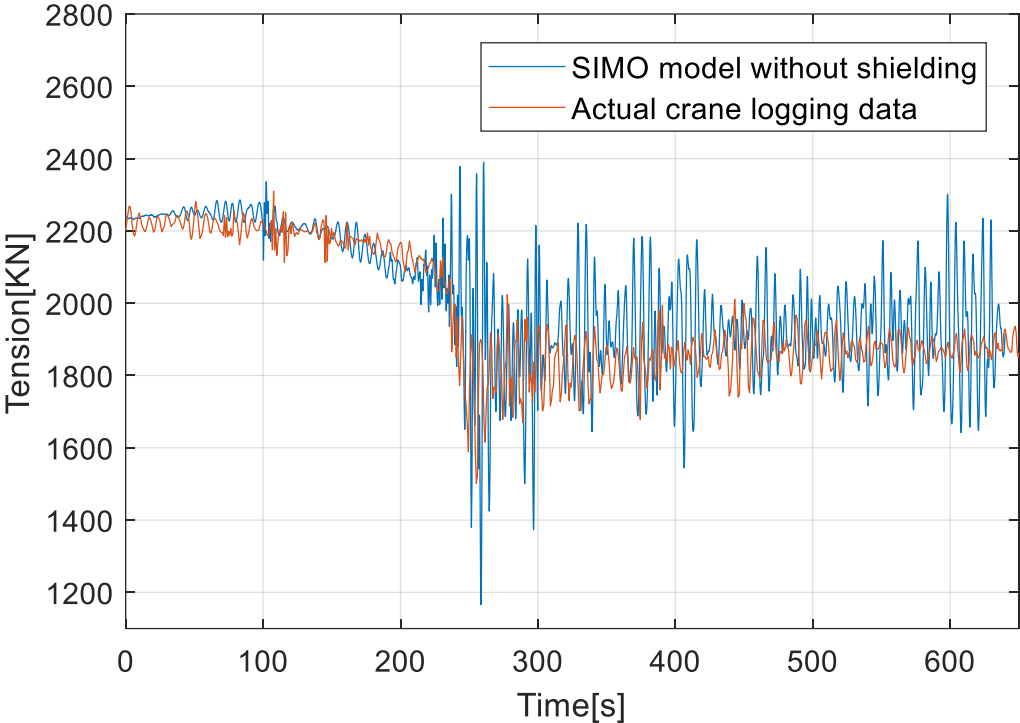
Figure 6-28 Crane logging data comparison without shielding at Hs =1.9m and Tp = 6s.
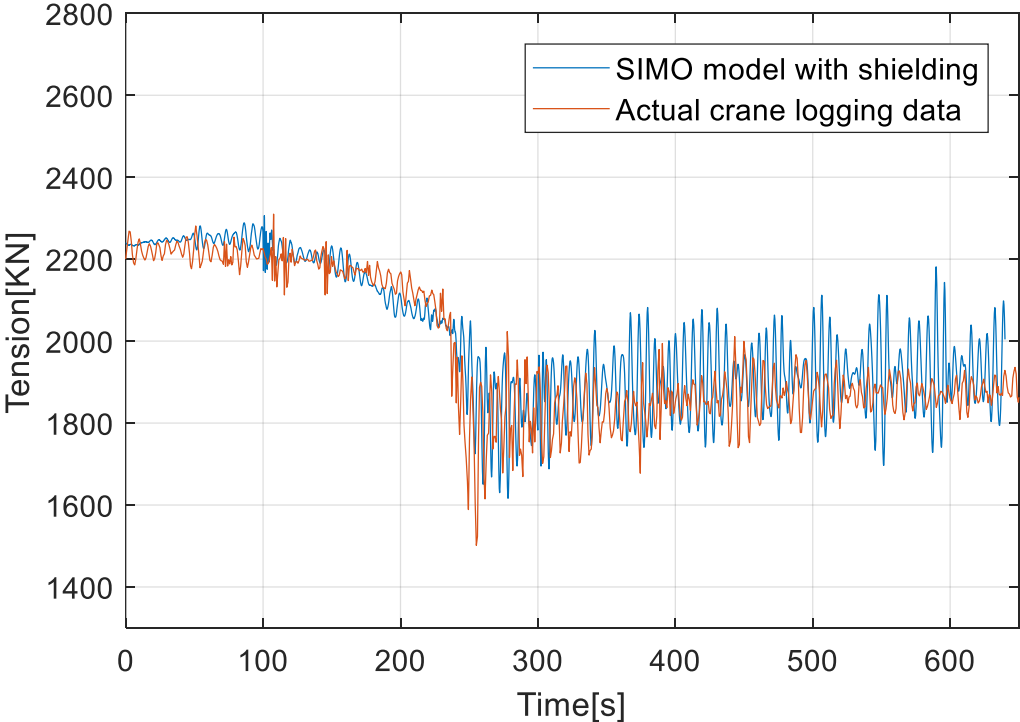
Figure 6-29 Crane logging data comparison with shielding at Hs =1.9m and Tp = 6s.

Figure 6-29 compares the results from SIMO with the actual crane measurement when the shielding effect is utilized. The slamming forces are not overestimated in the shielding model and are similar to the actual crane logging data. Both time histories experience the slamming forces around 250s. However, the actual logging data shows a slightly lower tension. The overall modeling results with shielding are more accurate than Figure 6-28.

Although the model dynamic responses in Figure 6-29 are lower with the shielding effect, the responses are still quite high after crossing the splash-zone. This is mainly due to the absence of wave exponential decay in the model. This was previously discussed in the start of section 6.2 of this chapter.

Overall, these comparisons support the introduced modeling methodology in this study. The obtained dynamic responses have a similar pattern to the actual measurement. This indicates that the hydrodynamic forces and DDCs are distributed properly within the template model.

Chapter 7

Conclusions and Future Work

The thesis studied two phases within the scope of offshore lifting operation of a subsea template. The following sub-sections will summarize the modeling approach as well as the major findings of each phase. The chapter will also include a brief discussion on the combined phases allowable sea states. Finally, the last sub-section will discuss some recommendations for future work.

7.1 Conclusions

7.1.1 Numerical analysis on the over-boarding phase

The first part of the study covered the over-boarding operation. The fully coupled numerical model has been established in SIMA-SIMO including the installation bodies, the lifting system as well as the tugger lines. Eigenvalue analysis and dynamic simulations are performed to study the performance of the installation system in both frequency and time domains. Three different tugger line arrangements are modeled and applied in the analysis to compare the influences of the tugger lines on horizontal motions of the template. Due to the complicity of the over-boarding process with nonlinearities from the tugger line engagement, both transient and the steady-state approaches are employed to assess the allowable sea states. The pendulum motion of the template is considered as the critical response, and statistical method is applied to estimate the extreme pendulum motions from various wave seeds when assessing the allowable sea states.

The study shows that the allowable significant wave height highly depends on the peak periods. When Tp is 6s, the operations are considered safe under all possible wave heights. With increasing Tp, the sea states drop significantly compared to Tp of 6s, and the allowable Hs are around 2m for Tp from 8s to 12s with the best tugger line arrangements. By comparing different tugger line arrangements, it is found that the involvement of the deck tugger can help to increase the allowable sea states of the over-boarding operation. However, the real operations rely on human interactions to control the engagement of the tugger lines, it is very challenging to model these interactions due to the limitations of the numerical tool. It is observed that the engagement and disengagement of different tugger lines in the numerical model introduce extra disturbances in the transient simulations, which lower the allowable sea states. Therefore, the steady-state approach is found to be more realistic to assess the allowable sea states for this operation. In general, higher sea states are obtained using the steady-state approach for over-boarding operations.

7.1.2   Numerical analysis on the splash-zone crossing phase

The second part of the study covered the splash-zone crossing operation. The fully coupled numerical model has also been established in SIMA-SIMO. The template model was modified from the over-boarding to include the scaled hydrodynamic coefficients. The hydrodynamic calculations have been carried out based on DNVGL-RP-N103 recommendations. The dynamic responses are investigated with and without utilizing the vessel shielding effect. The early evaluation of the dynamic responses showed that the lift wire maximum tension limit was more critical than the minimum slack as an operational limiting criterion. Furthermore, the statistical modeling showed that the lift wire maxima generally follows GEV distribution, while the minima follow Gumbel distribution. Same as over-boarding, the allowable sea states showed high dependency on the chosen peak period. The shielding model generally achieved higher operational sea states, especially with low peak periods (short waves). When the shielding effect is applied, the allowable Hs are around 2.5m for Tp from 8s to 12s

Several sensitivity studies have been performed for this phase. The change of wave direction had a significant impact on the lift wire dynamic responses. Based on the vessel RAO, the best operational wave direction was 165°. However, in terms of the disturbed wave elevations RAO, 105° wave direction had the lowest RAO at short peak periods due to the shielding.

DDC scaling showed a significant influence on the slamming force activation in the model. Without proper DDC scaling, the slamming forces will activate suddenly once the suction anchor bottom reaches the free water surface. A proper scaling for the DDC ensures that the forces activate gradually once the suction anchor roof reaches the free water surface.

The template dynamic responses are compared with and without the crane tugger lines. Although the crane tugger lines did not have any major influence on the lift wire tension, their absence caused a significant change in the in template initial yaw angle. This change can be compromising for the operation safety and time.

The influence of the suction anchor sizing on the operation dynamic responses is also investigated. The impact of increasing the suction anchor height and diameter is compared.

Both cases showed an increase in the lift wire maxima. However, the increase of the anchor diameter had more impact than the height by further increasing the hydrodynamic forces experienced by the template.

Finally, a validation of the introduced modeling methodology has been carried out based on an actual crane logging data from a previously installed subsea template. The results showed that the shielding model had more realistic responses when compared to the actual crane logging data. The comparison also showed that the introduced model was quite accurate in estimating the dynamic responses at splash-zone. However, due to the absence of the exponential decay of the wave kinematics, the responses were quite higher in the model when the template starts to be deeply submerged.

7.2   Allowable sea state of the whole operation

As previously discussed in section 4.4, the limiting parameters causing the lowest allowable sea state will be governing the execution of the whole lifting operation. Figure 7-1 compares the allowable sea states of the over-boarding and splash-zone phases. The analytical approach with the highest operational outcome is chosen in the comparison for each phase.
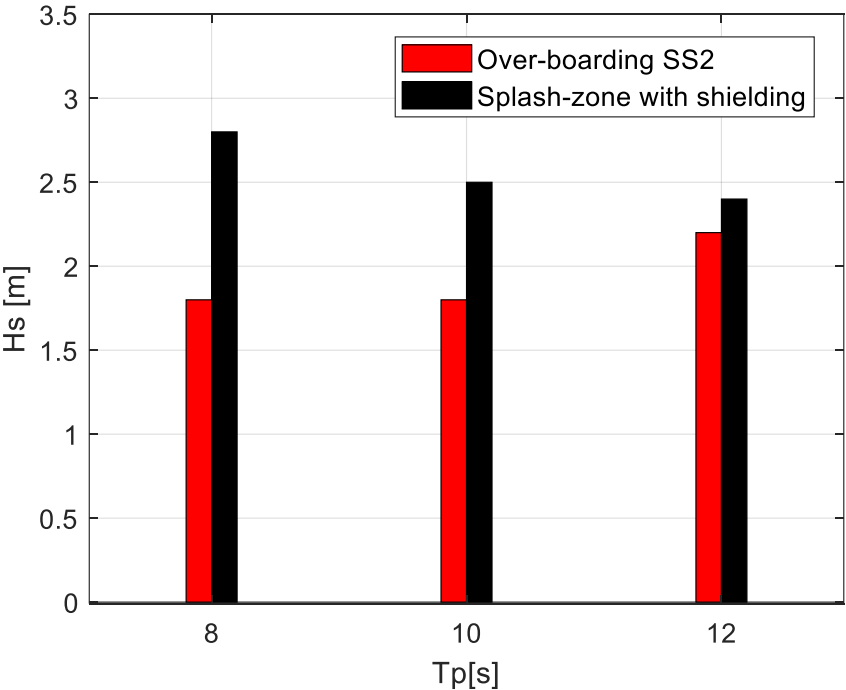
Figure 7-1 Allowable sea states of the combined operation.

The figure clearly shows that the over-boarding phase is governing the operation limiting Hs. It is noticed that the highest limiting Hs for the over-boarding is at 12s Tp since the template critical pendulum motion is at its highest when the peak period is closer to 8s (section 3.5).

However, the splash-zone phase shows an opposite trend from the over-boarding when the shielding effect is utilized. Section 6.2.2 showed that the shielding effect influence is higher at low peak periods. Thus, the highest limiting Hs for the splash-zone crossing is at 8s Tp.

Overall, the limiting Hs of the whole operation based on these two phases will be extremely influenced by Tp. It is recommended to carry out the operation in short waves, since the 6s Tp showed the highest limiting Hs for both phases of the operation (see Table 5-3 and Table 6-2).

7.3   Recommendations for future work

The study provided numerical modeling methodologies for two different phases of offshore lifting operations. The over-boarding model shows some limitations when the transient approach is used in the allowable sea state assessment. As for the splash-zone, even though the validation in section 6.4 showed that the model dynamic responses are reliable in performing operability studies for similar operations, the model can still be enhanced to improve the reliability of obtained results. The following recommendations can be considered for similar future numerical studies:

1) The over-boarding transient approach showed extreme instability when the tugger lines engaging and disengaging sequence is used in controlling the template. It is possible to improve the model further by investigating the possibility of increasing the duration of the operation. The increased duration will make it possible to increase the defined decay and build-up period for each tugger line.

2) The introduced water filling in section 3.3.4 is based on theoretical calculation. It is assumed that the filling will start and continue with a steady rate when the template is fully submerged. The model can be further improved if the actual filling measurements can be provided. This will improve the accuracy of estimated submerged weight of template.

3) The study provided by Solaas and Sandvik was used in scaling the suction anchor vertical damping [37]. Similar studies can increase the accuracy of the hydrodynamic coefficients inputs within the numerical model. It will be beneficial in the future if similar studies cover more ranges of suction anchors sizes, especially when the perforation effect is included.

4) Section 6.2 showed that SIMO has limitations when used in modeling the shielding effect. The absence of the exponential decay of the wave kinematics causes an overestimation of the dynamic responses on the template. To overcome such limitation, the template is lowered just below the free water surface to capture the slamming forces time history at the splash-zone. It will be beneficial in the future if the software overcomes this limitation to improve the reliability of the shielding models.

Bibliography

1.	DNV·GL, *Standard: Marine operations and marine warranty, DNVGL-ST-N001*. 2016.
2.	Bai, Y. and Q. Bai, *Subsea engineering handbook*. 2010, Elsevier: Amsterdam; Boston; Paris.
3.	Li, L., Z. Gao, and T. Moan, *Response Analysis of a Nonstationary Lowering Operation for an Offshore Wind Turbine Monopile Substructure*. Journal of Offshore Mechanics and Arctic Engineering, 2015. **137**(5).
4.	El-Reedy, M.A., *Offshore structures : design, construction and maintenance*. 2020.
5.	Li, L., *Dynamic analysis of the installation of monopiles for offshore wind turbines*. 2016.
6.	Li, L., et al., *Splash zone lowering analysis of a large subsea spool piece*. Marine Structures, 2020. **70**: p. 102664.
7.	Acero, W.G., et al., *Methodology for assessment of the operational limits and operability of marine operations*. Ocean Engineering, 2016. **125**: p. 308-327.
8.	Konkurranseposisjon, N.S., *NORSOK Stnadard U-001, Subsea Production Systems*. Norway, NORSOK, 2002.
9.	Nårstad, A.M., *Suction Anchor Penetration-Estimating Penetration Resistance Based on CPT Sleeve Friction*. 2017, NTNU.
10.	DNV·GL, *Recommended practice: Lifting appliances used in subsea operations, DNVGL-RP-N201*. 2017.
11.	DNV·GL, *Recommended practice: Modelling and analysis of marine operations, DNVGLRP-N103*. 2017.
12.	Li, L., Z. Gao, and T. Moan. *Operability analysis of monopile lowering operation using different numerical approaches*. 2016. ISOPE.
13.	Sandvik, P.C. *Estimation of extreme response from operations involving transients*. in *Second Marine Operations Specialty Symposium (MOSS), Singapore, Aug*. 2012.
14.	DNV·GL, *Loadout, transport and installation of subsea objects, DNVGL-OS-H206*. 2014.
15.	Araujo, R., M. Vaz, and P. Couto. *Methodology for overboarding operations*. in *2nd Marine Operations Speciality Symposium*. 2012.
16.	Sarkar, A. and O.T. Gudmestad, *Study on a new method for installing a monopile and a fully integrated offshore wind turbine structure*. Marine structures, 2013. **33**: p. 160-187.
17.	Gordon, R.B., G. Grytøyr, and M. Dhaigude. *Modeling suction pile lowering through the splash zone*. in *ASME 2013 32nd International Conference on Ocean, Offshore and Arctic Engineering*. 2013. American Society of Mechanical Engineers Digital Collection.
18.	Natskår, A., T. Moan, and P.Ø. Alvær, *Uncertainty in forecasted environmental conditions for reliability analyses of marine operations*. Ocean Engineering, 2015. **108**: p. 636-647.
19.	Guachamin-Acero, W. and L. Li, *Methodology for assessment of operational limits including uncertainties in wave spectral energy distribution for safe execution of marine operations*. Ocean Engineering, 2018. **165**: p. 184-193.

20. Bunnik, T. and B. Buchner. *Numerical prediction of wave loads on subsea structures in the splash zone*. in *The Fourteenth International Offshore and Polar Engineering Conference*. 2004. International Society of Offshore and Polar Engineers.

21. Jia, D. and M. Agrawal. *Fluid-structure interaction: lowering subsea structure/equipment in splash zone during installation*. in *Offshore Technology Conference*. 2014. Offshore Technology Conference.

22. Li, Y., et al., *Study of the Installation Process of the Subsea Tree Passed Through the Splash Zone.* Energies, 2020. **13**(5): p. 1014.

23. DNV·GL, *Enviromental conditions and enviromental loads, DNVGL-RP-C205*. 2018.

24. Reeve, D., A. Chadwick, and C. Fleming, *Coastal engineering: processes, theory and design practice*. 2012: CRC Press.

25. Haver, S., *Metocean modelling and prediction of extremes.* Lecture notes in TMR4195-Design of Offshore Structures. Department of Marine Technology, Norwegian University of Science and Technology, 2017.

26. Gudmestad, O., *Marine technology and operations: theory & practice*. 2015: WIT Press.

27. Journèe, J. and W. Massie, *Offshore Hydrodynamics vol. 4.* Delft University of Technology, Delft, Netherlands, 2001.

28. Bergdahl, L., *Wave-induced loads and ship motions*. 2009, Chalmers University of Technology.

29. Tysse, G.O. and O. Egeland, *Dynamic interaction of a heavy crane and a ship in wave motion.* 2018.

30. Zhou, C., *On extreme value statistics*. 2008: Rozenberg Publishers.

31. Baarholm, G.S., S. Haver, and O.D. Økland, *Combining contours of significant wave height and peak period with platform response distributions for predicting design response.* Marine Structures, 2010. **23**(2): p. 147-163.

32. Mun, J., *Advanced analytical models: over 800 models and 300 applications from the basel II accord to Wall Street and beyond*. Vol. 419. 2008: John Wiley & Sons.

33. Pinheiro, E.C. and S.L. Ferrari, *A comparative review of generalizations of the Gumbel extreme value distribution with an application to wind speed data.* Journal of Statistical Computation and Simulation, 2016. **86**(11): p. 2241-2261.

34. *SINTEF Ocean, SIMO 4.12.1 Theory Manual.* 2018.

35. Parra, C.A., *Numerical Study on Offshore Lifting Operations of a Subsea Spool*. 2018, University of Stavanger, Norway.

36. *SINTEF Ocean, SIMO 4.12.1 User Guide.* 2018.

37. Solaas, F. and P.C. Sandvik. *Hydrodynamic coefficients for suction anchors during installation operations*. in *ASME 2017 36th International Conference on Ocean, Offshore and Arctic Engineering*. 2017. American Society of Mechanical Engineers Digital Collection.

38. DNV·GL, *Standard for offshore and platform lifting appliances, DNVGL-ST-0378*. 2016.

Appendices

Appendix A

Different seeds comparison with the actual crane logging data
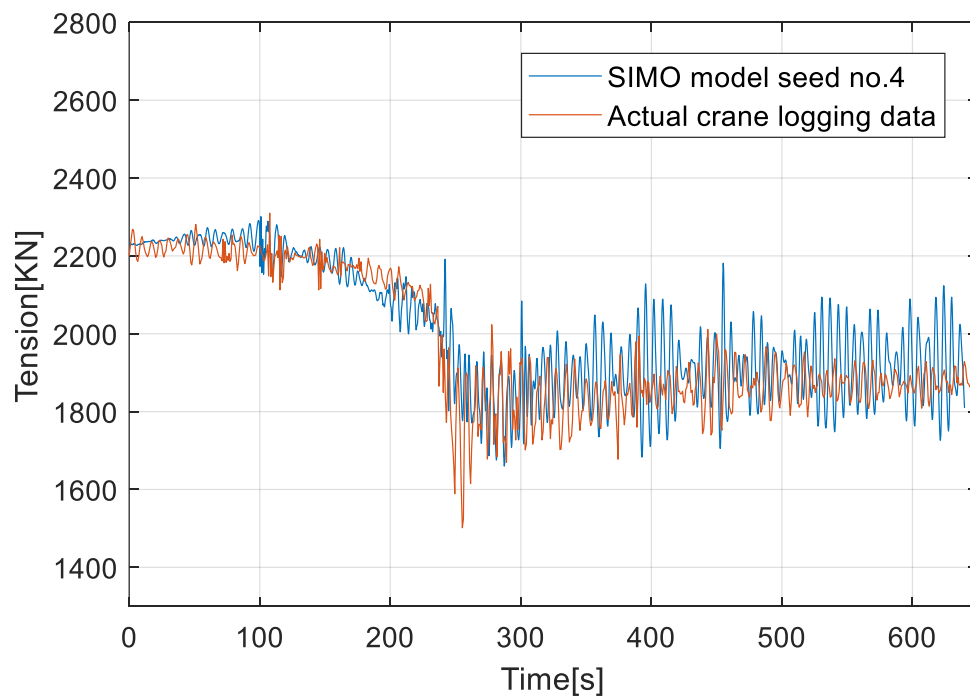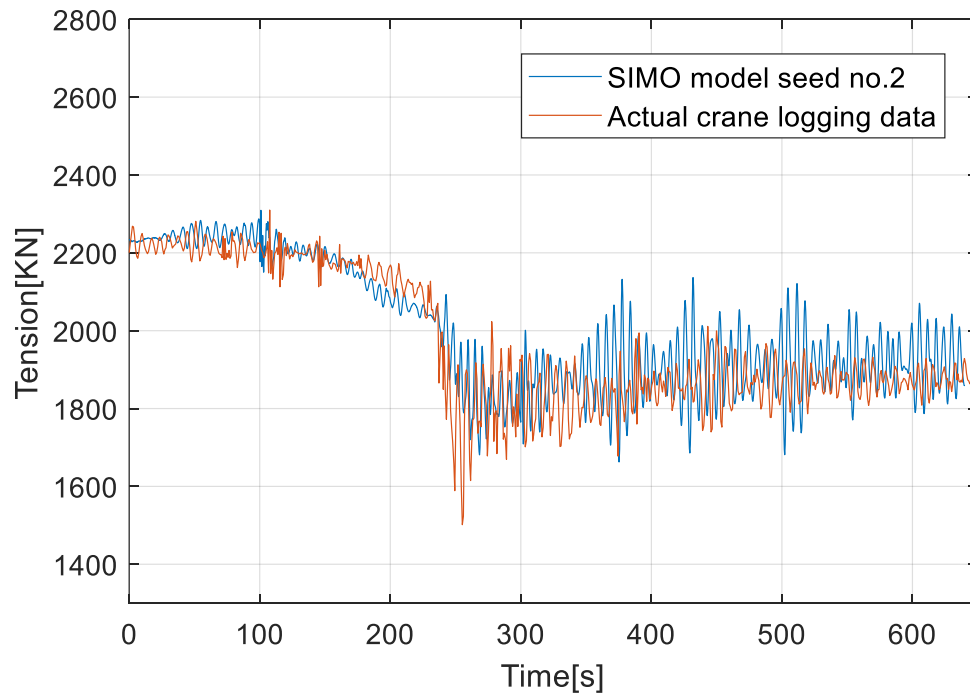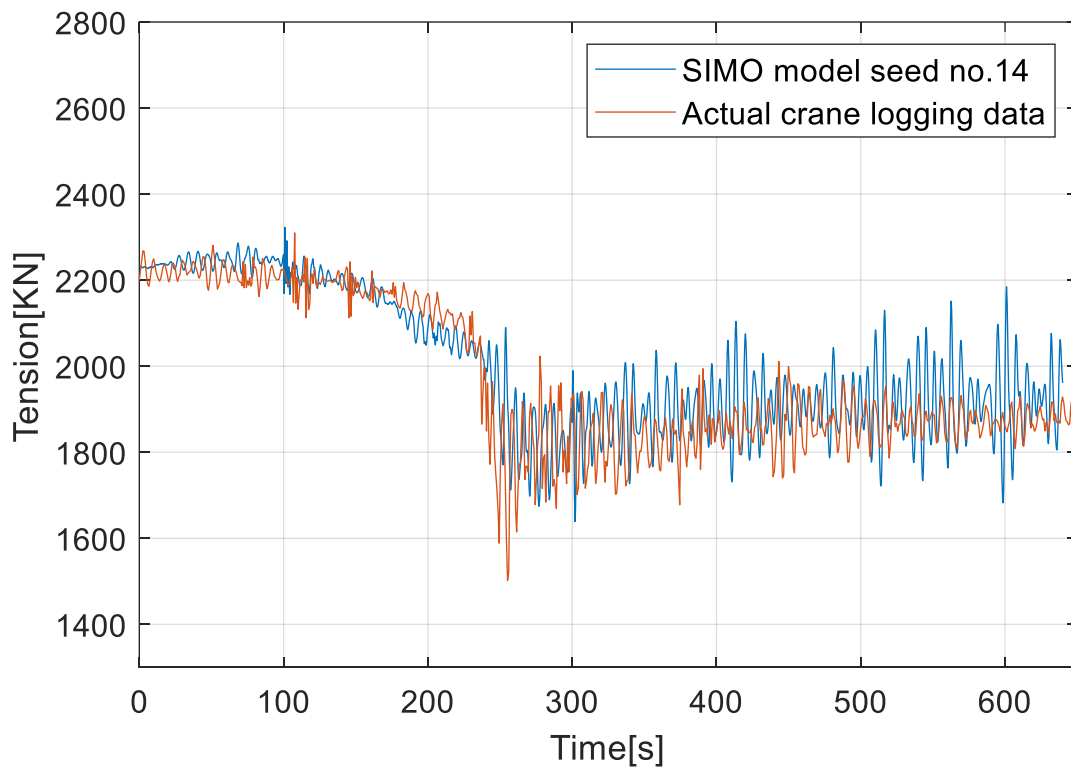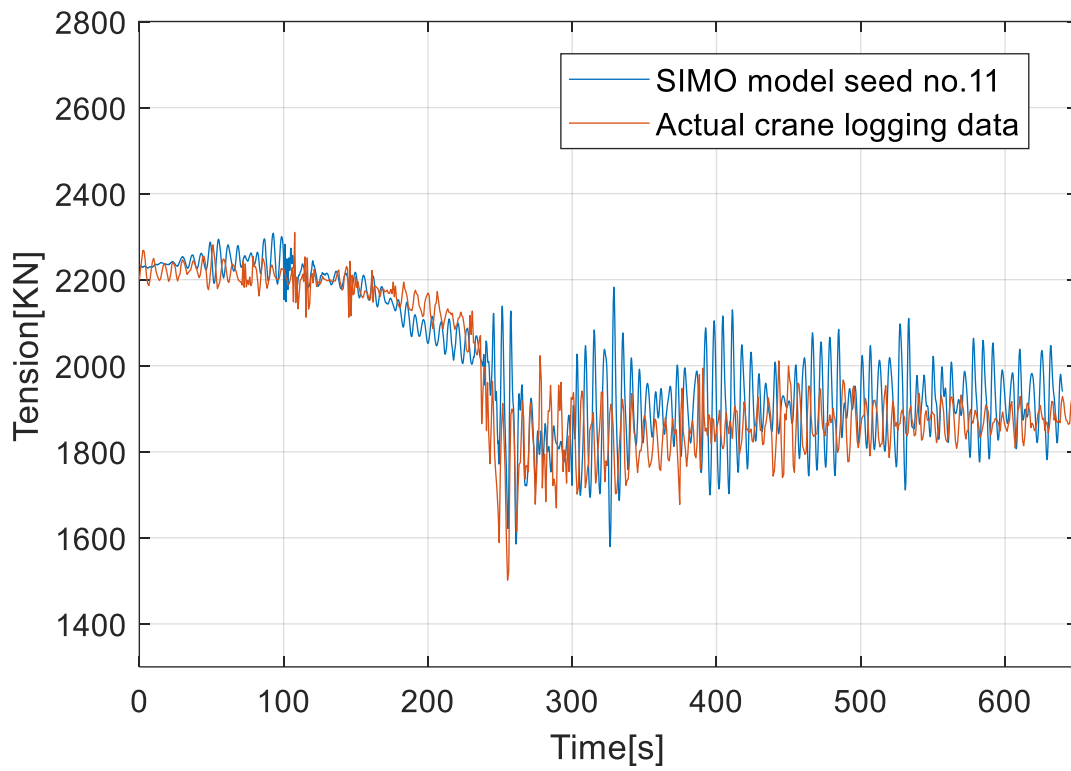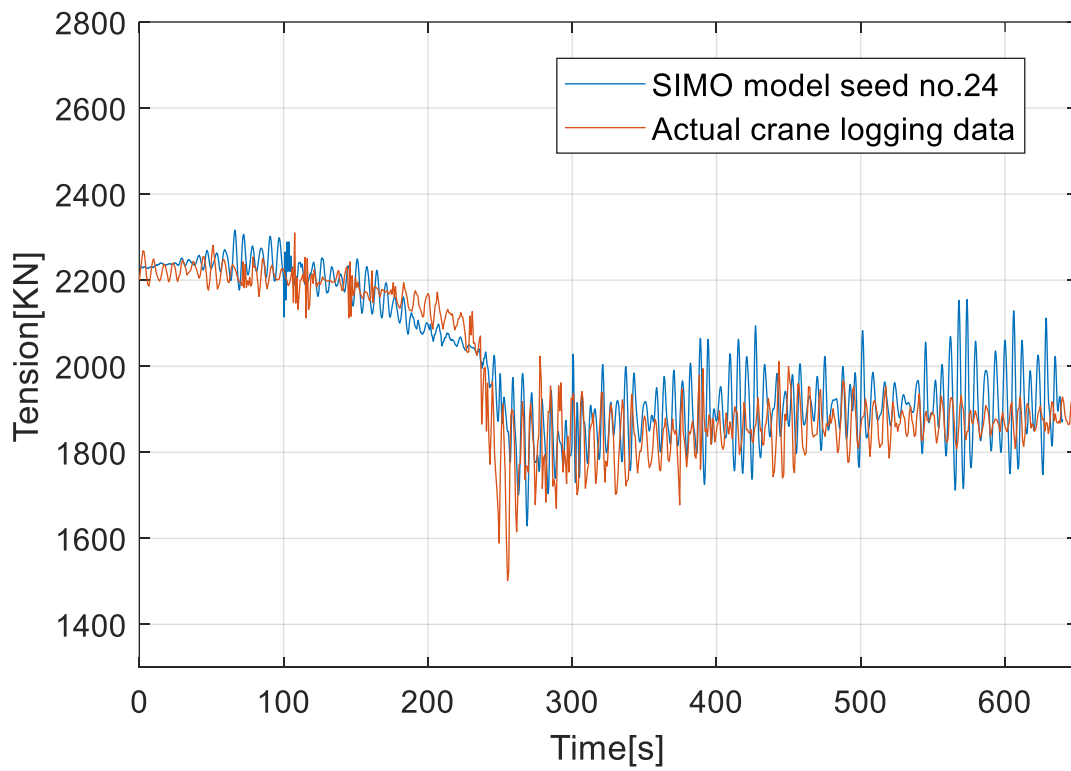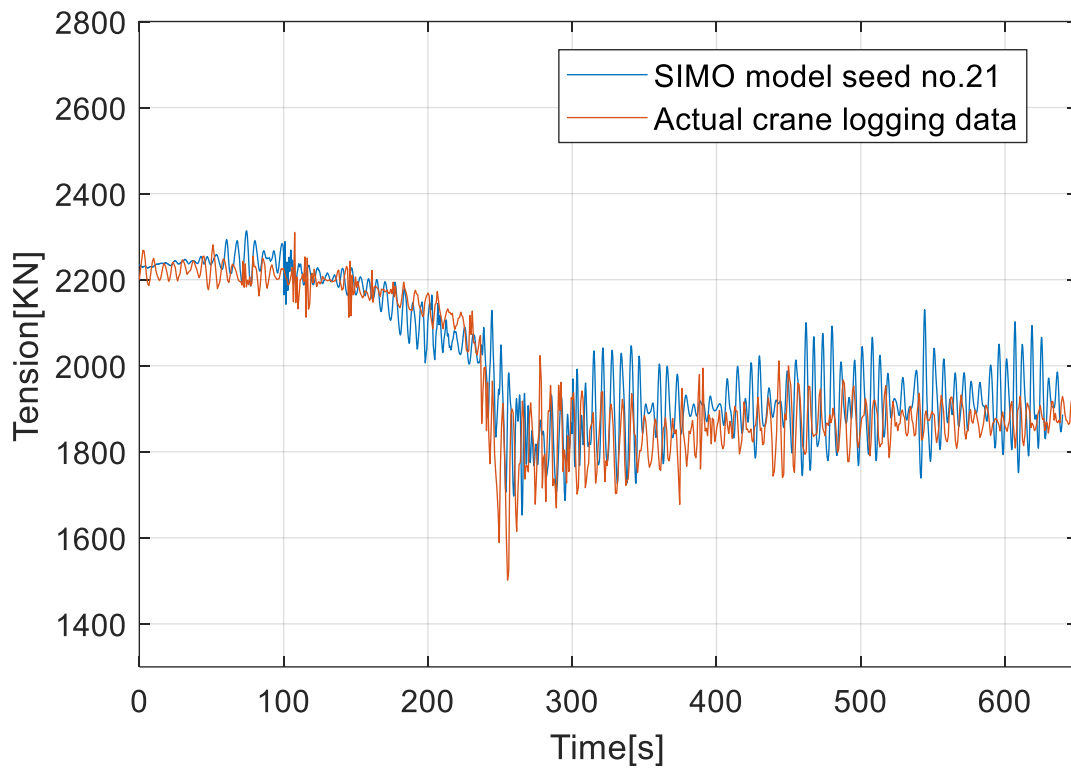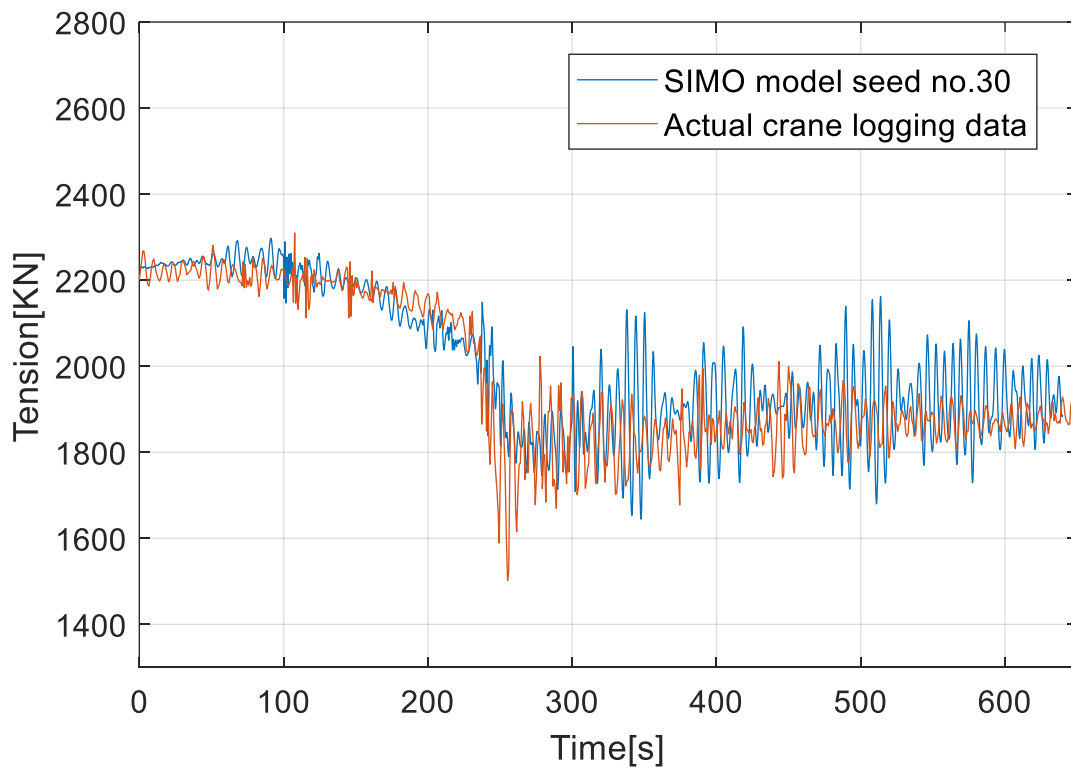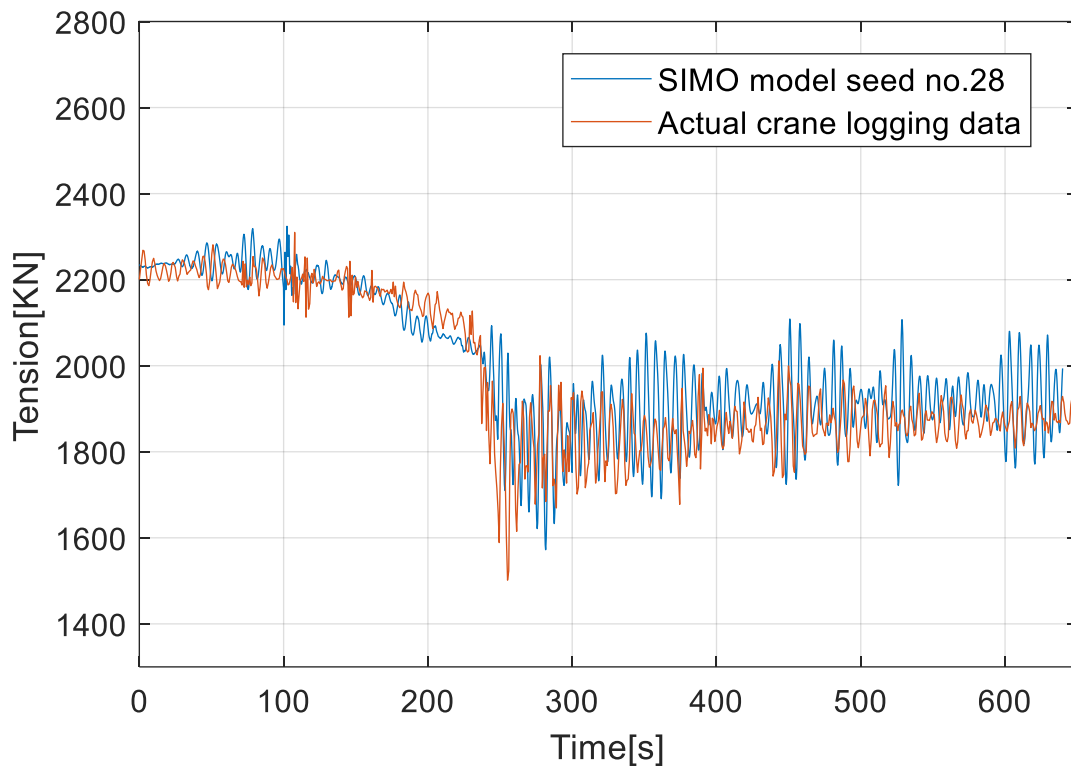
Appendix B

Matlab script for over-boarding phase

```matlab
%% Data Post Processing for the Matfiles
%% Clear all
close all; clear all; clc;
matlab_func = '';
addpath(matlab_func);



% Statistics_name = {'elev_origin'...
%
;'SHIP_Pos1';'SHIP_Pos2';'SHIP_Pos3';'SHIP_Pos4';'SHIP_Pos5';'SHIP_Pos6'...
%
;'TEMP_Pos1';'TEMP_Pos2';'TEMP_Pos3';'TEMP_Pos4';'TEMP_Pos5';'TEMP_Pos6'...
%     ;'HOOK_Pos1';'HOOK_Pos2';'HOOK_Pos3'...
%   ;'LIFTW';'sling1';'sling2';'sling3'; 'sling4';'tugger1';'tugger2'...
%     ;'fender1';'fender2';'fender3';'fender4'...
%       ;'A1_X';'A1_Y';'A1_Z'...
%       ;'A2_X';'A2_Y';'A2_Z'...
%       ;'A3_X';'A3_Y';'A3_Z'...
%       ;'A4_X';'A4_Y';'A4_Z'};

%% Define input and output directory

matlab_input='';    % Directory of the orgnized Matlab files

Hs_no=[2];    % input the Hs values, e.g, Hs_no=[1;1.2;];
Tp_no=[6];      %  input the Tp values, e.g, Tp_no=[7,8];
Dir_no= [165]; %  input the Direction values, e.g.,[120;165];
Seed_no=(1)';  %  input the Seed number values

format compact
nsamp       =           50000 ;
samp        =   0.2000000E-01 ;
start_time =    0.000000     ;
end_time   =    999.9800     ;
Time = linspace(start_time , end_time , nsamp);

%% suction anchor position

theta10 = 26.4723;

theta20 = 61.8489;

theta30 = 10.1637;

theta40 = 77.137;

rotation = 0.4;

theta1 = zeros(length(Time),1);
theta2 = zeros(length(Time),1);
theta3 = zeros(length(Time),1);
theta4 = zeros(length(Time),1);
for ii = 1:1:length(Time)
```

```matlab
    if Time(ii)<200
        theta1(ii) = theta10;
    end
    if (Time(ii)>= 200 &&  Time(ii)<= 540.625)
        theta1(ii) = (Time(ii)-200)*rotation + theta10;
    end
    if (Time(ii) > 540.625)
        theta1(ii) = (540.625-200)*rotation + theta10;
    end
    A1_X0 = -38 - 25.4421 * sin(theta1*pi()/180);
    A1_Y0 = 13 - 25.4421 * cos(theta1*pi()/180);
end

for ii = 1:1:length(Time)
    if Time(ii)<200
        theta2(ii) = theta20;
    end
    if (Time(ii)>= 200 &&  Time(ii)<= 540.625)
        theta2(ii) = (Time(ii)-200)*rotation + theta20;
    end
    if (Time(ii) > 540.625)
        theta2(ii) = (540.625-200)*rotation + theta20;
    end
    A2_X0 = -38 - 25.2013 * sin(theta2*pi()/180);
    A2_Y0 = 13 - 25.2013* cos(theta2*pi()/180);
end

for ii = 1:1:length(Time)
    if Time(ii)<200
        theta3(ii) = theta30;
    end
    if (Time(ii)>= 200 &&  Time(ii)<= 540.625)
        theta3(ii) = (Time(ii)-200)*rotation + theta30;
    end
    if (Time(ii) > 540.625)
        theta3(ii) = (540.625-200)*rotation + theta30;
    end
    A3_X0 = -38 - 14.1606 * sin(theta3*pi()/180);
    A3_Y0 = 13 - 14.1606 * cos(theta3*pi()/180);
end

for ii = 1:1:length(Time)
    if Time(ii)<200
        theta4(ii) = theta40;
    end
    if (Time(ii)>= 200 &&  Time(ii)<= 540.625)
        theta4(ii) = (Time(ii)-200)*rotation + theta40;
    end
    if (Time(ii) > 540.625)
        theta4(ii) = (540.625-200)*rotation + theta40;
    end
    A4_X0 = -38 - 13.7233 * sin(theta4*pi()/180);
    A4_Y0 = 13 - 13.7233 * cos(theta4*pi()/180);
end
%% Extreme vaules of pendulum motion

for kk=1:1:length(Tp_no)
    K = Tp_no(kk);
    for ll=1:1:length(Hs_no)
        L=Hs_no(ll);
        for mm=1:1:length(Dir_no)
```

```matlab
            M=Dir_no(mm);

            extreme_A1 = zeros(length(Hs_no), length(Tp_no));
            extreme_A2 = zeros(length(Hs_no), length(Tp_no));
            extreme_A3 = zeros(length(Hs_no), length(Tp_no));
            extreme_A4 = zeros(length(Hs_no), length(Tp_no));
            temp_max_A1= zeros(length(Seed_no),1);
            temp_max_A2= zeros(length(Seed_no),1);
            temp_max_A3= zeros(length(Seed_no),1);
            temp_max_A4= zeros(length(Seed_no),1);

            for nn=1:1:length(Seed_no)
                N=Seed_no(nn);
                if K>9
                    condition = strcat('w',num2str(L*100),
num2str(K*10),num2str(M),'_seed', num2str(N));
                else
                    condition = strcat('w',num2str(L*100),
'0',num2str(K*10),num2str(M),'_seed', num2str(N));
                end

                cd(matlab_input);
                if exist((strcat(condition,'.mat')),'file')>0
                    load(condition);

                    evalin('caller',strcat('A1_X = ', condition,'.A1_X;'));
                    evalin('caller',strcat('A1_Y = ', condition,'.A1_Y;'));

                    evalin('caller',strcat('A2_X = ', condition,'.A2_X;'));
                    evalin('caller',strcat('A2_Y = ', condition,'.A2_Y;'));

                    evalin('caller',strcat('A3_X = ', condition,'.A3_X;'));
                    evalin('caller',strcat('A3_Y = ', condition,'.A3_Y;'));

                    evalin('caller',strcat('A4_X = ', condition,'.A4_X;'));
                    evalin('caller',strcat('A4_Y = ', condition,'.A4_Y;'));

                    evalin('caller',strcat('tug_craneR = ',
condition,'.tug_craneR;'));
                    evalin('caller',strcat('tug_craneL = ',
condition,'.tug_craneL;'));
                    evalin('caller',strcat('tug_bow = ',
condition,'.tug_bow;'));
                    evalin('caller',strcat('tug_starb = ',
condition,'.tug_starb;'));
                    evalin('caller',strcat('tug_sternL = ',
condition,'.tug_sternL;'));
                    evalin('caller',strcat('tug_sternR = ',
condition,'.tug_sternR;'));

                    evalin('caller',strcat('crane_X = ',
condition,'.crane_X;'));
                    evalin('caller',strcat('crane_Y = ',
condition,'.crane_Y;'));
                    evalin('caller',strcat('crane_Z = ',
condition,'.crane_Z;'));

                    delta_A1_X = A1_X - A1_X0;
                    delta_A1_Y = A1_Y - A1_Y0;
```

```matlab
                        delta_A2_X = A2_X - A2_X0;
                        delta_A2_Y = A2_Y - A2_Y0;

                        delta_A3_X = A3_X - A3_X0;
                        delta_A3_Y = A3_Y - A3_Y0;

                        delta_A4_X = A4_X - A4_X0;
                        delta_A4_Y = A4_Y - A4_Y0;

                        A1_pendulum = sqrt(delta_A1_X.^2 + delta_A1_Y.^2);
                        A2_pendulum = sqrt(delta_A2_X.^2 + delta_A2_Y.^2);
                        A3_pendulum = sqrt(delta_A3_X.^2 + delta_A3_Y.^2);
                        A4_pendulum = sqrt(delta_A4_X.^2 + delta_A4_Y.^2);

                        temp_max_A1(nn)= max(A1_pendulum);
                        temp_max_A2(nn)= max(A2_pendulum);
                        temp_max_A3(nn)= max(A3_pendulum);
                        temp_max_A4(nn)= max(A4_pendulum);

                        clear(condition);

                    end
                end
            end

            extreme_A1(ll, kk) = K;

        end
end

%%fine out the parameters of fitted distribution
% process the maximum for temp_max55
data_max  = temp_max_A1;
data_max2 = temp_max_A2;
data_max3 = temp_max_A3;
data_max4 = temp_max_A4;
[ga, gb] = func_Gumbel_fit(data_max, 'MoM');    % find gumbel parameters
[ga2, gb2] = func_Gumbel_fit(data_max2, 'MoM');
[ga3, gb3] = func_Gumbel_fit(data_max3, 'MoM');
[ga4, gb4] = func_Gumbel_fit(data_max4, 'MoM');
hs_dist = sort(data_max); % sort the maximum data with increasing sequence
hs_dist2 = sort(data_max2);
hs_dist3 = sort(data_max3);
hs_dist4 = sort(data_max4);
f_dist = (1:1:length(hs_dist))/(length(hs_dist)+1);  % empirical
distribution
f_dist2 = (1:1:length(hs_dist2))/(length(hs_dist2)+1);
f_dist3 = (1:1:length(hs_dist3))/(length(hs_dist3)+1);
f_dist4 = (1:1:length(hs_dist4))/(length(hs_dist4)+1);

XG = min(data_max):0.05:max(data_max);              % this is only for plotting
XG2 = min(data_max2):0.05:max(data_max2);
XG3 = min(data_max3):0.05:max(data_max3);
XG4 = min(data_max4):0.05:max(data_max4);
YG = exp(-exp(-(XG-ga)/gb));
YG2 = exp(-exp(-(XG2-ga2)/gb2));
YG3 = exp(-exp(-(XG3-ga3)/gb3));
YG4 = exp(-exp(-(XG4-ga4)/gb4));
```

```
data_mean=mean(data_max)
data_mean2=mean(data_max2)
data_mean3=mean(data_max3)
data_mean4=mean(data_max4)
data_std=std (data_max);
data_std2=std (data_max2)
data_std3=std (data_max3)
data_std4=std (data_max4)
ratio = data_mean/data_std
ratio2 = data_mean2/data_std2
ratio3 = data_mean3/data_std3
ratio4 = data_mean4/data_std4


p_target1 = 0.9;
p_target2 = 0.95;
p_target3 = 0.99;

X_p90= -log(-log(p_target1))*gb+ga
X_p95= -log(-log(p_target2))*gb+ga
X_p99= -log(-log(p_target3))*gb+ga

X_p90_2= -log(-log(p_target1))*gb2+ga2
X_p95_2= -log(-log(p_target2))*gb2+ga2
X_p99_2= -log(-log(p_target3))*gb2+ga2

X_p90_3= -log(-log(p_target1))*gb3+ga3
X_p95_3= -log(-log(p_target2))*gb3+ga3
X_p99_3= -log(-log(p_target3))*gb3+ga3

X_p90_4= -log(-log(p_target1))*gb4+ga4
X_p95_4= -log(-log(p_target2))*gb4+ga4
X_p99_4= -log(-log(p_target3))*gb4+ga4
```

Matlab script for Splash-zone crossing phase

```matlab
%% Data Post Processing for the Matfiles
%% Clear all
close all; clear all; clc;
matlab_func = '';
addpath(matlab_func);



% Statistics_name = {'elev_origin'...
%
;'SHIP_Pos1';'SHIP_Pos2';'SHIP_Pos3';'SHIP_Pos4';'SHIP_Pos5';'SHIP_Pos6'...
%
;'TEMP_Pos1';'TEMP_Pos2';'TEMP_Pos3';'TEMP_Pos4';'TEMP_Pos5';'TEMP_Pos6'...
%      ;'HOOK_Pos1';'HOOK_Pos2';'HOOK_Pos3'...
%    ;'LIFTW';'sling1';'sling2';'sling3'; 'sling4';'tugger1';'tugger2'...
%      ;'fender1';'fender2';'fender3';'fender4'...
%       ;'A1_X';'A1_Y';'A1_Z'...
%       ;'A2_X';'A2_Y';'A2_Z'...
%       ;'A3_X';'A3_Y';'A3_Z'...
%       ;'A4_X';'A4_Y';'A4_Z'};

%% Define input and output directory

matlab_input='';   % Directory of the orgnized Matlab files

Hs_no=[2.5];   % input the Hs values, e.g, Hs_no=[1;1.2;];
Tp_no=[6]      %  input the Tp values, e.g, Tp_no=[7,8];
Dir_no= [165]; %  input the Direction values, e.g.,[120;165];
Seed_no=(1:1:21)';  %  input the Seed number values

format compact
nsamp       =            32000 ;
samp        =    0.2000000E-01 ;
start_time  =    0.000000     ;
end_time    =    639.9200     ;
Time = 0:0.02:639.9
Time2 = Time(100/samp:639.9200/samp)-100

%% Extreme vaules of lifting wire and slings

for kk=1:1:length(Tp_no)
    K = Tp_no(kk);
    for ll=1:1:length(Hs_no)
        L=Hs_no(ll);
        for mm=1:1:length(Dir_no)
            M=Dir_no(mm);

            extreme_liftw = zeros(length(Hs_no), length(Tp_no));
            extreme_sling1 = zeros(length(Hs_no), length(Tp_no));
            extreme_sling2 = zeros(length(Hs_no), length(Tp_no));
            extreme_sling3 = zeros(length(Hs_no), length(Tp_no));
            extreme_sling4 = zeros(length(Hs_no), length(Tp_no));
            temp_max_liftw= zeros(length(Seed_no),1);
            temp_min_liftw= zeros(length(Seed_no),1);
            temp_max_sling1= zeros(length(Seed_no),1);
            temp_max_sling2= zeros(length(Seed_no),1);
            temp_max_sling3= zeros(length(Seed_no),1);
            temp_max_sling4= zeros(length(Seed_no),1)
```

```matlab
            for nn=1:1:length(Seed_no)
                N=Seed_no(nn);
                if K>9
                    condition = strcat('w',num2str(L*100),
num2str(K*10),num2str(M),'_seed', num2str(N));
                else
                    condition = strcat('w',num2str(L*100),
'0',num2str(K*10),num2str(M),'_seed', num2str(N));
                end

                cd(matlab_input);
                if exist((strcat(condition,'.mat')),'file')>0
                    load(condition);


                    evalin('caller',strcat('liftw = ',
condition,'.liftw;'));
                    evalin('caller',strcat('sling1 = ',
condition,'.sling1;'));
                    evalin('caller',strcat('sling2 = ',
condition,'.sling2;'));
                    evalin('caller',strcat('sling3 = ',
condition,'.sling3;'));
                    evalin('caller',strcat('sling4 = ',
condition,'.sling4;'));


                    temp_max_liftw(nn)= max(liftw);
                    temp_min_liftw(nn)= min(liftw);
                    temp_max_sling1(nn)= min(sling1);
                    temp_max_sling2(nn)= min(sling2);
                    temp_max_sling3(nn)= min(sling3);
                    temp_max_sling4(nn)= min(sling4);
                    clear(condition);

                end
            end
        end

%           extreme_A1(ll, kk) = K;

    end
end

%fine out the parameters of fitted distribution
% process the maximum for temp_max55
data_max  = temp_max_liftw;
data_max1 = temp_min_liftw;
data_max2 = temp_max_sling1;
data_max3 = temp_max_sling2;
data_max4 = temp_max_sling3;
data_max5 = temp_max_sling4;
max_probb  = fun_gumbel_max(data_max, 0.98)
```